1999

Single- and multi-photon ionization studies of organosulfur species

Yu-San Cheung
Iowa State University

INFORMATION TO USERS

This manuscript has been reproduced from the microfilm master. UMI films the text directly from the original or copy submitted. Thus, some thesis and dissertation copies are in typewriter face, while others may be from any type of computer printer.

The quality of this reproduction is dependent upon the quality of the copy submitted. Broken or indistinct print, colored or poor quality illustrations and photographs, print bleedthrough, substandard margins, and improper alignment can adversely affect reproduction.

In the unlikely event that the author did not send UMI a complete manuscript and there are missing pages, these will be noted. Also, if unauthorized copyright material had to be removed, a note will indicate the deletion.

Oversize materials (e.g., maps, drawings, charts) are reproduced by sectioning the original, beginning at the upper left-hand corner and continuing from left to right in equal sections with small overlaps. Each original is also photographed in one exposure and is included in reduced form at the back of the book.

Photographs included in the original manuscript have been reproduced xerographically in this copy. Higher quality 6" x 9" black and white photographic prints are available for any photographs or illustrations appearing in this copy for an additional charge. Contact UMI directly to order.

UMI

A Bell & Howell Information Company
300 North Zeeb Road, Ann Arbor MI 48106-1346 USA
313/761-4700 800/521-0600

Single- and multi-photon ionization studies of organosulfur species

by

Yu-San Cheung

A dissertation submitted to the graduate faculty

in partial fulfillment of the requirements for the degree of

DOCTOR OF PHILOSOPHY

Major: Physical Chemistry

Major Professor: Cheuk Yiu Ng

Iowa State University

Ames, Iowa

1999

Graduate College

Iowa State University

This is to certify that the Doctoral dissertation of

Yu-San Cheung

has met the dissertation requirements of Iowa State University

Signature was redacted for privacy.

Major Professor

Signature was redacted for privacy.

For the Major Program

Signature was redacted for privacy.

For the Graduate College

TABLE OF CONTENTS

ACKNOWLEDGEMENTS

Many people have helped me during different ways during my life at Iowa State University. Their kindness was invaluable to my growth in graduate school and I take this chance to express my appreciation to them.

First of all, I deeply thank my parents and my brothers. They are at the other side of the Earth but I always get encouragement from them. Although they do not know what kind of research I am doing here, they are always supportive of my choices and work.

I am also grateful to my advisor, Prof. Cheuk Yiu Ng, for his support, understanding and encouragement in my research. Other than providing the best research opportunities to me, he also has made valuable and useful suggestions on daily life.

I also want to thank Dr Chung-Lin Liao for his assistance in my academics. He is a thorough and knowledgeable person. He certainly made my tough but challenging work a lot easier.

Drs. Chia-Wei Hsu and Jih-Chuang Huang are acknowledged for their help in some of the work presented in this thesis. I also thank Drs. Yu-Ju Chen and He-Quan Zhao for their help in operating apparatus in our laboratories. The experience in operating the different apparatus certainly broadens my scope in the field. Mr Jerry Flesch, a former member of our group, is appreciated for proof-reading this thesis.

Prof. Wai-Kee Li, Drs. See-Wing Chiu, Helene Lefebvre-Brion and Claudina Cossart-Magos are appreciated for their calculations performed for some of my work. I also

acknowledge Prof. John Hepburn for valuable discussions and assistance in the generation of coherent VUV radiation and Prof. Jim Weisshaar about discussions in the paper presented in Chapter 2.

I also thank Drs. Ida N.-L. Ma, Bruce H.-K. Lee and Sherlock S.-L. Lam for sharing the experiences in their lives with me. They provideed valuable encouragement to me.

Doctor Mark Blaedel at the Student Health Center is also acknowledged. His kindness, patience and professional medical treatments helped me to overcome many terrible illnesses during my years here.

Finally, the support from various financial sources is appreciated. They include the teaching assistantship (1994-1995), Henry Gilman Fellowship (1996-1997), and Nelson Chemistry Scholarship (1996-1997) from the Department of Chemistry; and the research assistantship from the Ames Laboratory (1995-1996, 1997-1999). Ames Laboratory is operated for the U. S. Department of Energy by Iowa State University under Contract No. W-7405-Eng-82. The National Science Foundation and Iowa State University are also acknowledged for funding the construction of the new vacuum ultra-violet laser system described in Chapter 7.

CHAPTER 1. GENERAL INTRODUCTION

1. Introduction

Accurate ionization energies (IE's) for molecular species are used for prediction of chemical reactivity and are of fundamental importance to chemists.[1,2] The IE of a gaseous molecule can be determined routinely in a photionization[2] or a photoelectron[3,4] experiment. IE determinations made in conventional photoionization and photoelectron studies have uncertainties in the range of 3-100 meV (25-250 cm^{-1}).

In the past decade, the most exciting development in the field of photoionization and photoelectron spectroscopy has been the availability of high resolution, tunable ultraviolet (UV) and vacuum ultraviolet (VUV) laser sources.[5-7] The laser pulsed field ionization photoelectron (PFI-PE) scheme is currently the state-of-the-art photoelectron spectroscopic technique and is capable of providing photoelectron energy resolution close to the optical resolution.[8-10] For specific molecular species with IE values below 12 eV, the non-resonant two-photon (N2P) PFI-PE scheme involving the use of a UV laser is an attractive method for high resolution photoelectron measurements.[11,12] Without doubt, the single-photon PFI-PE technique is the most versatile high-resolution photoelectron spectroscopic method. At the current technical level, VUV laser radiation with usable intensity can be generated at energies up to ≈17.7 eV by nonlinear optical mixing using commercial dye lasers.[5]

In my PhD study, I have focused my attention on the photoionization processes of some sulfur-containing species. The studies of the photoionization and photodissociation on sulfur-containing compounds [such as CS_2,[13,14] CH_3SH,[15-17] CH_3SSCH_3,[16,18,19]

$CH_3CH_2SCH_2CH_3$,[20] $HSCH_2CH_2SH$[21] and C_4H_4S (thiophene)[22] and sulfur-containing radicals, such as HS,[23] CS,[14] CH_3S,[16,24,25] CH_3CH_2S[20] and CH_3SS,[19]] have been the major subjects in our group because sulfur is an important species contributing to air pollution in the atmosphere. The modeling of the combustion and oxidation of sulfur compounds represents important steps for the control of both the production and the elimination of sulfur-containing pollutants.

Particularly, N2P-PFI-PE studies have been performed on some of the sulfur-containing species with the photoionization apparatus in our laboratory. As a continuation, I have employed similar techniques to study the photoionization of CH_3SH and CH_3CH_2SH (see Chapter 2), CH_3SCH_3 (see Chapter 6) and to probe the CH_3CH_2S radical generated in the photodissociation of CH_3CH_2SH (see Chapter 3).

I have also modified the apparatus to generate VUV laser light. A single VUV photon has enough energy to ionize a molecule and hence single-photon ionization can be studied. The modified apparatus has been used to study the VUV single-photon ionization of CS_2 (see Chapter 4), CH_3SH and CH_3CH_2SH (see Chapter 5) and CH_3SCH_3 (see Chapter 6). Photoionization mainly provides information on the IE of the neutral species and the energy levels (e.g. vibrational energy levels) of the neutral and cationic species. When appropriate, *ab initio* calculations have also been performed (mostly by myself, sometimes by collaborators). The theoretical results are usually very helpful in interpreting the experimental data.

To enhance the ability of the VUV laser technique, a much more sophisticated apparatus is under construction and I have been involved in its design and fabrication.

Although the construction is not finished, the critical parts of the new apparatus have been completed and are functioning very well. When operating, the new apparatus is expected to provide many new and interesting research opportunities. It will be introduced in Chapter 7 where the progress is reported.

2. Dissertation Organization

This dissertation consists of seven chapters, each of which has its own numbering system for equations, tables, figures and references.

Chapter 1 is a general introduction of the thesis. Chapters 2 to 6 contain five papers published in, or accepted for publication in, academic periodicals. Each paper is presented in accordance with the requirements of the periodical to which it was submitted. Because they were submitted to different periodicals, the formats between the papers may be different. Chapters 2 and 3 contain the N2P-PFI-PE spectroscopic studies of CH_3SH,[26] CH_3CH_2SH[26] and CH_3CH_2S radical formed in the photodissociation of CH_3CH_2SH.[27] Chapters 4 and 5 contain the VUV single-photon PFI-PE spectroscopic studies of CS_2,[28] CH_3SH[29] and CH_3CH_2SH.[29] Chapter 6 contains the PFI-PE spectroscopic study of CH_3SCH_3 using N2P and VUV single-photon ionizations.[30]

In Chapter 7, the progress of the construction in our laboratory of a new vacuum ultraviolet laser system equipped with a reflectron mass spectrometer is presented. A general conclusion of these studies are given in Chapter 8 followed by an appendix.

3. Literature Review

The use of lasers in photoionization is relatively old. The first multi-photon ionization (MPI) experiments on gaseous atoms were performed in 1966 by Voronov and Delone.[31] The MPI technique is still a very important and popular tool in spectroscopic studies due to its simple experimental setup. On the other hand, single VUV photon ionization studies in the past have relied mainly on discharge lamps .[32] As commercial lasers have become more and more powerful, the use of VUV laser systems becomes possible and affordable. In fact, some research groups in the world have constructed their own VUV laser systems for photoionization studies.[5-7,33-36]

Parallel to the development of high power laser sources, technical progress has also been made in high-resolution photoelectron spectroscopy. With the introduction of the laser PFI-PE method,[9,10,37,38] the energy resolution for photoelectron spectroscopy has been improved to sub-wavenumbers, approaching that achieved in optical spectroscopy.

In spite of these technical advances, few organosulfur compounds have been studied. Only conventional photoionization or photoelectron techniques have been used to study CH_3SH,[15,39,40] CH_3CH_2SH[4] and CH_3SCH_3.[39,41]

On the other hand, the simpler and symmetric linear organosulfur molecule, CS_2, has been studied in a number of high-resolution photoionization efficiency (PIE)[13,42] and photoelectron spectroscopy experiments.[12,43-45] The two approaches, however, have led to a discrepancy in the value of IE[$CS_2^+(\tilde{X}\,^2\Pi_{3/2,1/2})$]. This discrepancy is most likely caused by the Stark field ionization effect.[46] Furthermore, the IE[$CS_2^+(^2\Pi_{1/2})$] value deduced by the previous

Rydberg series analysis[47] is not in agreement with those of the PIE[13,37] and photoelectron spectroscopy[12,43-45] studies.

Based on the vacuum ultraviolet (VUV) photoionization mass spectrometric sampling of photoproducts formed in the 193-nm photodissociation of $CH_3CH_2SCH_2CH_3$, Ma *et al.* conclude that the CH_3CH_2S radical is predominantly produced in such a photochemical process.[20] In a recent laser induced fluorescence study[48], CH_3CH_2S is also shown to be the predominant product in the 248-nm laser photodissociation of CH_3CH_2SH.

References

1. S. G. Lias, J. E. Bartmess, J. F. Liebman, L. Holmes, R. D. Levin, and W. G. Mallard, J. Phys. Chem. Ref. Data **17**, Suppl. 1 (1988).
2. H. M. Rosenstock, M. K. Draxl, B. W. Steiner, and J. T. Herron, J. Phys. Ref. Data **6**, Suppl. 1 (1977).
3. D. W. Turner, C. Baker, A. D. Baker, and C. R. Brundle, *Molecular Photoelectron Spectroscopy* (Wiley, London, 1970).
4. K. Kimura, S. Katsumata, Y. Achibi, T. Yamazaki, and S. Iwata, *Handbook of HeI Photoelectron Spectra of Fundamental Organic Molecules* (Halsted, Toyko/New York, 1981).
5. J. W. Hepburn, in *Vacuum Ultraviolet Photoionization and Photodissociation of Molecules and Clusters*, edited by C. Y. Ng (World Scientific, Singapore, 1991), p. 435.

6. J. W. Hepburn, in *Laser Techniques in Chemistry*, edited by A. Meyers and T. R. Rizzo (Wiley, New York, 1994).

7. A. H. Kung and Y. T. Lee, in *Vacuum Ultraviolet Photoionization and Photodissociation of Molecules and Clusters*, edited by C. Y. Ng (World Scientific, Singapore, 1991), p. 487.

8. *High Resolution Laser Photoionization and Photoelectron Studies*, edited by I. Powis, T. Baer, and C. Y. Ng, Wiley Series in Ion Chem. and Phys. (Wiley, Chichester, 1995); and references therein.

9. K. Müller-Dethlefs, M. Sander, and E. W. Schlag, Z. Naturforsch. A **39**, 1089 (1984),

10. K. Müller-Dethlefs and E. W. Schlag, Ann. Rev. Phys. Chem. **42**, 109 (1991).

11. A. Strobel, I. Fischer, J. Staecker, G. Niednew-Schatteburg, K. Müller-Dethlefs, and V. E. Bondybey, J. Chem. Phys. **97**, 2332 (1992).

12. I. Fischer, A. Lochschmidt, A. Strobel, G. Niedner-Schatteburg, K. Müller-Dethefs, and V. E. Bondybey, Chem. Phys. Lett. **202**, 542 (1993).

13. Y. Ono, S. H. Linn, H. F. Prest, M. E. Gress, and C. Y. Ng, J. Chem. Phys. **73**, 2523 (1980).

14. S. Nourbakhsh, K. Norwood, G.-Z. He, and C. Y. Ng, Chem. Phys. Lett. Soc. **184**, 147 (1991).

15. S. Nourbakhsh, K. Norwood, H.-M. Yin, C.-L. Liao, and C. Y. Ng, J. Chem. Phys. **95**, 946 (1991).

16. C.-W. Hsu and C. Y. Ng, J. Chem. Phys. **101**, 5596 (1994).

17. C.-W. Hsu, C.-L. Liao, and C. Y. Ng, J. Chin. Chem. Soc. **42**, 149 (1995).

18. W.-K. Li, S.-W. Chiu, Z.-X. Ma, C.-L. Liao, and C. Y. Ng, J. Chem. Phys. **71**, 1692 (1979).

19. Z.-X. Ma, C.-L. Liao, C. Y. Ng, Y.-S. Cheung, W.-K. Li, and T. Baer, J. Chem. Phys. **100**, 4870 (1994).

20. Z.-X. Ma, C.-L. Liao, H.-M. Yin, C. Y. Ng, , N. L. Ma, and W.-K. Li, Chem. Phys. Lett. **213**, 250 (1993).

21. H.-Q. Zhao, Y.-S. Cheung, C.-X. Liao, C. Y. Ng, W.-K. Li, and S.-W. Chiu, J. Chem. Phys. **100**, 4870 (1994).

22. C.-W. Hsu, C.-L. Liao, Z.-X. Ma, and C. Y. Ng, J. Phys. Chem. **99**, 1760 (1995).

23. C.-W. Hsu, D. P Baldwin, C.-L. Liao, and C. Y. Ng, J. Chem. Phys. **100**, 8047 (1994).

24. C.-W. Hsu, C.-L. Liao, Z.-X. Ma, P. J. H. Tjossem, and C. Y. Ng, J. Phys. Chem. **97**, 6283 (1992).

25. S. Nourbakhsh, K. Norwood, G.-Z. He, and C. Y. Ng, J. Am. Chem. Soc. **113**, 6311 (1991).

26. Reprinted from the International Journal of Mass Spectrometry and Ion Processes, **159**, Y.-S. Cheung, C.-W. Hsu, J.-C. Huang, C. Y. Ng, W.-K. Li and S.-W. Chiu, "Nonresonant Two-Photon Pulsed Field Ionization Photoelectron Spectroscopic Study of CH_3SH and CH_3CH_2SH", pp. 13-26, Copyright 1996, with permission from Elsevier Science.

27. Reprinted from the Journal of Electron Spectrometry and Related Phenomena, **97**, Y.-S. Cheung, C.-W. Hsu and C. Y. Ng, "Non-Resonant Two Photon Pulsed Field Ionization Photoelectron Study of CH_3CH_2S Formed in the Photodissociation of CH_3CH_2SH", pp. 115-120, Copyright 1998, with permission from Elsevier Science.

28. Reprinted with permission from J.-C. Huang, Y.-S. Cheung, M. Evans, C.-X. Liao, C. Y. Ng, C.-W. Hsu, P. Heimann, H. Lefebvre-Brion and C. Cossart-Magos, "A High Resolution VUV Photoionization, Photoelectron and Pulsed Field Ionization Study of CS_2 Near the $CS_2^+(X^2\Pi_{3/2,1/2})$ Thresholds", Journal of Chemical Physics **106**, 1997, pp. 864-877. Copyright 1997 American Institute of Physics.

29. Reprinted with permission from Y.-S. Cheung, J.-C. Huang and C. Y. Ng, "Vacuum Ultraviolet Laser Pulsed Field Ionization Photoelectron Studies of Polyatomic Species: Accurate Ionization Energies of CH_3SH and CH_3CH_2SH", Journal of Chemical Physics **109**, 1998, pp. 1781-1786. Copyright 1998 American Institute of Physics.

30. Reprinted from the International Journal of Mass Spectrometry, **109**, Y.-S. Cheung and C. Y. Ng, "Vacuum Ultraviolet Single Photon and Ultraviolet Non-resonant Two-Photon Pulsed Field Ionization Photoelectron Study of CH_3SCH_3", pp. mmmm-nnnn, Copyright 1998, with permission from Elsevier Science.

31. G. S. Voronov and N. B. Delone, Sov. Phys. JETP, **23**, 54 (1996).

32. R. T. Wiedman and M. G. White, in *High Resolution Laser Photoionization and Photoelectron Studies, Wiley Series in Ion Chemistry and Physics* edited by I. Powis, T. Baer, and C. Y. Ng (Wiley, Chichester, 1995), p.79.

33. F. Merkt and T. P. Softley, *ibid.*, p. 119.

34. R. H. Page, R. J. Larkin, A. H. Kung, Y. R. Shen, and Y. T. Lee, Rev. Sci. Instrum. **58**, 1616 (1987).

35. A. H. Kung, Opt. Lett. **8**, 24 (1983).

36. E. Cromwell, T. Trickl, Y. T. Lee, and A. H. Kung, Rev. Sci. Instrum. **60**, 2888 (1989).

37. E. W. Schlag, *ZEKE Spectroscopy* (Cambridge University Press, Cambridge, 1996).

38. K. Müller-Dethefs, in *High Resolution Laser Photoionization and Photoelectron Studies, Wiley Series in Ion Chemistry and Physics* edited by I. Powis, T. Baer, and C. Y. Ng (Wiley, Chichester, 1995), p.21.

39. M. E. Akopyon, Y. L. Sergeev, and F. I. Vilesov, Khim, Vys. Energ. **4**, 305 (1970) [English translation, High Energy Chemistry, **4**, 265 (1970)].

40. R. E. Kutina, A. K. Edwards, G. L. Goodman, and J. Berkowitz, *J. Chem. Phys.* **77**, 5508 (1982).

41. K. Watanabe, T. Nakayma, and J. Mottl, J. Quant. Spectr. And Radiation Transfer, **2**, 369 (1962).

42. W. M. Trott, N. C. Blais, and E. A. Walters, J. Chem. Phys. **71**, 1692 (1979).

43. L.-S. Wang, J. E. Reutt, Y. T. Lee, and D. A. Shirley, J. Electron Spectrosc. Relat. Phenom. **47**, 167 (1988).

44. R. Frey, B. Gotchev, W. B. Petman, H. Pollak, and E. W. Schlag, Int. J. Mass Spectrom. Ion Phys. **26**, 137 (1978).

45. I. Reineck, B. Wanneberg, H. Veenhuizen, C. Nohre, R. Maripuu, K. E. Norell, L. Mattson, L. Karlsson, and K. Siegbahn, J. Electron Spectrosc. **34**, 235 (1984).

46. W. A. Chupka, J. Chem. Phys. **98**, 4520 (1993).

47. Y. Tanaka, A. S. Jursa, and F. J. LeBlanc, J. Chem. Phys. **32**, 1205 (1960).

48. W.-C. Hung, M.-Y. Shen, C.-H. Yu, and Y.-P. Lee, J. Chem. Phys. **105**, 5722 (1996).

CHAPTER 2. NONRESONANT TWO-PHOTON PULSED FIELD IONIZATION PHOTOELECTRON SPECTROSCOPIC STUDY OF CH_3SH AND CH_3CH_2SH

A paper published in the International Journal of Mass Spectrometry and Ion Processes

Y.-S. Cheung, C.-W. Hsu, J.-C. Huang, C. Y. Ng, W.-K. Li and S.-W. Chiu

Abstract

The threshold photoelectron spectra for CH_3SH and CH_3CH_2SH in the photon energy regions of 75 600–77 400 and 74 600–76 400 cm^{-1}, respectively, have been measured using the nonresonant two-photon pulsed field ionization photoelectron (N2P-PFI-PE) spectroscopic technique. The respective ionization energies (IEs) for CH_3SH and CH_3CH_2SH are determined to be 76 302 ± 5 cm^{-1} (9.4602 ± 0.0006 eV) and 74 943 ± 5 cm^{-1} (9.2918 ± 0.0006 eV). The theoretical IEs of 9.46 eV for CH_3SH and 9.30 eV for CH_3CH_2SH obtained by the Gaussian-2 (G2) procedure are in excellent agreement with the experimental values. *Ab initio* calculations for CH_3CH_2SH and $CH_3CH_2SH^+$ at the G2 level indicate that both CH_3CH_2SH and $CH_3CH_2SH^+$ exist as a *gauche*- or a *trans*-conformer with the *gauche*-conformer slightly more stable. Comparison of the experimental and theoretical results show that the main vibrational features resolved in the PFI-PE spectra can be assigned to excitation of vibrational modes involving the H-S torsional, C-S stretching and/or H-S bending vibrations of CH_3SH^+ and *gauche*-$CH_3CH_2SH^+$. A doublet observed for the H-S torsional mode is tentatively attributed to mixing of the harmonic vibrational levels due to the low potential barriers between the potential wells of the *gauche*- and *trans*-conformers of CH_3CH_2SH and $CH_3CH_2SH^+$. The vibrational structures observed in the PFI-PE spectra for CH_3SH and CH_3CH_2SH are consistent with the

expectation that ionization involves the ejection of a mostly nonbonding electron, associated with the S.

1. Introduction

The recently developed pulsed field ionization photoelectron (PFI-PE) spectroscopic technique[1-3] achieves resolution approaching that of optical spectroscopy. Bondybey, Müller-Dethlefs and co-workers have shown that PFI-PE spectra for molecular species can be obtained with good sensitivity using one-color nonresonant two-photon (N2P) ionization.[4-10] In many cases, the one color N2P-PFI-PE spectra are surprisingly similar to those acquired by the single vacuum ultraviolet (VUV) photon ionization scheme.[5,6] The N2P-PFI-PE scheme is very attractive because of its high sensitivity and the availability of commercial pulsed dye lasers with the output range of 200-400 nm required for the ionization of most polyatomic species at their thresholds.

We have recently employed the N2P-PFI-PE technique to study sulfur-containing radicals and organosulfur molecules.[11,12] Here we present the results obtained and the analysis of the N2P-PFI-PE spectra of CH_3SH and CH_3CH_2SH near their ionization thresholds. These spectra provide accurate determinations of the ionization energies (IEs) for CH_3SH and CH_3CH_2SH and the vibrational frequencies for CH_3SH^+ and $CH_3CH_2SH^+$. *Ab initio* calculations on the energetics and structures of CH_3CH_2SH and $CH_3CH_2SH^+$ at the Gaussian-2 level[13,14] are also presented to compare with the experimental results.

2. Experimental and theoretical methods

2.1. Experiment

The experimental apparatus used in this study has been described in detail.[11,12] It is modified from the laser ionization time-of-flight (TOF) mass spectrometer used in previous photodissociation studies.[15,16] A two-stage microchannel plate detector and a set of simple aperture lenses for PE detection have been added below the photoionization region and opposite the ion TOF tube.

For this experiment, CH_3SH (99.5% pure) and CH_3CH_2SH (99% pure) obtained from Aldrich are used without further purification. The CH_3SH or CH_3CH_2SH sample is seeded in Ar carrier gas (sample : carrier gas ≈ 0.2 : 1.0) at a total stagnation pressure of ≈ 2.5 - 3.5 bar at 298 K. The gas mixture is introduced into the photoionization region by supersonic expansion through a pulsed valve with a nozzle diameter of 0.5 mm. The molecular beam is skimmed by a conical skimmer (1-mm diameter, 3.8 cm from the nozzle) before intersecting with a tunable laser beam (90°, 8.3 cm downstream from the skimmer). Both the pulsed valve and the dye laser operate at a repetition rate of 13 Hz.

The molecular beam source chamber is pumped by a freon-trapped, 6-in. diffusion pump (pumping speed ≈ 2000 l/s), while the photoionization chamber and the ion-TOF tube are evacuated by two 50 l/s turbomolecular pumps. During the experiment, the beam source chamber and the photoionization chamber are maintained at pressures of about 1×10^{-4} and 2×10^{-6} Torr, respectively.

The second harmonic output of an excimer (Lambda Physik EMG 201 MSC) pumped-dye laser (Lambda Physik FL 3002) is focused into the photoionization region by a 200-mm

focal length fused-silica lens. Coumarin 153 and 540A dyes are used to produce the fundamental output in the 518-540 nm region. A typical laser pulse energy used in the second harmonic output range of 258-268 nm is 1.2 mJ, as monitored with a pyroelectric detector. The wavelength calibration uses the known resonance-enhanced multi-photon ionization spectrum of atomic sulfur,[25] which is produced by the multi-photon laser photodissociation of CH_3SH or CH_3CH_2SH.

Ion detection using the ion TOF mass spectrometer has been described in detail previously.[15,16] Here, a constant electric field of 280 V/cm is used to extract the ions formed in the photoionization region.

The ZEKE/PFI detection scheme relies on delayed PFI of long-lived high-n Rydberg states populated by laser excitation at a few wavenumbers below the ionization threshold. In this experiment, the firing of the excitation laser is delayed by 750 μs with respect to the triggering pulse for opening the pulsed valve. A 1-μs pulsed field of 2-4 V/cm is applied to the repeller plate 3 μs after firing the dye laser. The pulsed field-ionizes the molecular species in high-n Rydberg states as well as extracts the electrons thus formed to the microchannel plate electron detector. The firing sequence of the pulsed valve, dye laser and pulsed electric field is controlled by two digital delay units (Stanford Research DG535). The electron signal from the electron detector and the laser energy signal from the pyroelectric detector are fed into two identical boxcar integrators (Stanford Research SR250), which are interfaced to an IBM/AT computer. The electron and laser energy signals are averaged for 30 shots at each laser wavelength.

The bandwidth of the dye laser is 0.2 cm^{-1} for the fundamental and about 0.4 cm^{-1} for the second harmonic outputs. For a two-photon ionization process, the resolution of the ionization laser is expected to be about 0.8 cm^{-1}.

2.2. *Ab initio* calculations

The results of G2 calculations on the CH_3SH and CH_3SH^+ systems have been reported previously.[18] The predictions for the IE of CH_3CH_2SH and the heats of formation ($\Delta H°_{f0}$) for CH_3CH_2SH and $CH_3CH_2SH^+$ calculated using the G2 procedure are compared to experimental results here.

The G2 method has been described in detail by Curtiss *et al.*[13,14] Briefly, at the G2 level of theory, molecular structures are optimized using the second-order Møller-Plesset perturbation theory (MP2) with all electrons included using the 6-31G(d) basis set [MP2(full)/6-31G(d)]. All single-point calculations are based on the MP2/6-31G(d) optimized structures. The G2 method, an approximation of a QCISD(T)/6-311+G(3df,2p) calculation, requires single-point calculations at the QCISD(T)/6-311G(d,p), MP4/6-311G(d,p), MP4/6-311+G(d,p), MP4/6-311G(2df,p) and MP2/6-311+G(3df,2p) levels. A small semi-empirical correction is applied to account for high-level correlation effects.

The MP2/6-31G(d) harmonic vibrational frequencies, scaled by 0.93,[18] are taken to be the vibrational frequencies and are used for the zero-point vibrational energy (ZPVE) correction. The total energy at 0 K (E_o) is equal to E_e + ZPVE, where E_e is the total electronic energy. All single point *ab initio* calculations have been carried out on CRAY-YMP and CRAY-2 using the GAUSSIAN 90 or 92 program package.[19]

At the MP2/6-31G(d) level, two equilibrium structures each for CH_3CH_2SH and $CH_3CH_2SH^+$ were obtained with ∠C-C-S-H = 60° (*gauche*-conformation) and 180° (*trans*-conformation). The MP2/6-31G(d) geometrical parameters are given in Table 1. The labeling of the S, C and H atoms are shown in Figs. 1(a) and 1(b). For both CH_3CH_2SH and $CH_3CH_2SH^+$, the MP2/6-31G(d) calculation predicts that the *gauche*-conformer is slightly more stable than the *trans*-conformer. The CH_3CH_2-SH and CH_3CH_2-SH^+ bond rotational barriers are less than 2 kcal/mol at the MP2/6-31G(d) level. This indicates that the vibrational modes for CH_3CH_2SH and $CH_3CH_2SH^+$ involving C-S rotation (i.e., the torsional mode) are not harmonic, even at low vibrational levels and that the vibrational frequencies obtained from the harmonic approximation are not accurate. In spite of the strong anharmonicities, the G2 values for $\Delta H°_{f0}$'s and IEs are only slightly affected since the contributions of these modes to the ZPVEs are minor.

However, the anharmonicity may cause serious error in the vibrational spacings calculated for the torsional modes of CH_3CH_2SH and $CH_3CH_2SH^+$. Correct values can only be obtained by considering the potential energy as a function of the normal coordinate and solving the corresponding Schrödinger equation. The calculations of the torsional potentials are made at the MP2/6-31G(d,p) level using DEC Alpha workstations, and the torsional vibrational wavefunctions and energies described below are made using the Mathcad Plus 6.0 software installed in a Pentium microcomputer.

Table 1
Geometrical parameters for *gauche*-CH_3CH_2SH, *trans*-CH_3CH_2SH, *gauche*-$CH_3CH_2SH^+$ and *trans*-$CH_3CH_2SH^+$ calculated at the MP2/6-31G(d) level[a]

	gauche-conformer (C_1)		*Trans*-conformer (C_s)	
	$CH_3CH_2SH/CH_3CH_2SH^+$	Δr(or $\Delta\angle$)[b]	$CH_3CH_2SH/CH_3CH_2SH^+$	Δr(or $\Delta\angle$)[b]
r[S(1)-C(2)]	1.819/1.799	-0.020	1.822/1.802	-0.020
r[C(2)-C(3)]	1.521/1.533	+0.012	1.521/1.520	-0.001
r[C(3)-H(4)]	1.092/1.091	-0.001	1.093/1.091	-0.002
r[C(3)-H(5)]	1.093/1.092	-0.001		
r[C(3)-H(6)]	1.094/1.092	-0.002	1.093/1.092	-0.001
r[C(2)-H(7)]	1.093/1.098	+0.005	1.092/1.099	+0.007
r[C(2)-H(8)]	1.093/1.092	-0.001		
r[S(1)-H(9)]	1.342/1.350	+0.008	1.341/1.350	+0.009
∠S(1)-C(2)-C(3)	113.8/111.9	-1.9	109.0/111.2	+2.2
∠C(2)-C(3)-H(4)	110.8/112.0	+1.2	111.0/111.9	+0.9
∠C(2)-C(3)-H(5)	111.0/111.9	+0.9		
∠C(2)-C(3)-H(6)	110.3/107.0	-3.3	110.1/107.8	-2.3
∠C(3)-C(2)-H(7)	111.0/111.3	+0.3	110.2/113.0	+2.8
∠C(3)-C(2)-H(8)	110.4/112.7	+2.3		
∠C(2)-S(1)-H(9)	96.3/97.8	+1.5	97.0/99.0	+2.0
∠S(1)-C(2)-C(3)-H(4)	57.1/59.6	+2.5	60.2/61.6	+1.4
∠S(1)-C(2)-C(3)-H(5)	-62.9/-64.0	-1.1		
∠S(1)-C(2)-C(3)-H(6)	177.5/177.8	+0.3		
∠H(6)-C(3)-C(2)-H(7)	60.0/59.1	-0.9	59.7/60.8	+1.1
∠H(6)-C(3)-C(2)-H(8)	-58.5/-63.5	-5.0		
∠C(3)-C(2)-S(1)-H(9)	60.5/55.6	-4.9		

Table 1 (continued)

[a]All bond distances (r) are in Å. All angles ($\angle$) are in degrees.

[b]$\Delta r = r(CH_3CH_2SH^+) - r(CH_3CH_2SH)$ and $\Delta\angle = \angle(CH_3CH_2SH^+) - \angle(CH_3CH_2SH)$, where $r(CH_3CH_2SH^+)$, $r(CH_3CH_2SH)$], $\angle(CH_3CH_2SH^+)$ and $\angle(CH_3CH_2SH)$] are the r and $\angle$ values associated with CH_3CH_2SH and $CH_3CH_2SH^+$.

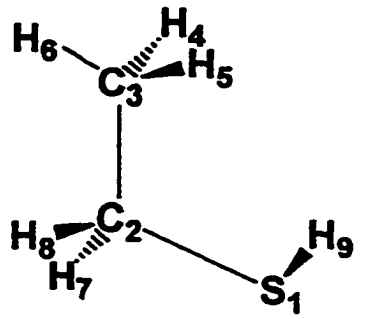

$CH_3CH_2SH/CH_3CH_2SH^+$

(gauche; C_1)

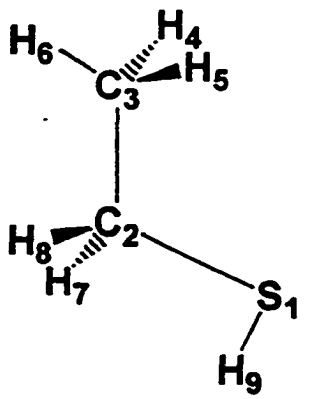

$CH_3CH_2SH/CH_3CH_2SH^+$

(trans; C_s)

Fig. 1. Structures for *gauche*-$CH_3CH_2SH/CH_3CH_2SH^+$ and *trans*-$CH_3CH_2SH/CH_3CH_2SH^+$ showing the numbering of S, C and H atoms. See Table 1 for detailed MP2/6-31G(d) optimized geometric parameters.

Strictly speaking, the normal coordinate for the torsional mode involves not only the dihedral angle ∠C-C-S-H but also the other internal coordinates. However, it is reasonable to assume that ∠C-C-S-H is the major component. To further simplify the problem, we assume a rigid rotation, i.e., the moments of inertia of the CH_3CH_2 and SH moieties do not change during the internal rotation. With these assumptions, the energies for the C-S bond rotation are the eigenvalues of the following one-dimensional Schrödinger equation:

$$(-\hbar^2/2\mu)[d^2\Psi(\phi)/d\phi^2] + V(\phi)\Psi(\phi) = E\Psi(\phi), \qquad (1)$$

where $\Psi(\phi)$ is the vibrational wavefunction for the torsional vibration; ϕ is the normal coordinate for the torsional mode, i.e., ∠C-C-S-H; $V(\phi)$ is the potential energy function; μ is the reduced moment of inertia of the CH_3CH_2 and SH moieties along the C-S bond; and the other symbols have their usual meanings. The values for μ were taken as those for the equilibrium structures at $\phi \approx 60°$, which are 1.68 and 1.70 amu $Å^2$ for the neutral and cation, respectively.

To construct $V(\phi)$, we calculate the MP2/6-31G(d,p) energies at ϕ = 0°, 10°, ..., 180°. At each value of ϕ, all other bond-lengths, bond-angles and torsional angles are optimized to obtain the lowest possible energies. In addition, the equilibrium structures and transition structures with $\phi \approx 60°$ and 120°, respectively, are fully optimized separately. Using these discrete points, smooth curves for the torsional potentials of CH_3CH_2SH and $CH_3CH_2SH^+$ are produced by cubic-spline interpolation. The torsional potentials for CH_3CH_2SH and $CH_3CH_2SH^+$ thus obtained are shown in the lower and upper parts of Fig. 2, respectively. The energy scale is given in kcal/mol measured with respect to the minimum of the potential well for CH_3CH_2SH (or $CH_3CH_2SH^+$) at ∠C-C-S-H ≈ 60°.

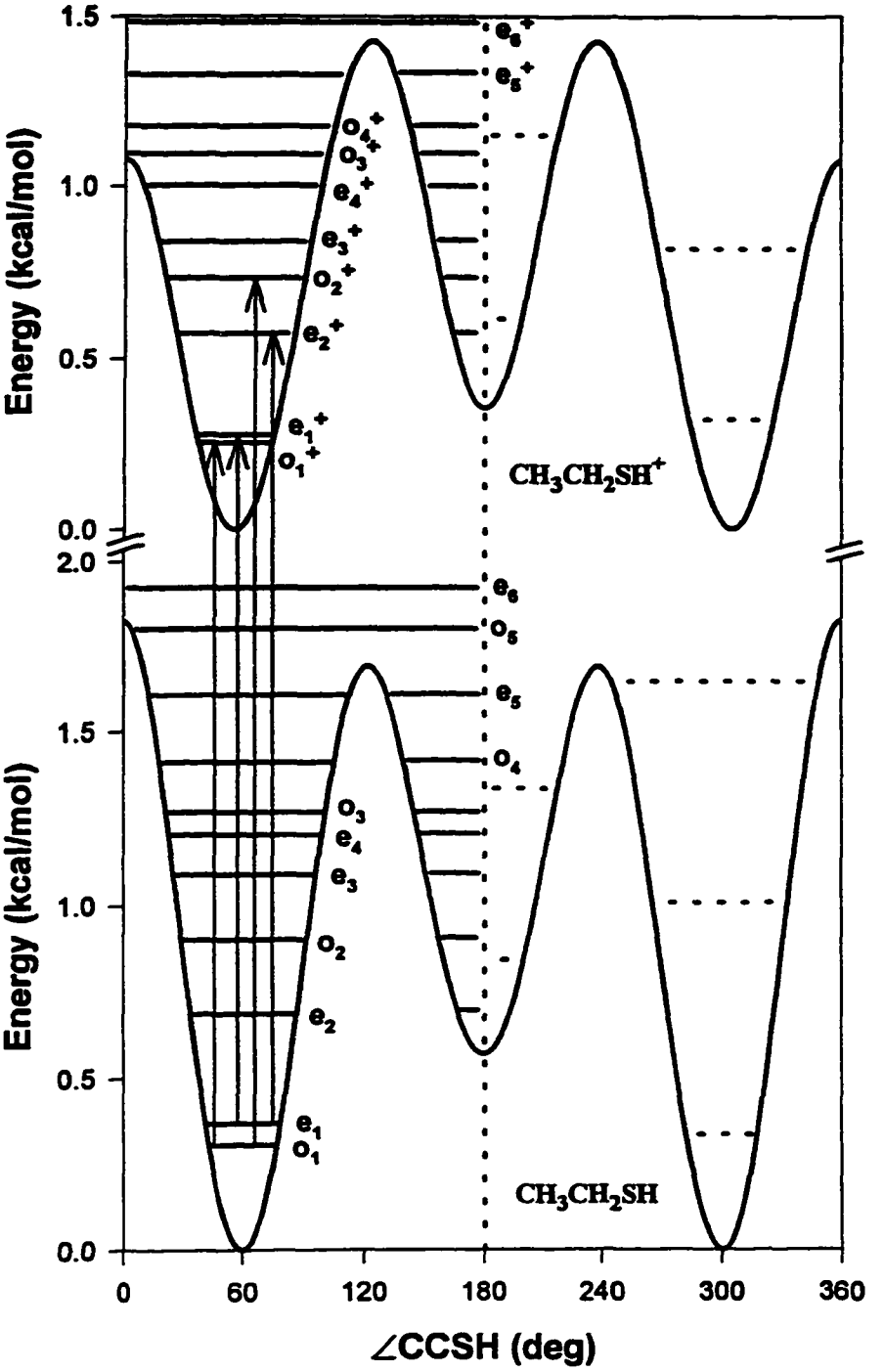

Fig. 2. Torsional potentials for CH_3CH_2SH (lower) and $CH_3CH_2SH^+$ (upper). The harmonic levels are shown by dashed lines and the levels obtained by solving Eq. (1) are shown as full lines. The energy scale is in kcal/mol and is measured with respect to the corresponding minimum of the potential well. Four allowed transitions from the o_l and e_l levels of CH_3CH_2SH are shown by vertical arrows.

The variational method is used to obtain the ground and excited vibrational state for the CH_3CH_2SH and $CH_3CH_2SH^+$ systems. Since $V(\phi)$ is an even function (symmetric about ϕ = 180°), each eigenfunction is either odd (o) or even (e). Furthermore, the potential has periodicity of 2π, so the sine and cosine functions are chosen for the basis sets. In this study, 50 sine functions [$\sin(n\phi)$, n = 1, 2, 3, ..., 50] and 50 cosine functions [$\cos(n\phi)$, n = 0, 1, 2, ..., 49] were used to obtain the odd and even eigenfunctions, respectively. Each matrix element consists of a kinetic energy integral and a potential energy integral. Since the basis functions are the eigenfunctions of the kinetic energy operator, the kinetic energy integrals are simply $n^2\hbar^2/2\mu$. The potential energy integrals are evaluated numerically using the Romberg algorithm implemented in the Mathcad Plus 6.0 software. Diagonalization are then performed to obtained the eigenvalues and hence the expansion coefficients.

The first few vibrational energy levels (full lines) are shown in Fig. 2 together with those obtained from the simple harmonic approximation (dashed lines) at the potential wells. The (even, odd) torsional levels for the neutral and cation are denoted as (e_n, o_n) and (e_n^+, o_n^+), n = 1, 2, 3, ..., respectively.

3. Results and discussion

3.1. CH_3SH^+

The equilibrium geometry of methyl mercaptan has C_s symmetry.[18] The values for the IE of CH_3SH obtained in previous photoionization and PE spectroscopic studies vary in the range from 9.438 to 9.46 eV.[19-23] The HeI PE spectra[22,23] and the photoelectron-photoion

coincidence (PEPICO) spectrum[20] for CH_3SH reveal a progression of vibrational peaks in the first electronic band. This progression has an average vibrational spacing of 647 ± 25 cm^{-1} and is attributed to excitation of the CH_3-SH^+ stretching mode.[20] Since the ionization of CH_3SH to form CH_3SH^+ in its ground state corresponds to the removal of a nonbonding electron from the S atom, the equilibrium geometries for CH_3SH and CH_3SH^+ are similar. For this reason, the vibrational progression of the first PE band is expected to be dominated by the 0-0 transition, which is consistent with experimental observations.[20,22,23]

Figures 3(a) and 3(b) show the N2P-PFI CH_3SH^+ ion and N2P-PFI-PE spectra for CH_3SH in the photon energy region of 75 600 - 77 400 cm^{-1} (2 × 37 800 – 2 × 38 700 cm^{-1}), respectively. These are the average of two reproducible scans. The peak positions of PE structures resolved in Fig 3(b) is reproducible within 1 cm^{-1}. The PFI-PE spectrum of Fig. 3(b), measured using a pulsed field of 2.4 V/cm, has not been corrected for the Stark shift of 4.2 cm^{-1}. The ion and PE spectra have not been normalized by the dye laser intensities. Since the experiment involves two-photon ionization, the ion and electron signals at corresponding photon energies should be normalized by the square of the dye laser intensities to yield the correct photoionization efficiency (PIE) and PE spectra. We find that the PIE and PE thus obtained are essentially the same as those shown in Fig. 3(a) and 3(b), except that the signal-to-noise ratios are poorer due to the fluctuation of the measured dye laser intensities. The fact that the ion and PE spectra observed here using the N2P ionization scheme are in good accord with the respective single VUV PIE spectrum and the PEPICO spectrum for CH_3SH[20] supports the conclusion that the spectra shown in Figs. 3(a) and 3(b) are not significantly affected by

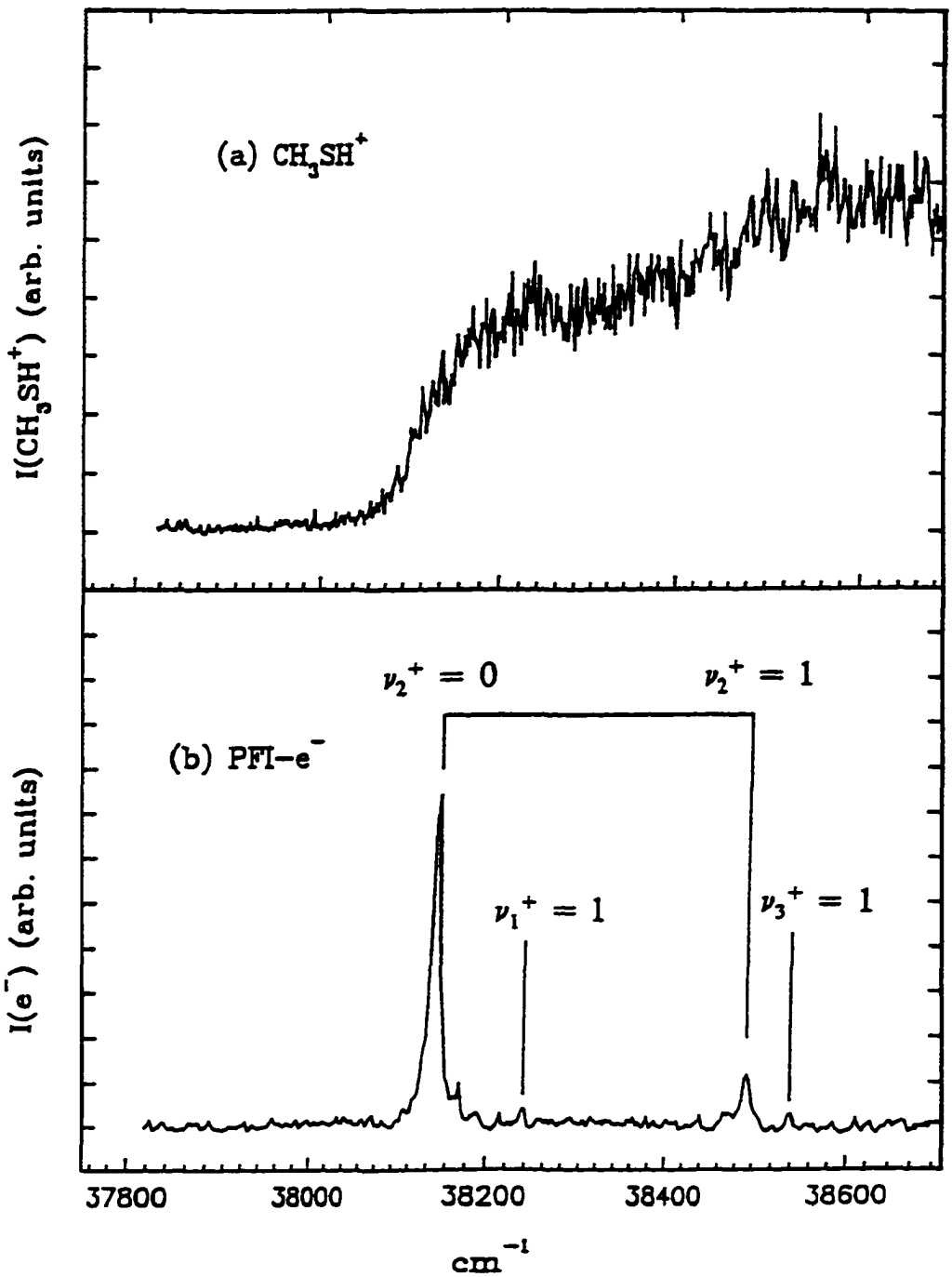

Fig. 3. (a) N2P CH_3SH^+ ion spectrum in the region 75 600-77 400 cm^{-1} (2 × 37 800-2 × 38 700 cm^{-1}) obtained using an electric field of 280 V/cm. (b) N2P-PFI-PE spectrum for CH_3SH in the region 75 600-77 400 cm^{-1} (2 × 37,800-2 × 38 700 cm^{-1}) obtained using a pulsed electric field of 2.4 V/cm. The PFI-PE spectrum has not been corrected for the Stark shift effect.

normalization of the dye laser intensities. We note that the resolution of the PFI-PE spectrum of Fig. 3(b) is more than 40 times better than that of the PEPICO spectrum.[20]

After taking into account the Stark shift of 4.2 cm^{-1}, the IE for CH_3SH, as marked by the strong PE peak of Fig. 3(b), is determined to be 76 302 ± 5 cm^{-1} (9.4602 ± 0.0006 eV). The half width for the PE peak is ≈ 12 cm^{-1}. The uncertainty of ±5 cm^{-1} for the IE accounts for the Stark shift and the reproducibility of the PE peak position. The latter is mostly determined by the laser photon energy resolution of 0.8 cm^{-1} used in this study. While the IE determined here is in agreement with the value (9.46 eV) determined in previous PEPICO[20] and PE spectroscopic studies,[23,24] it is higher than the value (9.44 eV) derived in previous PIE measurements.[20-22]

Since a repeller field of 280 V/cm is used, the onset of the CH_3SH^+ ion spectrum is expected to be affected considerably by the Stark shift effect. As shown in Fig. 3(a), the ionization onset of the N2P ion spectrum of CH_3SH is more than 80 cm^{-1} lower than the IE of CH_3SH determined by the first strong PE peak of the N2P-PFI-PE spectrum.

The G2 predictions for the IE of CH_3SH, and the $\Delta H°_{f0}$'s and E_o's for CH_3SH and CH_3SH^+ have been reported previously.[18] These predictions are compared to the present and previous[20-22,25] experimental findings in Table 2. As shown in the table, the IE(G2) value of 9.46 eV is in excellent agreement with the IE of CH_3SH (9.4602 ± 0.0006 eV) determined in the present study. Using this IE value and the known $\Delta H°_{f0}(CH_3SH)$ = -2.9 kcal/mol,[25] we obtain $\Delta H°_{f0}$ (CH_3SH^+) = 215.3 kcal/mol, which is also in excellent accord with the $\Delta H°_{f0}$(G2) value of 215.2 kcal/mol for CH_3SH^+.

Table 2
Total G2 energy [E_o(G2)], G2 and experimental heats of formation [$\Delta_f H°_0$(G2) and $\Delta_f H°_0$ (expt)] and G2 and experimental ionization energies [IE(G2) and IE(expt)][a]

	E_o(G2) (hartree)	$\Delta_f H°_0$ (G2) (kcal/mol)	$\Delta_f H°_0$ (expt) (kcal/mol)	IE(G2) (eV)	IE(expt)[b] (eV)
Neutrals					
CH_3SH	-438.14847[c]	-2.9[c]	-2.9[d]	9.46[c]	**9.4553 ± 0.0006** 9.468 ± 0.025[e] 9.446 ± 0.010[e] 9.44 ± 0.01[f] 9.438 ± 0.001[g]
gauche-$CH_3CH_2SH(C_1)$	-477.37504	-7.1	-	9.30	**9.2918 ± 0.0006** 9.285±0.005[d]
Trans-$CH_3CH_2SH(C_s)$	-477.37419	-6.6	-	9.28	-[h]
Cations					
CH_3SH^+	-437.80090[c]	215.2[c]	215.2[i]	-	-
Gauche-$CH_3SH_2SH^+(C_1)$	-477.03325	207.3	-	-	-
Trans-$CH_3SH_2SH^+(C_s)$	-477.03309	207.4	-	-	-

[a]Unless specified, the values given in the table are determined in this work.
[b]The recommended values are in bold font.
[c]Reference 18.
[d]Reference 25.
[e]Reference 20.

Table 2 (continued)

[f]Reference 21.
[g]Reference 22.
[h]The IE of CH_3CH_2SH determined here is assigned to that for the *gauche*-conformer. See the text.
[i]Value calculated using $\Delta_f H°_0(CH_3SH)$ = -2.9 kcal/mol and IE(CH_3SH) = 9.4553 ± 0.0006 eV.

The *ab initio* structures and vibrational frequencies for CH_3SH^+ obtained at the MP2/6-31G(d) level have been reported by Chiu *et al.*[18] As pointed out above, the ionization of CH_3SH in the first electronic band involves the removal an electron from the S atom. Although the electron ejected is mostly nonbonding in nature, it is still expected to affect the bonding parameters associated with the S atom, i.e., r(C-S), r(S-H) and $\angle$(C-S-H). The observation of the vibrational progression associated with the CH_3-SH^+ stretching mode in the PE spectrum of CH_3SH is consistent with this expectation. We show in Table 3 the MP2/6-31G(d) harmonic vibrational frequencies[18] for the torsional (a''), C-S stretching (a') and S-H bending (a') modes for comparison with the vibrational spacings observed in Fig. 3(b). These theoretical frequencies have been scaled by 0.93.[18] We have denoted the torsional, C-S stretching and S-H bending frequencies for CH_3SH^+ as ν_1^+, ν_2^+ and ν_3^+, respectively, in the order of increasing frequency.

The PE peak at 76,989 cm^{-1} [(2 × 38 492.3 + 4.2) cm^{-1}] resolved in Fig. 3(b), which is separated from the first PE peak by 687 ± 3 cm^{-1}, is assigned to excitation of the $\nu_2^+ = 1$ state of CH_3SH^+. This vibrational spacing is greater than the average spacing of 647 ± 25 cm^{-1} obtained in the previous PEPICO experiment.[20] The C-S stretching frequency of 687 ± 3 cm^{-1} for CH_3SH^+ observed here is in accord with the scaled MP2/6-31G(d) prediction of 678 cm^{-1}. A careful examination of the spectrum of Fig. 3(b) reveals two small peaks appearing at 76 480 cm^{-1} [(2 × 38 237.8 + 4.2) cm^{-1}] and 77084 cm^{-1} [(2 × 38 540 + 4.2) cm^{-1}]. These peaks are found in two independent scans and have signal-to-noise (S/N) ratios above the noise level. Since their spacings of 178 ± 3 and 782 ± 3 cm^{-1}, measured with respect to the IE of CH_3SH

Table 3
Comparison of theoretical and experimental vibrational frequencies for CH_3SH^+ and $CH_3CH_2SH^+$[a]

Assignment	Theoretical[b] (cm^{-1})	Experimental[c] (cm^{-1})
CH_3SH^+		
ν_1^+ [torsional (a")]	212	178[d] (w)
ν_2^+ [C-S stretch (a')]	678	687 (s)
ν_3^+ [S-H bend (a')]	770	782[d] (w)
gauche-$CH_3CH_2SH^+$		
ν_1^+ [Torsional]	174 (170)	
$e_1 \rightarrow e_2^+$	93[e]	116[d] (s)
$o_1 \rightarrow o_2^+$	169[e]	144[d] (s)
ν_3^+	289 (289)	288 (s)
ν_4^+ [C-S stretch]	615 (607)	628 (s)
ν_5^+	707 (676)	696 (w)
ν_9^+	1089(1080)	1058 (w)

[a]All MP2/6-31G(d) frequencies have been scaled by 0.93. The MP2/6-31G(d) frequencies for CH_3SH^+ are obtained from Ref. [18].
[b]Values in parentheses are scaled harmonic frequencies for *trans*-CH_3CH_2SH.
[c]The uncertainties for the vibrational spacings are ±3 cm^{-1}. w = weak and s = strong.
[d]Tentative assignments. See the text.
[e]Unscaled frequencies correspond to the ionization transitions $e_1 \rightarrow e_1^+$ and $o_1 \rightarrow o_1^+$. See the text.

(i.e., the peak position of the first strong PE peak), are in fair agreement with the scaled MP2/6-31G(d) torsional and S-H bending frequencies of 212 and 770 cm^{-1}, we tentatively assign these peaks to $\nu_1^+ = 1$ and $\nu_3^+ = 1$, respectively. A future experimental study with higher S/N ratios and higher energy resolution, together with a higher level theoretical study, is needed to confirm these assignments of ν_1^+ and ν_3^+.

3.2. $CH_3CH_2SH^+$

The success in identifying excitations of the torsional, C-S stretching and S-H bending vibrational modes of CH_3SH^+ is based on the expected structural change of CH_3SH upon removal of a mostly nonbonding electron from the S atom. As presented in the discussion below, this idea is extended to help assign the vibrational structures observed in the N2P-PFI-PE spectrum of CH_3CH_2SH.

In order to gain insight into the possible vibrational modes of $CH_3CH_2SH^+$ which may be excited in the ionization of CH_3CH_2SH, we show in Table 1 the computed differences in bond lengths (Δr) and in bond angles ($\Delta\angle$) between *gauche*-CH_3CH_2SH and *gauche*-$CH_3CH_2SH^+$ and between *trans*-CH_3CH_2SH and *trans*-$CH_3CH_2SH^+$. The most significant change in bond length upon ionization is that of the C-S bond, which is predicted to decrease by 0.02 Å. Thus, the C-S stretching vibration of $CH_3CH_2SH^+$ is expected to be excited. For the *gauche*-conformer, the change in the dihedral angle $\angle$C(3)-C(2)-S(1)-H(9), -4.9°, is also significant, suggesting excitation of the torsional mode. The changes of 1.9°-2.2° in $\angle$S(1)-C(2)-C(3) and 1.5°-2.0° in $\angle$C(2)-S(1)-H(9) indicate possible excitation of S-H and C-S

bending vibrations. Other changes in bond angles involving C and H atoms are necessary to balance the torsional and S-H and C-S bending vibrations involving the S atom.

Fig. 4 shows the N2P-PFI-PE spectrum for CH_3CH_2SH in the photon energy range of 74 600-76 400 cm^{-1} (2 × 37 300-2 × 38 200 cm^{-1}). Again, this spectrum has not been corrected for the Stark shift. The pulsed field used in measuring this spectrum is 3 V/cm, which corresponds to a Stark shift of ≈ 5 cm^{-1}. The PFI-PE signals have also not been normalized by the square of the dye laser intensities due to the poor signal-to-noise ratios of the measured laser intensities at photon energies >75 800 cm^{-1} (>2 × 37 900 cm^{-1}). Within experimental uncertainties, we find that the relative intensities for vibrational peaks observed in the normalized spectrum in the region of 74 600-75 800 cm^{-1} (>2 × 37 300-2 × 37 900 cm^{-1}) are similar to those shown in Fig. 4.

Similar to the N2P-PFI-PE spectrum for CH_3SH, the spectrum of Fig. 4 is dominated by the first vibrational PE peak at 37 469 cm^{-1}. After taking into account the Stark shift, the position of this peak corresponds to the two-photon energy of 74 943 ± 5 cm^{-1} (9.2918 ± 0.0006 eV) and marks the IE of CH_3CH_2SH. The observation of the dominant vibrational PE band at the IE is consistent with the expectation that the ionization of CH_3CH_2SH, as in the case of CH_3SH, involves the ejection of a mostly nonbonding electron associated with the S atom.

Using the G2 procedure, we have calculated the theoretical E_o, IE and $\Delta H°_{f0}$ values for *gauche*-CH_3CH_2SH and *trans*-CH_3CH_2SH, and the theoretical E_o and $\Delta H°_{f0}$ values for *gauche*-$CH_3CH_2SH^+$ and *trans*-$CH_3CH_2SH^+$. These values are listed in Table 2. Experimental $\Delta H°_{f0}$'s for these species are not available. The G2 calculation shows that *gauche*-CH_3CH_2SH is

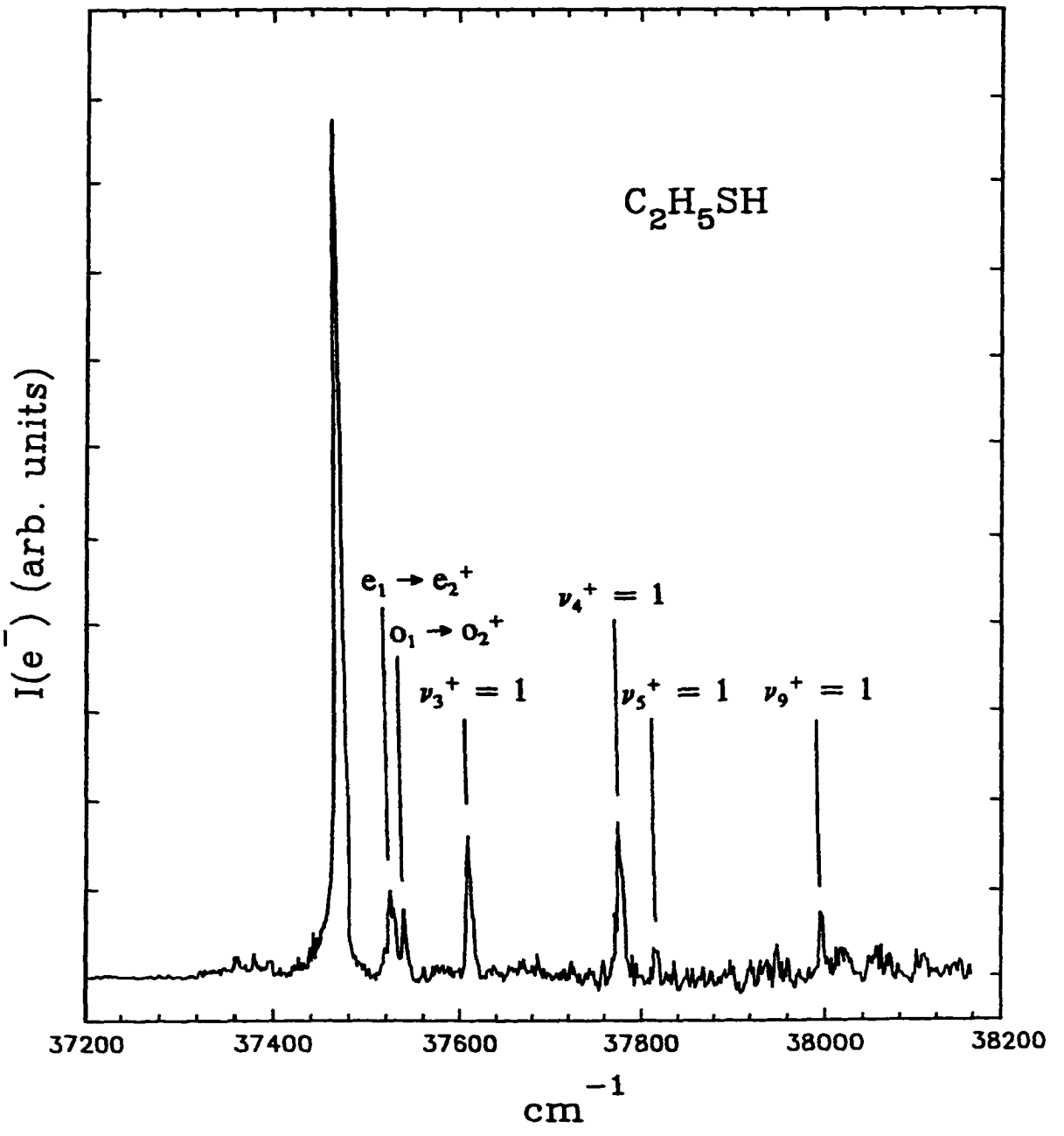

Fig. 4. N2P-PFI-PE spectrum for CH_3CH_2SH in the region 74 400-76 320 cm^{-1} (2 × 37 200-2 × 38 160 cm^{-1}) obtained using a pulsed electric field of 3 V/cm. The PFI-PE spectrum has not been corrected for the Stark shift effect.

more stable than *trans*-CH_3CH_2SH by 0.5 kcal/mol, while *gauche*-$CH_3CH_2SH^+$ is more stable than *trans*-$CH_3CH_2SH^+$ by only 0.1 kcal/mol. The G2 IEs for *gauche*-CH_3CH_2SH and *trans*-CH_3CH_2SH are 9.30 and 9.28 eV, respectively, which are in excellent agreement with the experimental value of 9.2918 eV. In a gas cell photoionization experiment, it would be difficult to distinguish the IEs of the *gauche*- and *trans*-conformers. In the beam expansion conditions used in this experiment, the vibrational temperature attained for CH_3CH_2SH should be in the range of 50-100K. The low vibrational temperature achieved in this study is shown by the negligible intensities for the hot bands observed below the IE of CH_3CH_2SH. Assuming that the prediction of the relative stabilities for *gauche*-Ch_3CH_2SH and *trans*-CH_3CH_2SH is correct, we estimate that <8% of the CH_3CH_2SH in the pulse supersonic jet has the *trans*-CH_3CH_2SH structure. On the basis of this estimate, we have assigned the experimental IE of 74 943 ± 5 cm^{-1} (9.2918 ± 0.0006 eV) determined here to be the IE of *gauche*-CH_3CH_2SH.

The positions of other weaker vibrational peaks, measured with respect to that of the first strong vibrational PE peak (i.e., the IE), are 116, 144, 288, 628, 696 and 1058 cm^{-1}. In view of the population analysis, which indicates that the population of *trans*-CH_3CH_2SH is insignificant in the pulsed supersonic beam, we attribute these vibrational peaks to excitation of the vibrational modes of *gauche*-$CH_3CH_2SH^+$. These spacings are compared to the scaled MP2/6-31G(d) harmonic frequencies for *gauche*-$CH_3CH_2SH^+$ in Table 3. The harmonic frequencies labeled ν_1^+, ν_3^+, ν_4^+, ν_5^+ and ν_9^+ in the table correspond to the lowest and the 3rd, 4th, 5th and 9th lowest frequencies of the 21 vibrational modes of *gauche*-$CH_3CH_2SH^+$. The scaled MP2/6-31G(d) harmonic frequencies for *trans*-$CH_3CH_2SH^+$ are similar to the corresponding harmonic frequencies of *gauche*-$CH_3CH_2SH^+$ (see values in parentheses in

Table 3). The scaled theoretical harmonic frequencies of $\nu_3^+ = 289$ cm^{-1}, $\nu_4^+ = 615$ cm^{-1}, $\nu_5^+ = 707$ cm^{-1} and $\nu_9^+ = 1089$ cm^{-1} for *gauche*-$CH_3CH_2SH^+$ match reasonably well with the experimental spacings of 288, 628, 696 and 1058 cm^{-1}, respectively. The lowest theoretical harmonic frequency for $\nu_1^+ = 174$ cm^{-1} corresponds to excitation of the torsional vibrational mode of *gauche*-$CH_3CH_2SH^+$. Near the expected ν_1^+ frequency, it is interesting that a doublet with spacings of 116 and 144 cm^{-1} measured with respect to the IE are observed in the PFI-PE spectrum of CH_3CH_2SH.

The harmonic vibrational motions for ν_1^+, ν_3^+, ν_4^+, ν_5^+ and ν_9^+ of *gauche*-$CH_3CH_2SH^+$ are depicted in Fig. 5, (a)-(e), respectively. As indicated above, ν_1^+ is the torsional mode which mainly involves the rotation of H around the C-S bond. The ν_3^+ mode involves S-H bending and the motion of the H's in the CH_3 group balances the S-H bending motion. The ν_4^+ mode corresponds to C-S stretching. Modes ν_5^+ and ν_9^+ also involve H-S bending. Both ν_1^+ and ν_5^+ change the dihedral angle $\angle$C(3)-C(2)-S(1)-H(9). The change in r(C-S) is mainly induced by ν_3^+. Modes ν_3^+, ν_5^+ and ν_9^+ change $\angle$C(3)-C(2)-S(1). These changes in bond lengths and bond angles induced by these vibrational modes are consistent with the more significant changes in bond lengths and bond angles associated with the S atom that occur when *gauche*-CH_3CH_2SH is ionized to form *gauche*-$CH_3CH_2SH^+$ in the ground state (see Δr and $\Delta\angle$ values in Table 1).

As pointed out above, the difference between the stabilities for *gauche*-CH_3CH_2SH and *trans*-CH_3CH_2SH (*gauche*-$CH_3CH_2SH^+$ and *trans*-$CH_3CH_2SH^+$) is predicted to be $\leq$ 0.5 kcal/mol ($\leq$ 0.1 kcal/mol), so we expect high anharmonicity for the torsional potential V(ϕ),

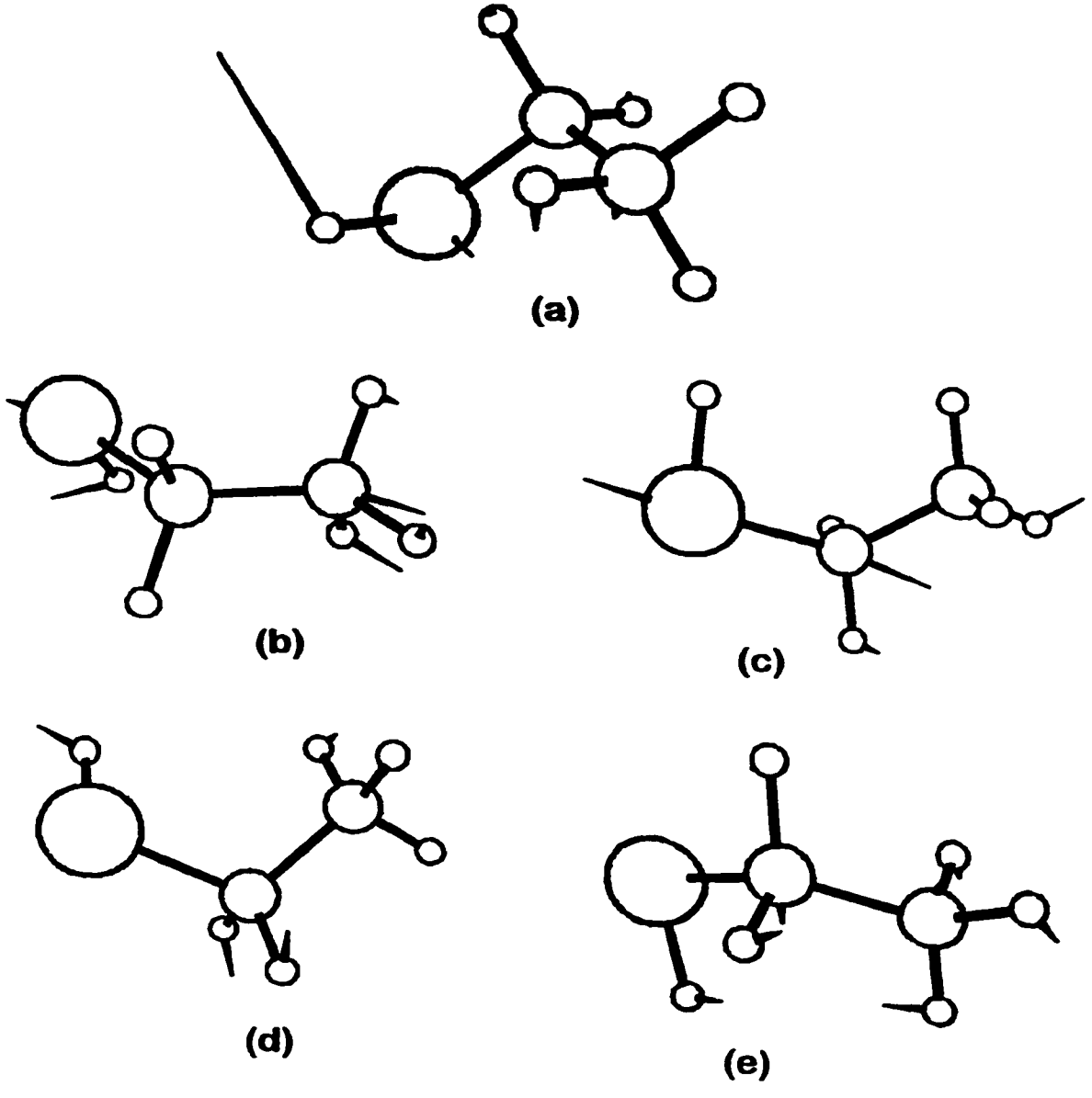

Fig. 5. Schematics showing the harmonic vibrations of *gauche*-CH_3CH_2SH: (a) ν_1^+ (torsional); (b) ν_3^+; (c) ν_4^+ (C-S stretch); (d) ν_5^+; and ν_9^+.

where ϕ is the dihedral angle $\angle$C(3)-C(2)-S(1)-H(9). As shown in Fig. 2, the potential barrier located at $\phi \approx 120°$, is $\approx$1.7 kcal/mol ($\approx$1.4 kcal/mol) for the CH_3CH_2SH ($CH_3CH_2SH^+$) system. Under the simple harmonic approximation, only the two or three lowest (torsional) vibrational states (shown by dashed lines) are classically bound by each potential well. The fact that the potential barrier heights are comparable to the vibrational quanta causes the harmonic levels in one potential well to mix with those in the others. Since $V(\phi)$ is symmetric about $\phi = 180°$, the actual (torsional) vibrational levels obtained by solving Eq. (1) are classified as odd or even levels (indicated by full lines in Fig. 2). At energies above the potential barrier, the system resembles a free rotating system whose energy levels (except the lowest one) are doubly degenerate.

The calculated energies for the five lowest (torsional) vibrational levels for CH_3CH_2SH (o_1, e_1, e_2, o_2 and e_3) and $CH_3CH_2SH^+$ (o_1, e_1, e_2, o_2 and e_3) are listed in Table 4. The energies of these levels are measured with respect to the corresponding potential wells at $\phi \approx 60°$. The three lowest states for CH_3CH_2SH are o_1, e_1 and e_2 with the energies of 109, 128 and 241 cm^{-1}, respectively. Assuming a vibrational temperature in the range of 50-100 K for the molecular beam, the respective populations for the e_1 and e_2 states are estimated to be 56-76% and 2.2-15% that of the ground o_1 state, respectively. On the basis of this analysis, we conclude that ionization from the o_1 and e_1 states is important, but ionization from the e_2 level can be neglected.

The probabilities of transitions between the vibrational states of the neutral and the cation are determined by the Franck-Condon factor (FCF), $|\langle \Psi | \Psi^+ \rangle|^2$, where Ψ and Ψ^+ are

Table 4
Theoretical energies for the (torsional) vibrational levels, transition energies and Franck-Condon factors for the $CH_3CH_2SH/CH_3CH_2SH^+$ system.

Torsional levels	ν(theo)[a] (cm^{-1})	$\Delta\nu$(theo)[b] (cm^{-1})	$\Delta\nu$(expt)[c] (cm^{-1})	FCF(theo)[d] (cm^{-1})	Estimated Intensity[e]
CH_3CH_2SH					
o_1	109	$o_1 \rightarrow o_1^+$: 0	0	0.962	1.00
e_1	128	$o_1 \rightarrow o_2^+$: 169	144[f]	0.036	0.04
e_2	241	$e_1 \rightarrow e_1^+$: -17	-	0.968	0.56-0.76
o_2	314	$e_1 \rightarrow e_2^+$: 93	116[f]	0.021	0.01-0.02
e_3	381	$e_1 \rightarrow e_3^+$: 186	-	0.002	0.001-0.002
$CH_3SH_2SH^+$					
o_1^+	89				
e_1^+	91				
e_2^+	201				
o_2^+	258				
e_3^+	294				

[a]Theoretical positions of (torsional) vibrational levels measured with respect to the respective potential wells.

[b]Theoretical transition energies measured with respect to the position of the transition line $o_1 \rightarrow o_1^+$, i.e., the transition energy for $o_1 \rightarrow o_1^+$ is taken as zero.

[c]Experimental transition energies measured with respect to the IE of *gauche*-CH_3CH_2SH.

[d]Franck-Condon factor = $|\langle\Psi|\Psi'\rangle|^2$ for the corresponding $\Delta\nu$ process, where Ψ and Ψ' are the (torsional) vibrational wavefunctions for the neutral and cation, respectively.

[e]The estimated intensities are calculated by taking the product of the relative population of o_1 or e_1 and the FCFs of the corresponding processes. The intensity for $o_1 \rightarrow o_1^+$ is normalized as to unity.

[f]The assignment of the 116 and 144 cm^{-1} to $e_1 \rightarrow e_2^+$ and $o_1 \rightarrow o_2^+$, respectively, are tentative. See the text.

the (torsional) vibrational wavefunctions of the neutral and cation, respectively. An immediate conclusion is that transition is allowed only between even states and between odd states. The numerical values of FCFs for the five lowest allowed transitions are shown in Table 4. As expected, the $o_1 \rightarrow o_1^+$ and $e_1 \rightarrow e_1^+$ transitions are dominant, with FCFs close to unity. The FCFs for $o_1 \rightarrow o_2^+$ and $e_1 \rightarrow e_2^+$ are significantly lower with only ≈ 4% and ≈ 2% those of the respective $o_1 \rightarrow o_1^+$ and $e_1 \rightarrow e_1^+$ transitions. For the $e_1 \rightarrow e_3^+$ transition the FCF falls to 0.002. The FCFs for ionization transitions from o_1 and e_1 to higher excited states of the cation are expected to be even lower. We estimate the relative intensity for an ionization transition by taking the product of the estimated population for o_1 or e_1 and the FCF of the process involved. The estimated relative intensities ($o_1 \rightarrow o_1^+$ normalized to unity) are given in Table 4.

Based on comparisons between the experimental [Δν(expt)] and theoretical transition energies [Δν(theo)], we assign the observed doublet at Δν(expt) = 116 and 144 cm^{-1} as due to the ionization transitions of $e_1 \rightarrow e_2^+$ and $o_1 \rightarrow o_2^+$, respectively. Taking into account the accuracy of the theoretical predictions, the Δν(theo) values of 93 and 169 cm^{-1} for the $e_1 \rightarrow e_2^+$ and $o_1 \rightarrow o_2^+$ transitions are in reasonable agreement with the corresponding Δν(expt) values. However, the relative intensities for $e_1 \rightarrow e_2^+ : o_1 \rightarrow o_2^+$, estimated to be ≈ 0.1-0.2 : 0.4 (Table 4), are not in accord with the experimental observation that shows the transition for Δν(expt) = 93 cm^{-1} is greater than that for Δν(expt) = 116 cm^{-1}. Because of the low intensities, the $e_1 \rightarrow e_3^+$ transition and transitions to higher excited cationic states may not be observable. The transition energy for $e_1 \rightarrow e_1^+$ is predicted to be -17 cm^{-1}, i.e., 17 cm^{-1} below the IE of CH_3CH_2SH. Since the strong PE peak at 76 302 cm^{-1} is contributed by many vibrational modes

and the width of this peak is broad, especially at the base, it is likely that the $e_1 \rightarrow e_1^+$ transition is unresolved and contributes to the low energy shoulder of the strong PE peak.

One of the difficult problems in the analysis of the vibrational structures of a polyatomic molecule, such as CH_3CH_2SH, is the hot band effects. The populations of low frequency vibrational modes of CH_3CH_2SH may give rise to vibrational hot bands below and above the IE. Judging from the observation that the intensities for vibrational hot bands below the IE of CH_3CH_2SH are significantly lower than the vibrational peaks of interest in this analysis, we have neglected the contribution of vibrational bands due to hot band excitations in our analysis.

The scaled MP2/6-31G(d) harmonic frequency for the CH_3 torsional mode of $CH_3CH_2SH^+$ is $\nu_2^+ \approx 230$ cm^{-1}, greater than scaled MP2/6-31G(d) harmonic frequency for S-H torsional mode ν_1^+ ($\approx$170 cm^{-1}) by $\approx$60 cm^{-1}. The respective methyl rotor potential energy barriers for CH_3CH_2SH and $CH_3CH_2SH^+$ are calculated to be 1.5 and 1.1 kcal/mol at the MP2/6-31G(d) level. These values are similar to the H-S torsional potential barriers for CH_3CH_2SH and $CH_3CH_2SH^+$. The current theoretical analysis of the doublet for the H-S torsional modes of the $CH_3CH_2SH/CH_3CH_2SH^+$ system has neglected the interaction between the CH_3 and H-S torsional motions. The failure of the analysis to reproduce the experimental doublet intensities for the H-S torsional mode suggests that a higher level of theoretical analysis of the observed H-S torsional vibrational excitations is required. A higher level theoretical analysis of the vibrational PE band structures should include the coupling of the methyl torsion and *gauche-trans* isomerization.[26] The degree of this coupling can be examined by comparing the high resolution PFI-PE spectra for CH_3CH_2SH, CD_3CH_2SH and CH_3CH_2SD in a future experiment. As shown in Tables 3 and 4, the predicted positions of the $e_1 \rightarrow e_2^+$ (93 cm^{-1}) and

$o_1 \rightarrow o_2^+$ (169 cm^{-1}) transitions differ from the respective experimental positions of 116 and 144 cm^{-1} by more than 20 cm^{-1}. Perhaps, a higher level theoretical simulation will also yield better agreement between the predicted and experimental PE band positions. For these reasons, we consider that the present assignment of the doublet to $e_1 \rightarrow e_2^+$ and $o_1 \rightarrow o_2^+$ as tentative.

4. Conclusion

We have obtained the PE spectra for CH_3SH and CH_3CH_2SH near their ionization thresholds using the N2P-PFI-PE spectroscopic techniques. These spectra yield highly accurate IEs for CH_3SH and CH_3CH_2SH. The G2 predictions of the IEs for these molecules are in excellent agreement with the experimental results. On the basis of the G2 theoretical analysis, we conclude that the IE of 74,943±5 cm^{-1} determined here for CH_3CH_2SH is due to the ionization reaction *gauche*-$CH_3CH_2SH + h\nu \rightarrow$ *gauche*-$CH_3CH_2SH^+ + e^-$.

By comparing the experimental PE vibrational spacings with the scaled MP2/6-31G(d) harmonic frequencies, we have assigned the vibrational features resolved in the PE spectra of CH_3SH and CH_3CH_2SH. All the vibrational PE bands observed in the PE spectra can be attributed to excitation of the torsional, C-S stretching and/or S-H bending vibrations of CH_3SH^+ and *gauche*-$CH_3CH_2SH^+$. This observation is consistent with the conclusion that the ionization of CH_3SH and CH_3CH_2SH involves the removal of an electron, mostly nonbonding in nature, from the S atom.

The torsional potentials for CH_3CH_2SH and $CH_3CH_2SH^+$ have been computed at the MP2/6-31G(d,p) level. A doublet observed for the torsional mode of $CH_3CH_2SH^+$ is attributed tentatively to transitions between torsional levels of CH_3CH_2SH and $CH_3CH_2SH^+$ arising from

the mixing of the harmonic frequencies due to the low torsional potential barriers between the *gauche*- and *trans*-conformers.

Acknowledgements

C.Y.N. is grateful to helpful discussion with Prof. J. Weisshaar. C.Y.N. acknowledges the donors of Petroleum Research Fund, administered by the American Chemical Society, for partial support of this research. W.K.L. is thankful for the support of a Hong Kong University and Polytechnic Grant Committee Earmarked Grant for research. S.W.C. acknowledges the use of computer time at the National Center for Supercomputing Applications of the University of Illinois at Champaign. Ames Laboratory is operated for the U. S. Department of Energy by Iowa State University under Contract No. W-7405-Eng-82. This article was supported by the Division of Chemical Sciences, Office of Basic Energy Science.

References

[1] K. Müller-Dethlefs, M. Sander and E. W. Schlag, Z. Naturforsch. A, 39 (1984) 1089.

[2] K. Müller-Dethlefs and E. W. Schlag, Annu. Rev, Phys. Chem., 42 (1991) 109.

[3] I. Powis, T. Baer and C. Y. Ng (Eds.), High Resolution Laser Photoionization and Photoelectron Studies, Wiley, Chichester, 1995, and references therein.

[4] A. Strobel, I. Fischer, J. Staecker, G. Niedner-Schatteburg, K. Müller-Dethlefs and V. E. Bondybey, J. Chem. Phys., 97 (1992) 2332.

[5] I. Fischer, A. Lochschmidt, A. Strobel, G. Niedner-Schatteburg, K. Müller-Dethlefs and V. E. Bondybey, J. Chem. Phys., 98 (1993) 3592.

[6] I. Fischer, A. Lochschmidt, A. Strobel, G. Niedner-Schatteburg, K. Müller-Dethelef and V. E. Bondybey, Chem. Phys. Lett., 202 (1993) 542.

[7] A. Strobel, A. Lochschmidt, I. Fischer, G. Niedner-Schatteburg and V. E. Bondybey, J. Chem. Phys., 99 (1993) 733.

[8] I. Fischer, A. Strobel, J. Staecher, G. Niedner-Schatteburg, K. Müller-Dethlefs and V. E. Bondybey, J. Chem. Phys., 96 (1992) 7171.

[9] G. Reiser, W. Habenicht and K. Müller-Dethlefs, J. Chem. Phys., 98 (1993) 8462.

[10] N. Knoblauch, A. Strobel, I. Fischer and V. E. Bondybey, J. Chem. Phys., 103 (1995) 5417.

[11] C.-W. Hsu, D. P. Baldwin, C.-L. Liao and C. Y. Ng, J. Chem. Phys., 100 (1994) 8047.

[12] C.-W. Hsu and C. Y. Ng, J. Chem. Phys., 101 (1994) 5596.

[13] L. A. Curtiss, K. Raghavachari, G. W. Truck and J. A. Pople, J. Chem. Phys., 94 (1991) 7221.

[14] L. A. Curtiss, L. D. Kock and J. A. Pople, J. Chem. Phys., 95 (1991) 4040.

[15] C.-W. Hsu, C.-L. Liao, Z.-X, Ma, P. J. H. Tjossem and C. Y. Ng, Chem. Phys. Lett., 199 (1992) 78.

[16] C. W. Hsu, C.-L. Liao, Z.-X. Ma, P.J. H. Tjossem and C. Y. Ng, J. Chem. Phys., 97 (1992) 6283.

[17] C. E. Moore, Atomic Energy Levels, Natl. Bur. Stand. (U.S.) Circ. No. 467, Vol. I, U.S. GPO, Washington, D.C. 1949.

[18] S.-W. Chiu, W.-K. Li, W.-B. Tzeng and C. Y. Ng, J. Chem. Phys., 97 (1992) 6557-6568.

[19] M. J. Frisch et al., GAUSSIAN 90, Gaussuan Inc., Pittsburgh, PA, 1990.

[20] S. Nourbakhsh, K. Norwood, H.-M. Yin, C.-L. Liao and C. Y. Ng, J. Chem. Phys., 95 (1991) 956.

[21] M. E. Akopyan, Y. L. Serhiev and F. I. Vilesov, Khim. Vys. Energy, 4 (1970) 305.

[22] R. E. Kutina, A. K. Edwards, G. L. Goodman and J. Berkowitz, J. Chem. Phys., 77 (1982) 5508.

[23] K. Kimura, S. Katsumata, Y. Achiba, T. Yamazaki and S. Iwata, Handbook of HeI Photoelectron Spectra of Fundamental Organic Molecules, Halsted, New York, 1981.

[24] D. C. Frost, F. G. Herring, A. Katrib, C. A. McDowell and R. A. N. McLean, J. Phys. 76 (1972) 1030.

[25] S. G. Lias, J. E. Bartmess, J. F. Liebman, J. L. Holmes, R. D. levin and W. G. Wallard, J. Phys. Chem. Ref. Data 17, Suppl. 1 (1988).

[26] We note that the H-S torsional potential shown in Fig. 2 has taken into account the relaxation of the methyl group, i.e., as the H-S group is rotated around the C-S bond, the CH_3 group is also allowed to rotate. Thus, the H-S and CH_3 torsional motions are coupled to some degree in the present treatment.

CHAPTER 3. NON-RESONANT TWO PHOTON PULSED FIELD IONIZATION PHOTOELECTRON STUDY OF CH_3CH_2S FORMED IN THE PHOTODISSOCIATION OF CH_3CH_2SH

A paper published in the Journal of Electron Spectrometry and Related Phenomena

Y.-S. Cheung, C.-W. Hsu and C. Y. Ng

Abstract

The non-resonant two photon pulsed field ionization photoelectron (N2P-PFI-PE) spectrum for CH_3CH_2S produced in the photodissociation of CH_3CH_2SH has been measured in the energy region of 2 × (36 160-37 200) cm^{-1}. The assignment of the N2P-PFI-PE spectrum indicates that both the $\tilde{X}\,^2A''$ and $\tilde{A}\,^2A'$ states for CH_3CH_2S are formed in the photodissociation of CH_3CH_2SH at $h\nu \approx 4.6$ eV. The ionization energies for transitions to $CH_3CH_2S^+(\tilde{X}\,^3A'')$ from the $\tilde{X}\,^2A''$ and $\tilde{A}\,^2A'$ states of CH_3CH_2S are determined to be 9.107 ± 0.004 and 9.077 ± 0.004 eV, respectively. The small energy gap of 0.030 ± 0.004 eV observed between the $\tilde{X}\,^2A''$ and $\tilde{A}\,^2A'$ states of CH_3CH_2S is consistent with the *ab initio* theoretical calculation.

1. Introduction

The pulsed field ionization (PFI) photoelectron (PFI-PE) method has been established to be an important technique for photoelectron spectroscopic studies [1, 2]. Photoelectron spectra with energy resolutions better than 1 cm^{-1} have been demonstrated using this method. Combining with the supersonic molecular beam technique, this method allows routine spectroscopic studies of polyatomic cations at the vibrationally resolved level [1]. For

diatomic and selected triatomic molecules, rotationally resolved spectroscopic studies of their cations can also be performed [1]. Despite the growing list of published PFI-PE spectra for molecules, only a few high resolution PFI-PE spectra for radical species have been reported [1, 3, 4]. In principle, radicals can be prepared by laser dissociation prior to PFI-PE measurements. This type of experiments would normally require at least two separate lasers [5]. Since many molecules are known to dissociate efficiently in the ultraviolet (UV) region [6], the steps involving radical preparation by photodissociation (using appropriate precursor molecules) and ionization via an N2P-PFI scheme can be achieved in a single UV laser shot. Such experiments, which involve the absorption of totally three UV photons, have been demonstrated in previous N2P-PFI-PE studies of SH from H_2S and CH_3S from CH_3SH (and CH_3SSCH_3) [3, 4]. In this report, we present a similar study of CH_3CH_2S prepared from the UV photodissociation of CH_3CH_2SH.

On the basis of the vacuum ultraviolet (VUV) photoionization mass spectrometric sampling of photoproducts formed in the 193-nm (ArF) photodissociation of $CH_3CH_2SCH_2CH_3$, along with *ab initio* calculations of C_2H_5S, Ma *et al.* [5] concluded that C_2H_5S radicals with the CH_3CH_2S structure are predominantly produced in such a photochemical process. The VUV photoionization efficiency (PIE) spectrum for CH_3CH_2S was recorded and a value of 8.97 ± 0.01 eV was determined for the ionization energy (IE) of CH_3CH_2S [5]. This value is found to be in good agreement with the theoretical GAUSSIAN-2 prediction of 9.07 eV [5]. In a recent laser induced fluorescence (LIF) study [7], CH_3CH_2S is shown to be produced predominantly in the 248-nm (KrF) laser photodissociation of

CH_3CH_2SH. This observation is consistent with the results of the 248-nm photodissociation of CH_3SH, where the CH_3S isomer is shown to be the dominant product [4, 6].

2. Experiment

The experimental apparatus used in this study has been described in detail [3, 4, 8]. It is modified from the laser ionization time-of-flight (TOF) mass spectrometer used in previous photodissociation studies [6, 9]. A two-stage microchannel plate detector and a set of simple aperture lenses for photoelectron detection have been added below the photoionization region and opposite to the ion TOF tube.

For this experiment, CH_3CH_2SH (99% pure) obtained from Aldrich is used without further purification. The CH_3CH_2SH sample is seeded in Ar carrier gas (sample : carrier gas $\approx$ 0.2 : 1.0) at a total stagnation pressure of $\approx$3.0 bar at 298 K. The gas mixture is introduced into the photoionization region by supersonic expansion through a pulsed valve with a nozzle diameter of 0.5 mm. The molecular beam is skimmed by a conical skimmer (1-mm diameter, 3.8 cm from the nozzle) before intersecting with a tunable laser beam (90°, 8.3 cm downstream from the skimmer). Both the pulsed valve and the dye laser operate at a repetition rate of 13 Hz.

The molecular beam source chamber is pumped by a freon-trapped, 6 in. diffusion pump (pumping speed $\approx$ 2000 l s^{-1}), while the photoionization chamber and the ion TOF tube are evacuated by two 50 l s^{-1} turbomolecular pumps. During the experiment, the beam source chamber and the photoionization chamber are maintained at pressures of about 1×10^{-4} and 2×10^{-6} torr, respectively.

The second harmonic output of an excimer (Lambda Physik EMG 201 MSC) pumped-dye laser (Lambda Physik FL 3002) is focused into the photoionization region by a 20-mm focal length fused-silica lens. Coumarin 153 dye is used to produce the fundamental output in the 524-542 nm region. Typical laser pulse energies used in the second harmonic output range of 262-271 nm are 1.2 mJ, as monitored with a pyroelectric detector. The wavelength calibration uses the known resonance-enhanced multi-photon ionization spectrum of atomic sulfur [10], which is also produced by the multi-photon laser photodissociation of CH_3CH_2SH.

Ion detection using the TOF mass spectrometer has been described in detail previously [9]. Here, a constant electric field of 280 V cm^{-1} is used to extract the ions formed in the photoionization region. The PFI-PE detection scheme relies on delayed PFI of long-lived high-n Rydberg states populated by laser excitation at a few wavenumbers below the ionization threshold [1, 2]. In this experiment, the firing of the photodissociation and excitation laser is delayed by 750 μs with respect to the triggering pulse for opening the pulsed valve. A 1-μs pulsed field of 3.1 V cm^{-1} is applied to the repeller plate 3 μs after firing the dye laser. The pulsed field field-ionizes the molecular species in high-n Rydberg states as well as extracts the electrons thus formed to the microchannel plate electron detector. The firing sequence of the pulsed valve, dye laser and pulsed electric field is controlled by two digital delay units (Stanford Research DG535). The electron signal from the electron detector and the laser energy signal from the pyroelectric detector are fed into two identical boxcar integrators (Stanford Research SR250), which are interfaced to an IBM/AT computer. The electron and laser energy signals are averaged for 30 shots at each laser wavelength.

The bandwidth of the dye laser is 0.2 cm^{-1} (full-width-at-half-maximum, FWHM) for the fundamental and ≈0.4 cm^{-1} (FWHM) for the second harmonic outputs. For a two-photon ionization process, the resolution due to the ionization laser is expected to be ≈ 0.8 cm^{-1} (FWHM).

3. Results and discussion

To a first approximation, the ground state of CH_3S belongs to the C_{3v} point group [4, 9] and has ^2E symmetry. As a result of the spin-orbit interaction, the ground and 1st excited states for CH_3S can be labeled as the $\tilde{X}\,^2E_{3/2}$ and $\tilde{A}\,^2E_{1/2}$ states, respectively. In the previous N2P-PFI-PE experiment, the IEs for the formation of $CH_3S^+(\tilde{X}\,^3A'')$ from the $\tilde{X}\,^2E_{3/2}$ and $\tilde{A}\,^2E_{1/2}$ states of CH_3S have been determined, yielding an accurate value for the spin-orbit splitting [4, 6]. Considering that CH_3CH_2S of C_s symmetry is formed by the substitution of a H atom in CH_3S with a CH_3 group, the degenerate ^2E ground state of CH_3S decomposes into the $\tilde{X}\,^2A''$ and $\tilde{A}\,^2A'$ states for CH_3CH_2S. The high-resolution LIF study of CH_3CH_2O indicates that the electronic ground state for CH_3CH_2O is $^2A''$ [11]. In the recent LIF study of CH_3CH_2S [7], together with MP2 *ab initio* calculation, the ground state of CH_3CH_2S is also assigned to be $^2A''$.

We have performed *ab initio* calculations to investigate the energies and geometries of the lowest two electronic states $CH_3CH_2S(\tilde{X}\,^2A'', \tilde{A}\,^2A')$ using the GAUSSIAN-94 suite of programs [12] installed at a Pentium personal computer. The geometry optimizations and frequency analysis were performed at the ROHF/6-31+G(d) level and energies were obtained

at the ROMP2(full)/6-311+G(d, p) level. At the ROHF/6-31+G(d) level, the *trans*-configuration (see Fig. 1) is the most stable structure at both electronic states. At the ROMP2(full)/6-311+G(d,p)//ROHF/6-31+G(d) level, the electronic energy of the $^2A''$ state is 0.06 eV lower than the $^2A'$ state. When zero-point vibrational energy (ZPVE) (scaled by 0.8929) is included, however, the $^2A'$ state becomes more stable (by 0.08 eV) due to the smaller ZPVE of the $^2A'$ state. The ZPVE is known to be subject to a large uncertainty. In this case, the energy gap between the $^2A''$ and $^2A'$ states of CH_3CH_2S apparently lies in the range of uncertainties of the ZPVE calculation.

The dominant electronic configuration for the $^2A''$ and $^2A'$ states of CH_3CH_2S are shown to be $...(12a')^2(13a')^2(4a'')^1$ and $...(12a')^2(13a')^1(4a'')^2$, respectively [7]. As shown in Fig. 1, the 13a′ molecular orbital corresponds to the p_x orbital of S lying in the C-C-S plane, while the 4a″ orbital is the p_y atomic orbital of S oriented perpendicularly to the C-C-S plane. Since the p_x and p_y orbitals of the S atom are essentially nonbonding in nature, the energy separation between the $^2A''$ and $^2A'$ states is expected to be small. In spite of the uncertainty of the *ab initio* calculation described above, we may conclude that this energy separation is likely to be ≈0.1 eV. Following the conclusion of previous LIF experiments [7, 11], we assign $^2A''$ as the ground state for CH_3CH_2S.

The N2P-PFI-PE spectrum for CH_3CH_2S in the energy region of 2 × (36 160-37 200) cm^{-1} [or 2 × (4.483-4.612) eV] is shown in Fig. 2. The spectra of Figs. 2(a) and 2(b) represent two independent scans. Assuming that the formation of $CH_3CH_2S^+ + e^-$ from CH_3CH_2SH is a three-photon process, we have normalized the PFI-PE signal [I(e^-)] by

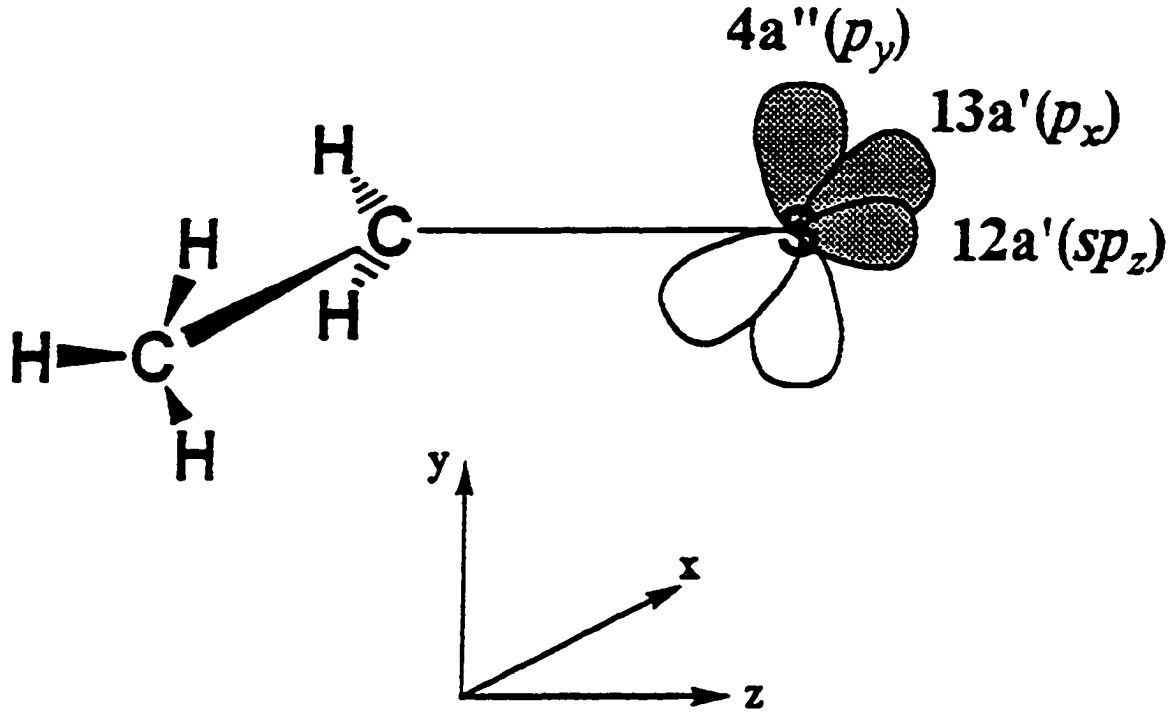

CH_3CH_2S (C_s)

Fig. 1. Schematic diagram showing the geometry of *trans*-CH_3CH_2S. The 13a′ and 4a″ molecular orbitals for CH_3CH_2S are identified as the respective p_x and p_y atomic orbitals of the S atom.

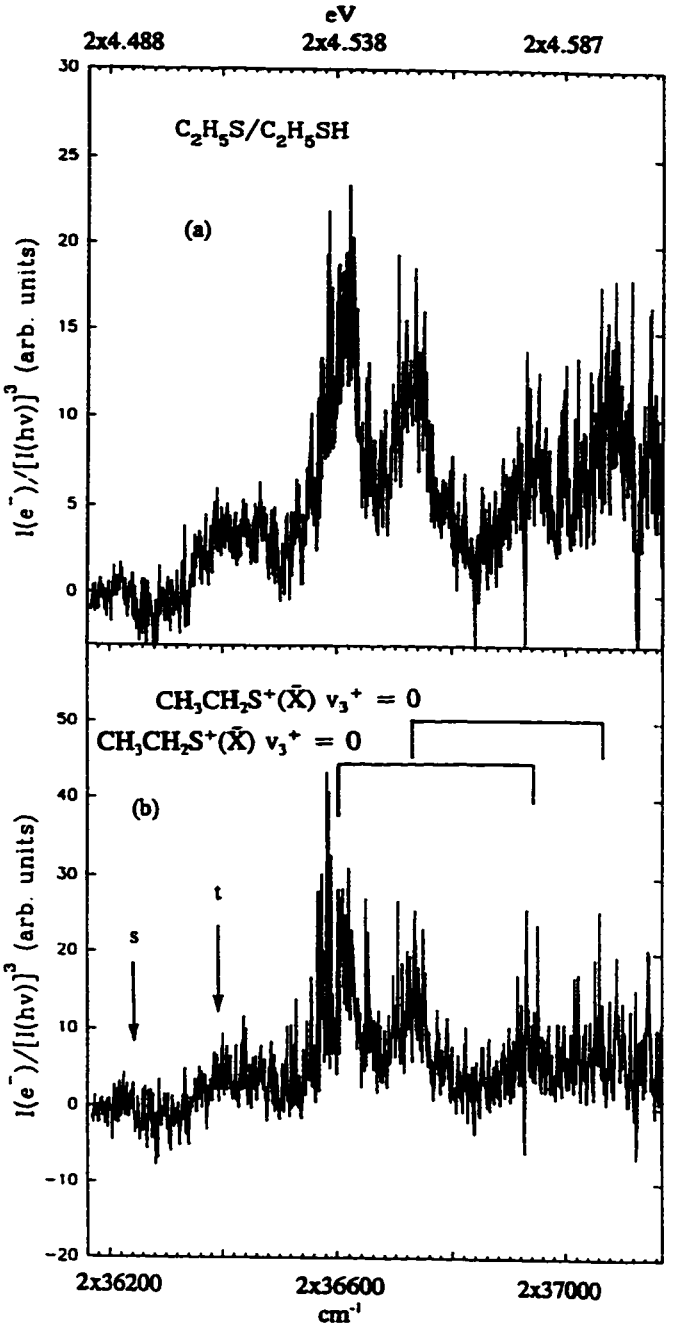

Fig. 2. (a) and (b) are the N2P-PFI-PE spectra for CH_3CH_2S measured in two independent scans in the energy region of 2 × (36 160-37 200) cm^{-1} [or 2 × (4.483-4.612) eV]. Note that the PFI-PE signal [I(e^-)] is normalized by $[I(h\nu)]^3$, where I((hν) is the laser energy signal. The arrows marked by "t" and "s" correspond to the ionization transitions $CH_3CH_2S[\tilde{X}\,^2A''$, $\nu(C\text{-}S) = 1] \rightarrow CH_3CH_2S^+(\tilde{X}\,^3A'')$ and $CH_3CH_2S\ [\tilde{A}\,^2A'$, $\nu(C\text{-}S) = 1] \rightarrow CH_3CH_2S^+(\tilde{X}\,^3A'')$, respectively.

$[I(h\nu)]^3$, where I(hν) is the laser energy signal. The spectrum of Fig. 2(a) was recorded at a higher laser power and thus achieved a better signal-to-noise ratio than that of Fig. 2(b). The weak band at 2 × 37 060 cm^{-1} is more visible in the spectrum of Fig. 2(a). However, we believe that Fig. 2(b) shows the correct relative PFI-PE band intensities based on comparison with other experimental scans. We note that efforts made to record the N2P-PFI PIE spectrum of CH_3CH_2S were unsuccessful. The focusing of the UV laser beam as required in the present experiment may induce the absorption of additional photon(s) by $CH_3CH_2S^+$ initially formed via the N2P-PFI process. This excitation is expected to cause further fragmentation, depleting the observable $CH_3CH_2S^+$ signal.

The two dominant peaks observed at 9.107 and 9.077 eV have a width of ≈0.008 eV and are assigned as the formation of the $CH_3CH_2S^+(\tilde{X}\,^3A'')$ ground state from the vibrational ground states of $CH_3CH_2S(\tilde{X}\,^2A'')$ and $CH_3CH_2S(\tilde{A}\,^2A')$, respectively. Two weaker peaks at energies 670 ± 30 cm^{-1} higher than the two dominant peaks are discernible in the spectra of Figs. 2(a) and 2(b). The splitting of the weak peaks is similar to that of the dominant peaks. Since the formation of $CH_3CH_2S^+$ involves the ionization of a nonbonding electron mostly localized at the S atom, the C-S bond is expected to be excited during the ionization process. These weaker peaks can thus be attributed to the formation of $CH_3CH_2S^+(\tilde{X}\,^3A'', \nu^+ = 1)$ from $CH_3CH_2S(\tilde{X}\,^2A'')$ and $CH_3CH_2S(\tilde{A}\,^2A')$, where ν^+ represents the vibrational quantum number for the C-S stretching mode of $CH_3CH_2S^+$. This assignment is supported by the *ab initio* [HF/6-31G(d)] frequency of 683 cm^{-1} for ν^+ obtained in the present study. The $IE[CH_3CH_2S(\tilde{X}\,^2A'')] = 9.107 \pm 0.004$ eV and $IE[CH_3CH_2S(\tilde{A}\,^2A') = 9.077 \pm 0.004$ eV

obtained here are in good agreement with the previous experimental and theoretical results of 8.97 ± 0.01 and 9.07 eV, respectively [5]. The energy gap between the $CH_3CH_2S(\tilde{X}^2A'')$ and $CH_3CH_2S(\tilde{A}^2A')$ is determined to be 0.030 ± 0.004 eV. Such a small value is consistent with the theoretical calculations as stated above. Figs 2(a) and 2(b) seem to reveal other reproducible fine structures. However, the clear identification of these structures requires further studies at better signal-to-noise ratios.

This assignment of the N2P-PFI-PE spectra of Figs. 2(a) and 2(b) suggests that the CH_3CH_2S radical is produced at both the $\tilde{X}^2A''$ and $\tilde{A}^2A'$ states in the 248-nm photodissociation of CH_3CH_2SH. Assuming that the ionization cross-sections for $CH_3CH_2S(\tilde{X}^2A'')$ and $CH_3CH_2S(\tilde{A}^2A')$ states are identical, the N2P-PFI-PE spectrum shows that the population for $CH_3CH_2S(\tilde{X}^2A'')$ is less than that for $CH_3CH_2S(\tilde{A}^2A')$ by 30-50%. Although a detailed theoretical study has not been made on the photofragmentation of CH_3CH_2SH, the formation of CH_3CH_2S + H may result from excitation of a nonbonding electron at the sulfur atom to the anti-bonding orbital of the S-H bond in the parent molecule followed by a prompt S-H bond cleavage. As demonstrated in the formation of CH_3S from the UV photodissociation of CH_3SH, the ejection of the light H atom results in a low rotational excitation for the heavier CH_3S fragment.[4] Thus, we expect that CH_3CH_2S radicals formed in the UV photodissociation of CH_3CH_2SH contain low rotational energies. This expectation is confirmed by the narrow FWHM (≈30-50 cm^{-1}) observed for vibrational peaks in the PFI-PE spectrum, which can be used to estimate the rotational excitation of CH_3CH_2S.

The LIF study of CH_3CH_2S prepared in the 248-nm photodissociation of CH_3CH_2SH reveals prominent vibrational hot bands associated with the CS-stretching [ν(C-S)] and CCS-bending modes of CH_3CH_2S at 672.4 and 296.0 cm^{-1}, respectively.[7] The expected positions of the hot band ionization transitions, $CH_3CH_2S[\tilde{X}\,^2A'', \nu(C\text{-}S) = 1] \rightarrow CH_3CH_2S^+(\tilde{X}\,^3A'')$ and $CH_3CH_2S[\tilde{A}\,^2A', \nu(C\text{-}S) = 1] \rightarrow CH_3CH_2S^+(\tilde{X}\,^3A'')$ are marked by the arrows labeled as "t" and "s" in Fig. 2(b). The ionization hot bands due to excitation of the CCS-bending mode of CH_3CH_2S are also expected to exist. Although weak PFI-PE peaks seem to exit at the expected positions of the hot bands associated with the CS-stretching vibration of CH_3CH_2S, we consider this correlation tentative because of the poor signal-to-noise ratios of the experimental spectra shown in Figs. 2(a) and 2(b).

4. Conclusion

The N2P-PFI-PE study reported here shows that the ratio for the population of the ground $\tilde{X}\,^2A''$ state to that of the first excited $\tilde{A}\,^2A'$ electronic state is ≈0.6 for CH_3CH_2S formed in the UV photodissociation of CH_3CH_2SH. The IEs of CH_3CH_2S at the $\tilde{X}\,^2A''$ and $\tilde{A}\,^2A'$ states were determined to be 9.077 ± 0.004 eV and 9.107 ± 0.004 eV, respectively. This leads to a value of 0.030 ± 0.004 eV for the energy gap between the $\tilde{X}\,^2A''$ and $\tilde{A}\,^2A'$ states. The experimental value of 670 ± 30 cm^{-1} for the CS-stretching mode of $CH_3CH_2S^+$ is in agreement with the HF/6-31G(d) theoretical value of 683 cm^{-1}.

Acknowledgement

This work was supported by the Director, Office of Energy Research, Office of Basic Energy Sciences, Chemical Sciences Division of the U. S. Department of Energy under Contract No. W-7405-Eng-82 for the Ames Laboratory. YSC was the 1997 Gilman Fellowship and Nelson Chemistry Scholarship recipients at Iowa State University.

References

[1] K. Müller-Dethlefs, E. W. Schlag, Ann. Rev. Phys. Chem. 42 (1991) 109.

[2] I. Powis, T. Baer, C. Y. Ng, High Resolution Laser Photoionization and Photoelectron Studies, Wiley Series in Ion Chemistry and Physics, Wiley, Chichester, 1995.

[3] C.-W. Hsu, D. P. Baldwin, C.-L. Liao, C. Y. Ng, J. Chem. Phys. 100 (1994) 8047.

[4] C.-W. Hsu, C. Y. Ng, J. Chem. Phys. 101 (1994) 6696.

[5] Z.-X. Ma, C.-L. Liao, H.-M. Yin, C. Y. Ng, S.-W. Chiu, I. Ma, W.-K. Li, Chem. Phys. Lett. 213 (1993) 250.

[6] C. Y. Ng, Adv. Photochemistry, vol 22, Wiley, New York, 1997, pp. 1-116.

[7] W.-C. Hung, M.-Y. Shen, C.-H. Yu, Y.-P. Lee, J. Chem. Phys. 105 (1996) 5722.

[8] Y.-S. Cheung, C.-W. Hsu, J.-C. Huang, C. Y. Ng, W.-K. Li, S.-W. Chiu, Int. J. Mass Spectrom. Ion Processes 159 (1996) 13.

[9] C.-W. Hsu, C.-L. Liao, Z.-X. Ma, P. J. H. Tjossem, C. Y. Ng, J. Chem. Phys. 97 (1992) 6283.

[10] C. E. Moore, Atomic Energy Levels, National Bureau of Standard (US) Cir. 467, vol. 1, US GPO, Washington, DC 1949.

[11] X. Q. Tan, J. M. Williamson S. C. Foster, T. A. Miller, J. Phys. Chem. 97 (1993) 9311.

[12] Gaussian 94, Revision B.2, M. J. Frisch, G. W. Trucks, H. B. Schlegel, P. M. W. Gill, B. G. Johnson, M. A. Robb, J. R. Cheeseman, T. Keith, G. A. Petersson, J. A. Montgomery, K. Raghavachari, M. A. Al-Laham, V. G. Zakrzewski, J. V. Ortiz, J. B. Foresman, C. Y. Peng, P. Y. Ayala, W. Chen, M. W. Wong, J. L. Andres, E. S. Replogle, R. Gomperts, R. L. Martin, D. J. Fox, J. S. Binkley, D. J. Defrees, J. Baker, J. P. Stewart, M. Head-Gordon, C. Gonzalez, J. A. Pople, Gaussian, Inc., Pittsburgh PA, 1995.

CHAPTER 4. A HIGH RESOLUTION VUV PHOTOIONIZATION, PHOTOELECTRON AND PULSED FIELD IONIZATION STUDY OF CS_2 NEAR THE $CS_2^+(X^2\Pi_{3/2,1/2})$ THRESHOLDS

A paper published in the Journal of Chemical Physics

J.-C. Huang, Y.-S. Cheung, M. Evans, C.-X. Liao, C. Y. Ng, C.-W. Hsu, P. Heimann, H. Lefebvre-Brion and C. Cossart-Magos

ABSTRACT

High resolution photoionization efficiency (PIE) and pulsed field ionization photoelectron (PFI-PE) spectra for CS_2 have been measured using coherent vacuum ultraviolet (VUV) laser radiation in the energy range of 81 050-82 100 cm^{-1}. The PIE and threshold photoelectron (TPE) spectra for CS_2 in the energy range of 80 850-82 750 cm^{-1} have also been obtained using synchrotron radiation for comparison with results of the VUV laser study. The analysis of the PIE spectra reveals three Rydberg series converging to the excited $CS_2^+(^2\Pi_{1/2})$ spin-orbit state. These series, with quantum defects of 1.430, 1.616 and 0.053, are associated with the $[^2\Pi_{1/2}]np\sigma_u$, $[^2\Pi_{1/2}]np\pi_u$ and $[^2\Pi_{1/2}]nf_u$ configurations, respectively. The Stark shift effect on the ionization threshold of CS_2 has been examined as a function of dc electric fields (F) in the range of 0.65-1071 V/cm. The observed F dependence of the Stark shift for the ionization onset of CS_2 is consistent with the prediction by the classical adiabatic field ionization formula. The extrapolation of the ionization onset to zero F yields accurate values for $IE[CS_2^+(^2\Pi_{3/2})]$. This study shows that in order to determine accurate IEs and to probe autoionizing structures for molecular species by PIE measurements, it is necessary to minimize the electric field used for ion extraction. The assignment of Renner-Teller structures resolved

in the VUV PFI-PE spectrum is guided by the recent non-resonant two-photon (N2P) PFI-PE and theoretical studies. The analysis of the PFI-PE spectrum also yields accurate values for IE[$CS_2^+(^2\Pi_{3/2,1/2})$]. Taking the average of the IE values determined by VUV-PFI-PE, N2P-PFI-PE and Stark field extrapolation methods, we obtain a value of 81 285.7 ± 2.8 cm^{-1} for IE[$CS_2^+(^2\Pi_{3/2})$]. For IE[$CS_2^+(^2\Pi_{1/2})$], we recommend a value of 81 727.1 ± 0.5 cm^{-1} determined by the Rydberg series analysis. A theoretical simulation of the $^2\Pi_{3/2}(0_0^0)$ and $^2\Pi_{1/2}(0_0^0)$ VUV-PFI-PE band profiles reproduces the observed branching ratio of 1.9 ± 0.3 for $CS_2^+(^2\Pi_{3/2})/CS_2^+(\tilde{X}\,^2\Pi_{1/2})$. The relative intensities of vibronic structures observed in the VUV PFI-PE and TPE spectra are in agreement. Evidence is found, indicating that the strongly (Stark field induced) autoionizing Rydberg state, $17p\sigma_u$, which is ≈10 cm^{-1} below the IE of CS_2, has a minor contribution to the observed profile for the $\tilde{X}\,^2\Pi_{3/2}(0_0^0)$ PFI-PE band.

I. INTRODUCTION

Vacuum ultraviolet (VUV) photoionization mass spectrometry (PIMS) and threshold photoelectron (TPE) spectroscopy are important experimental techniques for the studies of photoionization-photoelectron dynamics and cation energetics.[1] These studies in the past have mainly relied on laboratory discharge and synchrotron radiation sources.[1,2] However, the low VUV intensities obtainable from traditional laboratory discharge lamps and second generation synchrotron radiation sources have limited the achievable resolution in most previous photoionization and TPE studies to ≈3-30 meV. The recent developments of coherent VUV lasers[3-8] and third generation synchrotron radiation sources, coupled with an insertion device,

such as an undulator,[9-11] promise to significantly improve the resolution in PIMS and TPE studies.[12]

Recently, a VUV monochromatized undulator synchrotron source associated with the Chemical Dynamics Beamline has been developed at the Advanced Light Source (ALS) of the Lawrence Berkeley National Laboratory.[11,13] By connecting a 6.65 m off-plane Eagle mounted scanning monochromator to the third generation synchrotron radiation source equipped with an undulator (10 cm period), it has been demonstrated that usable monochromatic VUV radiation with photon energy bandwidths of ≈1-2 cm^{-1} (FWHM) can be achieved.[9-11] We note that the undulator synchrotron radiation at ALS is 99% polarized. In additional to its high resolution capability, the major advantage of a synchrotron source, such as that of ALS, is the ease in tunability covering the full 6-24 eV photon energy range. When operated in the multi-bunch mode, a synchrotron source provides essentially cw radiation.[14]

Comparing the achievable energy resolutions, coherent VUV lasers are superior to synchrotron radiation sources. The generation of coherent VUV laser radiation in the energy range of 6.5-19 eV by four-wave mixing schemes in rare gases and in metal vapors can now be made routinely.[3-8,15,16] Using commercial dye lasers with resolutions of 0.03-0.2 cm^{-1} (FWHM) in the visible photon energy range, the resolution for VUV generated by nonlinear mixing is expected to be in the range of 0.1-1.0 cm^{-1}.[3,8] A VUV laser system constructed using high resolution lasers has also been demonstrated, providing transform-limited spectral resolution.[4-7] Since a VUV laser system can be operated in individual laboratories, it is certain that VUV lasers will replace laboratory discharge lamps in laboratory photochemical studies.

Parallel to the development of high brightness VUV light sources, much technical progress has also been made in high resolution photoelectron spectroscopy.[12,17,18] A high resolution cw monochromatized synchrotron source is well-suited for TPE and photoelectron-photoion coincidence (PEPICO) studies.[1] The resolution of traditional TPE methods is mostly limited by the photon energy bandwidth.[19] We expect that TPE and PEPICO studies can be made routinely at a resolution <3 meV using the ALS undulator synchrotron light sources. In a recent TPE study using a monochromatized synchrotron source with a wavelength resolution of 0.03 Å (FWHM), a resolution of ≈1 meV for TPE measurements has been demonstrated.[20]

With the introduction of the laser pulsed field ionization photoelectron (PFI-PE) method,[17,18] the energy resolution for photoelectron spectroscopy has been improved to sub-wavenumbers, approaching that achieved in optical spectroscopy. The pulsed nature of a coherent VUV laser source makes it a natural photoionization source for time-of-flight (TOF) mass spectrometry and PFI-PE spectroscopy studies.[12] It has been shown that a synchrotron radiation source, when operated in a few bunch mode, can also be used for PFI-PE studies.[21,22] Recently, methods have also been introduced for the measurements of mass analyzed threshold ions (MATI) formed in the Stark field ionization of high-n Rydberg species prepared by excitation using VUV laser[23-27] or cw synchrotron radiation.[10] The advancement of the PFI-PE and MATI techniques are the most exciting developments in the field of VUV photoionization-photoelectron spectroscopy.

In this article, we present the results of a high-resolution photoionization efficiency (PIE) and PFI-PE study of CS_2 near the $CS_2^+(\tilde{X}\,^2\Pi_{3/2,1/2})$ thresholds using VUV laser techniques. The PIE and TPE spectra for CS_2 have also been measured using the

monochromatized undulator synchrotron source at ALS for comparison with results of the VUV laser study. As shown below, the VUV laser and ALS synchrotron experiments provide complementary information about the energetics and dynamics for the photoionization of CS_2.

When an autoionization Rydberg series is resolved in a high resolution PIMS experiment, covering a sufficiently large number of high-*n* Rydberg states, the analysis of these Rydberg states can lead to a highly accurate converging limit or IE. As a result of strong predissociation of high Rydberg polyatomic molecules formed in VUV excitation, autoionizing Rydberg features for polyatomic species are often not observable in PIE measurements. In such a case, IE values for the ground and/or excited vibronic states of a polyatomic species may be determined by the step-like onsets observed in the PIE spectrum. We note that strong autoionizing structures may obscure step-like onsets revealing the formation of excited ionic states. The PIE spectrum of CS_2 near the $CS_2^+(\tilde{X}\,^2\Pi_{3/2,1/2})$ thresholds exhibits both rich autoionization features and step-like structures.[28,29]

The IE$[CS_2^+(\tilde{X}\,^2\Pi_{3/2,1/2})]$ values determined by the step-like structures in previous high resolution PIE experiments[28,29] are lower than those obtained by photoelectron spectroscopy studies.[30-33] This discrepancy is most likely caused by the Stark field ionization effect.[34] Furthermore, the IE$[CS_2^+(^2\Pi_{1/2})]$ value deduced by the previous Rydberg series analysis[35] is not in agreement with those of the PIE[28,29] and photoelectron spectroscopy[30-33] studies. For this reason, we have measured the Stark shift of the photoionization onsets of CS_2 as a function of electrostatic ion extraction field. Through a careful examination of the IE$[CS_2^+(\tilde{X}\,^2\Pi_{3/2,1/2})]$ values determined by the VUV PIE, TPE, PFI-PE and Stark shift extrapolation methods, we

have obtained consistent and more accurate IE values for the formation of $CS_2^+(\tilde{X}\,^2\Pi_{3/2,1/2})$ from $CS_2(\tilde{X}\,^1\Sigma_g^+)$.

The ground state of CS_2 is linear with the dominant electronic configuration:[36]

$$...(5\sigma_g)^2(4\sigma_u)^2(6\sigma_g)^2(5\sigma_u)^2(2\pi_u)^4(2\pi_g)^4\ \tilde{X}\,^1\Sigma_g^+$$

The first vibrational excited levels for the symmetric stretch (ν_1), degenerate bend (ν_2) and asymmetric stretch (ν_3) of the $CS_2(\tilde{X}\,^1\Sigma_g^+)$ state are known to be 658.00, 395.99 and 1535.35 cm^{-1}, respectively.[37] The removal of an electron from the highest occupied molecular orbital (i.e., $2\pi_g$) results in the formation of the linear $CS_2^+(\tilde{X}\,^2\Pi_{3/2,1/2})$ ground state with the spin-orbit splitting constant known to be A = -440 cm^{-1}.[30] The first excited vibrational levels for the symmetric stretch (ν_1^+), degenerate bend (ν_2^+), and asymmetric stretch (ν_3^+) for the CS_2^+ ground state are also known to be ≈ 620, 332 and 1195 cm^{-1}, respectively.[30,38]

The vibronic structures of $CS_2^+(\tilde{X}\,^2\Pi_{3/2,1/2})$ are of spectroscopic and theoretical interest.[37] The symmetry forbidden excitation of one quantum of ν_2^+ was observed in previous photoelectron spectroscopy studies,[30-33] an observation attributing to the interaction with an autoionization state. Since one quantum of ν_1^+ is approximately equal to two quanta of ν_2^+ in CS_2^+, substantial anharmonic coupling effects are expected.[39,40] As a result of the Renner-Teller effect and spin-orbit interaction, the ν_2^+ vibrational levels are expected to be split into two or more components.[38,41] Extensive information about the vibronic structures of $CS_2^+(\tilde{X}\,^2\Pi_{3/2,1/2})$ arising from Renner-Teller effect and Fermi resonances have been obtained in previous gas phase emission[42,43] and matrix isolation[44,45] studies. Due to the anharmonic coupling effects, unambiguous assignments of vibronic states to harmonic quantum numbers

are not possible.[38] The recent non-resonant two photon PFI-PE (N2P-PFI-PE) spectrum obtained by Fischer *et al.*,[30] in addition to providing accurate IEs, has yielded partially resolved Renner-Teller structures for excitation to the $(0,\nu_2^+,0)$ levels of $CS_2^+(^2\Pi_{3/2,1/2})$. Since the N2P process requires considerable laser fluences, the occurrence of dissociation and multi-photon ionization processes can cause complications in the N2P-PFI study. For example, significant fragmentation of CS_2^+ due to the absorption of additional photons has prevented the PIE measurement for CS_2^+.

It is well known that the intensity and shape of a TPE band can be affected by autoionizing states which fall within the electron energy bandwidth used in the experimental study.[1,19] We expect that optical allowed low-*n* Rydberg states close to an ionization threshold also have a similar effect on a PFI-PE band.[10] This effect has not been examined in detail previously. A major goal of this study is to compare the Franck-Condon factors of vibronic bands observed in the VUV TPE and VUV-PFI-PE spectra of CS_2.

The rotational constants of $\approx$0.109 cm^{-1} for CS_2/CS_2^+ are too small for the present experiment to resolve the rotational structures associated with the $CS_2^+(\tilde{X}\,^2\Pi_{3/2,1/2})$ photoelectron bands. We have performed a theoretical simulation of the observed VUV-PFI-PE profiles for the $CS_2^+(\tilde{X}\,^2\Pi_{3/2,1/2};\ 0_0^0)$ vibronic bands using a method which has been successfully applied to simulating the VUV-PFI-PE spectra of CO_2.[46]

II. EXPERIMENT

A. VUV laser photoionization and PFI-PE measurements

The schematic diagram of the experimental setup is shown in Fig. 1. The experimental apparatus essentially consists of a tunable VUV laser source and a photoelectron-photoion apparatus[47,48] for ion TOF and PFI-PE measurements. The experimental arrangement is similar to that used in our recent N2P-PFI studies,[47,48] except that the ionization UV laser is replaced by a VUV laser system in this study.

The VUV laser system is comprised of one excimer laser (Lambda Physik EMG201), two dye lasers (Lambda Physik FL3002) and a Hg oven. The XeCl (308 nm) output (200-250 mJ) of the excimer laser was split to pump the two dye lasers (Dye Lasers 1 and 2). The output frequencies ω_1 and ω_2 of Dye Lasers 1 and 2, respectively, were mixed in the Hg oven using a proper mixture of Hg and Ar as the nonlinear mixing medium. In this experiment, the VUV frequencies used corresponded to the sum frequencies (SF) $2\omega_1 + \omega_2$.

The design of the Hg oven is similar to that described previously.[15] The oven is constructed of a heated stainless steel tube (diameter = 3.76 cm) as the main cell with two water-cooled stainless steel side arms. The oven temperature was monitored by a thermal couple. The vapor pressure of Hg in the oven was controlled by the oven temperature, which was in turn stabilized at 400 K using a temperature feedback circuit to regulate the electric power of the oven heater. The laser entrance and exit windows were made of quartz and MgF_2, respectively. A series of baffles with appropriate apertures was installed in the side arms to prevent diffusion of Hg vapor to the entrance and exit windows. Provision was made so that Hg, which condensed at the side arms and the apertures, returned to the Hg cell. In this

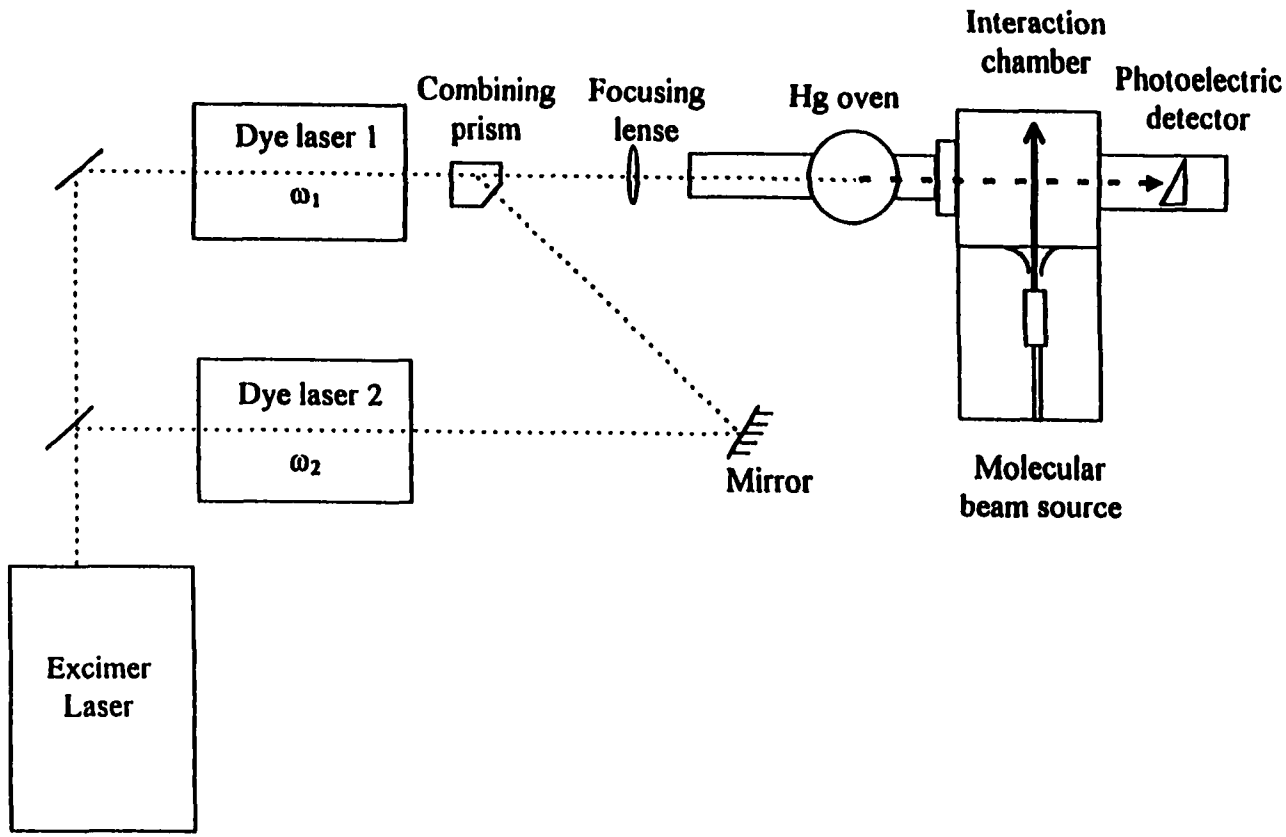

FIG. 1. Schematic diagram for the experimental setup. Rhodamine 640 was used for Dye Laser 1 and was fixed at 15 982.1 cm^{-1}. The latter frequency was doubled to ω_1 = 31 964.2 cm^{-1} using a BBOI crystal. Coumarin 540A was used for Dye Laser 2 and was tuned in the range of ω_2 = 16 949-18 868 cm^{-1}. The sum frequencies $2\omega_1 + \omega_2$ cover the range of 81 100-82 100 cm^{-1}.

experiment, Ar was introduced to the cell as the buffer gas through the inlets close to the exit window.

Rhodamine 640 dye was used for Dye Laser 1 and its output was locked at 15 982.1 cm^{-1} (625.70 nm). This fundamental frequency was doubled using a BBO1 crystal to generate the UV frequency of ω_1 = 31 964.12 cm^{-1}. We note that the N2P transition frequency of Hg from the 6^1S_0 ground state to the excited 7^1S_0 state is $2\omega_1$ = 63 928.24 cm^{-1}. For Dye Laser 2, Coumarin 540A was used to produce tunable frequencies in the visible range of ω_2 = 16 949-18 868 cm^{-1} (530-590 nm). The dye laser beams with frequencies ω_1 and ω_2 were merged in a laser-beam-combining prism (Karl Lambreht) and were further focused into the Hg oven using a lens with a focal length of 20 cm. The distance between the point of SF generation to the photoionization/photoexcitation (PI/PEX) region is 21 cm.

To calibrate the laser frequencies, a small fraction of the dye laser (ω_2) output was directed into a uranium hollow cathode tube with Ne as the buffer gas. The Ne absorption spectrum recorded simultaneously during the experiment provided accurate calibration of the CS_2 PIE and PFI-PE spectra. The bandwidth of the dye lasers is 0.2 cm^{-1} for the fundamental and ≈0.4 cm^{-1} for the second harmonic outputs. For a two-photon excitation, the resolution is ≈0.8 cm^{-1}. Thus, the resolution for the VUV laser radiation generated by SF mixing is estimated to be ≤1 cm^{-1}. The accuracy of photon frequencies given here is expected to be ±0.2 cm^{-1}.

A photoelectric detector made out of copper was used to measure the VUV laser photon intensities. The detector was situated ≈15 cm from the PI/PEX region. In addition to

monitoring the VUV light intensities, the photoelectric detector also served as a light trap for ω_1, ω_2 and VUV radiations. Since no dispersive device, such as a monochromator, was used in this experiment, the contributions to the observed photoelectric current due to ω_1, ω_2 and VUV frequencies produced by tripling and difference frequency generation (i.e., $3\omega_2$ and $2\omega_1 - \omega_2$, respectively) must be corrected. We found that the UV (ω_1) and visible (ω_2) laser beams produced negligible photoelectric signals when the oven is at room temperature. The UV and visible laser beams start to diverge from the tightly focused spot in the center of the Hg oven. We estimate that the UV and visible laser beams have a diameter of $\approx$3 mm at the PI/PEX region. The observed photoelectric signal has a minor contribution from VUV radiation resulting from tripling and difference frequency mixing. The conversion efficiency for frequency tripling is three orders of magnitude smaller than that for SF generation. The photoelectric contribution due to $3\omega_2$ is insignificant and can be measured by blocking ω_1. The sensitivities of the photoelectric detection for $3\omega_2$ and $2\omega_1 - \omega_2$ should be significantly lower than that for SF $2\omega_1 + \omega_2$ in this experiment. We found that the photoelectric spectrum recorded here is similar to the VUV spectrum in the same wavelength region obtained previously by SF generation in Hg under essentially the same experimental conditions. This observation suggests that the photoelectric signal due to difference frequency mixing is not significant.

During the alignment of the lasers beams, the photoelectric detector was retracted so that the beam spots for the UV and visible (i.e., ω_1 and ω_2, respectively) beams could be monitored outside of the vacuum chamber. Since the diameter of the VUV laser beam

produced by SF generation is smaller than the UV and visible beams, due to the negative dispersion condition, the alignment of the UV and visible beams at the PI/PEX region also ensures the alignment of the VUV beam.

The photoelectron-photoion apparatus used in this study has been described in detail.[47,48] It is modified from the laser ionization TOF mass spectrometer used in previous photodissociation studies.[49,50] A photoelectron detector, which consists of a set of simple aperture lenses and a two-stage microchannel plate detector, has been added below the photoionization region and opposite the ion TOF tube.

In this experiment, the CS_2 molecular beam was produced by seeding the CS_2 vapor (≈270 Torr) at ≈18 °C in 1714 Torr of Ar and then expanding the mixture through the nozzle (diameter = 50 μm) of a pulsed valve operating at a repetition rate of 10 Hz. The CS_2 sample was analytical grade obtained from Aldrich and was used without further purification. The Ar used was from Air Product and has a purity of ≥99.995%. The molecular beam is skimmed by a conical skimmer (1-mm diameter, 3.8 cm from the nozzle) before intersecting with a tunable VUV laser beam (90°, 8.3 cm downstream from the skimmer).

The molecular beam source chamber was pumped by a freon-trapped, 6 in. diffusion pump (pumping speed ≈2,000 L/s), while the photoionization chamber and the ion-TOF tube were evacuated by turbomolecular pumps with pumping speeds of 250 and 50 L/s, respectively. During the experiment, the beam source chamber and the photoionization chamber were maintained at pressures of $\approx 5 \times 10^{-5}$ and $\approx 5 \times 10^{-7}$ Torr, respectively.

Ion detection using the ion TOF mass spectrometer has been described previously.[47-50] In this study, a constant electric field in the range of 23-787 V/cm was used to extract the ions formed in the PI/PEX region. Using a dc ion extraction electric field at <23 V/cm was found to cause a significant loss in the ion detection sensitivity.

The PFI-PE detection scheme relies on delayed PFI of long-lived high-*n* Rydberg states populated by laser excitation at a few wavenumbers below the ionization threshold. In this experiment, the firing of the excitation laser was delayed by 520 μs with respect to the triggering pulse for opening the pulsed valve. The PFI-PE detection scheme proposed by Chupka[34] was used in the present study. A reverse-biased dc field of 0.08 V/cm was used to sweep away any prompt electrons from reaching the electron detector. After a typical delay of 3.8 μs with respect to the firing of the VUV laser, a forward-biased pulsed (duration = 1 μs) electric field of 0.24 V/cm was used to field-ionize the high-*n* Rydberg species as well as to extract the electrons to the microchannel plate detector. Using this PFI-PE detection scheme, we expect to achieve a resolution of ≈0.8 cm^{-1}.[34,46]

Since the UV and visible lasers were not focused at the PI/PEX region, multi-photon ionization processes were not favorable. Furthermore, the photon energy range (≥10.03 eV) of interest in this study is significantly higher than $3\omega_2$ and $2\omega_1 - \omega_2$. Thus the photoion and PFI-PE signals resulting from the ionization of CS_2 should be free from ion and electron backgrounds due to VUV radiation produced by tripling and difference frequency mixing. This was confirmed by the finding that negligible ion signals were observed when the heater for the Hg oven was off, or when one of the laser beams was blocked.

The firing sequence of the pulsed valve, dye laser and pulsed electric field is controlled by two digital delay units (Stanford Research DG535). The signals from the electron detector (or ion detector) and the photoelectric VUV detector were fed into two identical boxcar integrators (Stanford Research SR250), which were interfaced to an IBM/PC computer. The electron (or ion) and VUV laser signals were averaged for 10 to 30 shots at each VUV laser frequency. The spectra shown here represent the averages of 4-5 independent scans obtained at the same experimental conditions.

B. VUV synchrotron photoionization and TPE measurements

The experimental arrangement and procedures used for PIE measurements have been described previously in detail.[10] The photoionization-photoelectron apparatus (end station 2) associated with the chemical dynamics beamline[9,10] at the ALS was used.

Since the combined performance of the U10 undulator, the 6.65 m off-plane Eagle monochromator and the associated deflecting and focusing optics will be presented in a separate article,[11] only a brief description of their functions will be described below. The undulator radiation was deflected first by a water-cooled spherical mirror. A second retractable toroidal mirror directed the beam into the harmonic suppressor,[51] which was essentially a differentially pumped rare gas cell designed to absorb unwanted higher harmonics emitted from the U10. Using Ar as the filter gas, the harmonics at energies greater than 15.76 eV were essentially eliminated. That is, the synchrotron photoionization experiments of CS_2 described here are free from effects of higher order VUV radiation. After passing through the harmonic suppressor, the fundamental VUV beam was deflected and focused by a bendable cylindrical mirror (M4) followed by a second cylindrical mirror focusing onto the entrance slit of the 6.65 m off-plane

Eagle mounted monochromator. To operate in the energy range of 6-24 eV, the grating of the monochromator was required to rotate and translate. In order to maintain the horizontal focus of the VUV beam at the exit slit of the monochromator, the focal length of M4 was adjusted. The dispersed VUV light from the exit slit of the monochromator was further focused by a toroidal mirror into the photoionization region of the quadruple mass spectrometer (QMS) (or the TPE spectrometer) of End Station 2 during the PIE (or TPE) measurements. The focused VUV photon spot in the PI region was <1 mm^2. During the experiment, the peak of the U10 undulator fundamental radiation was tuned within 0.2 eV of the photon energies of interest. The photon energies were further selected by scanning the monochromator around the peak of the undulator fundamental radiation.

Due to the high brightness of the undulator synchrotron beam at the ALS, there was little obstruction of the VUV beam when a 25-μm entrance slit was used. The grating employed in this study was a MgF_2 coated 1200 l/mm grating with a dispersion of 1.24 Å/mm. We have recorded the PIE spectrum of NO using entrance and exit slits of 10 μm, corresponding to a nominal wavelength resolution of $\Delta\lambda$ = 0.0124 Å ($\Delta E \approx 0.09$ meV). The width (ΔE = 0.2 meV FWHM) observed for the autoionization features of NO at $\lambda \approx 1325$ Å (or $E \approx 9.357$ eV) indicated that the actual resolution achieved was $\Delta E/E \approx 47\,000$, more than a factor of two poorer than the nominal resolution. The PIE spectra reported here were obtained using entrance and exit slits of 15-μm, corresponding to an actual resolution of 0.3 meV (FWHM). The TPE measurements were made using 50 μm entrance and exit slits and were expected to achieve a resolution of 1.0 meV (FWHM).

The pure CS_2 beam was formed by supersonic expansion using a stainless steel nozzle at a stagnation pressure of ≈300 Torr and by a double-differentially pumped beam production system. A circular skimmer of 1-mm diameter was used between the first and second differentially pumped chambers. The first and second differentially pumping chambers, evacuated by turbomolecular pumps (Seiko Seiki) with pumping speeds of 2000 and 1200 L/s, maintained pressures of $\approx 6 \times 10^{-4}$ and 9×10^{-6} Torr, respectively, during the experiment.

For PIE measurements, the CS_2 beam thus formed entered the QMS spectrometer through a 3-mm diameter aperture along the central axis of the ion optics of the QMS. The QMS detector was divided into two differentially pumped chambers which were separated by a 6.35-mm aperture. The VUV photon beam and the CS_2 beam intersected at 90° in the photoionization region located in the first differential pumping chamber of the QMS spectrometer. After passing through the photoionization region, the VUV beam was intercepted by a silicon photodiode, from which the photon flux was measured. During the experiment, the chamber wall separating the first and second differential pumping chambers was kept at ≈77 K by filling liquid nitrogen in the jacket of the chamber wall. The first and second chambers of the QMS were evacuated by turbomolecular pumps (Seiko Seiki) with pumping speeds of 400 and 1000 L/s that maintain pressures of $\approx 5 \times 10^{-6}$ and 1×10^{-7} Torr, respectively.

The TPE spectrometer used here was a simple steradiancy analyzer.[52] The photoionization region of the TPE spectrometer was located in the main chamber of the photoionization-photoelectron apparatus and was separated from the photoionization region of the QMS spectrometer by 12.75 cm. The central axis of steradiancy ZEKE analyzer was perpendicular to the VUV photon beam, the CS_2 molecular beam and the central axis of the

QMS. The lower part of the steradiancy analyzer was situated in the photoelectron chamber, which was evacuated separately by a turbomolecular pump (Seiko Seiki) with a pumping speed of 400 L/s and maintained a pressure of $\approx 1 \times 10^{-7}$ Torr during the experiment. In the present study, the entrance and exit apertures of the steradiancy analyzer used have a diameter of 3 mm. A repeller field of ≈0.1 V/cm was used at the PI region to collect the TPEs toward the steradiancy analyzer. A set of dual-channel plate located at the end of the steradiancy analyzer was used as the electron detector.

The photon energy steps used here varied in the range of 0.1-0.5 meV and the CS_2^+ ion and TPE counting times at each step varied from 1 to 4 s. The ion and TPE intensities reported in the present study were normalized by the corresponding VUV light intensities. As indicated above, a silicon photodiode was used as the VUV detector. Since the photon energy region covered in this experiment was narrow, we expect that variation in the detection efficiency of the silicon photodiode was minor and no attempt was made to correct the VUV photon energy response of the silicon detector.

Since the energy scale for the PIE spectrum of CS_2 measured using the VUV laser is known to ±0.2 cm^{-1}, we have calibrated the energy scale of the PIE (and TPE) spectrum obtained at ALS by normalizing the positions of the autoionizing Rydberg features observed in the synchrotron experiment to those measured in the VUV laser study.

III. RESULTS AND DISCUSSION

A. Stark shift effect and Rydberg series resolved in the PIE spectrum

Figure 2(a) depicts the PIE spectrum for CS_2 in the energy region of 81 200-81 800 cm^{-1} (10.067-10.142 eV) measured using the VUV laser radiation and a dc Stark field (F) of 23 V/cm. This energy region covers the IEs for the formation of the $CS_2^+(^2\Pi_{3/2,1/2})$ spin-orbit states. The PIE spectra for CS_2 obtained using the VUV laser radiation and F = 158 and 787 V/cm near the ionization threshold are also included in the figure [see Figs. 2(b) and 2(c), respectively].

The Stark shift effect on the PIE spectrum of CS_2 can be examined at significantly lower electrostatic fields using the QMS spectrometer arrangement at ALS. The fact that the CS_2 beam is traveling along the central axis of the QMS makes possible the collection of nearly all CS_2^+ formed in the photoionization region by using a small electrostatic field. The PIE spectra for CS_2 in the region of 80 890-82 260 cm^{-1} (10.03-10.20 eV) obtained at ALS using F = 0.65, 220, 583 and 1071 V/cm are shown in Figs. 3(a)-3(d). We note that the ionization onsets for the PIE spectra of Figs. 3(a)-3(d) rise more gradually than those observed in Figs. 2(a)-2(c), suggesting that the rotational and vibrational temperatures of the CS_2 beam formed using a pulsed nozzle are lower than those produced using a cw nozzle.

The PIE spectra of Figs. 2(a)-2(c) and 3(a)-3(d) clearly show that the IE values determined using a finite repeller field (or F) at the photoionization region are lower than the "true" IE. According to the classical formula, adiabatic Stark ionization is predicted to lower the IE by $6.1(F)^{1/2}$ cm^{-1}, where F is in V/cm. We have plotted in Figs. 4(a) and 4(b) the ionization onset (or nominal IE) as a function of $F^{1/2}$ observed in the PIE spectra measured

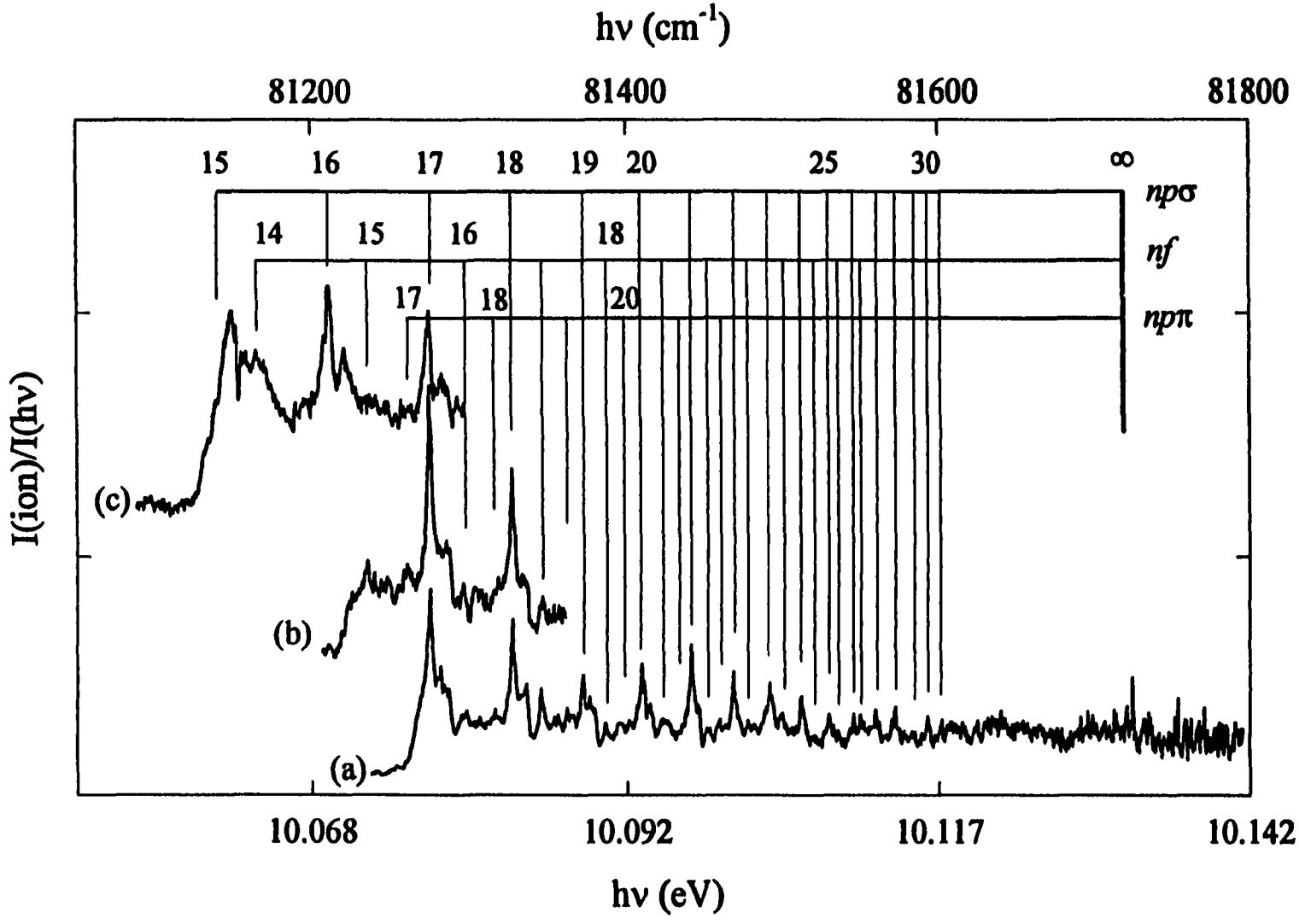

FIG. 2. PIE spectra for CS_2 in the energy range of 81 200-81 800 cm^{-1} (10.067-10.142 eV) measured using VUV laser radiation and dc Stark fields (a) F = 23 V/cm, (b) F = 158 V/cm and (c) F = 787 V/cm. Photon energy resolution is ≈1 cm^{-1} (FWHM).

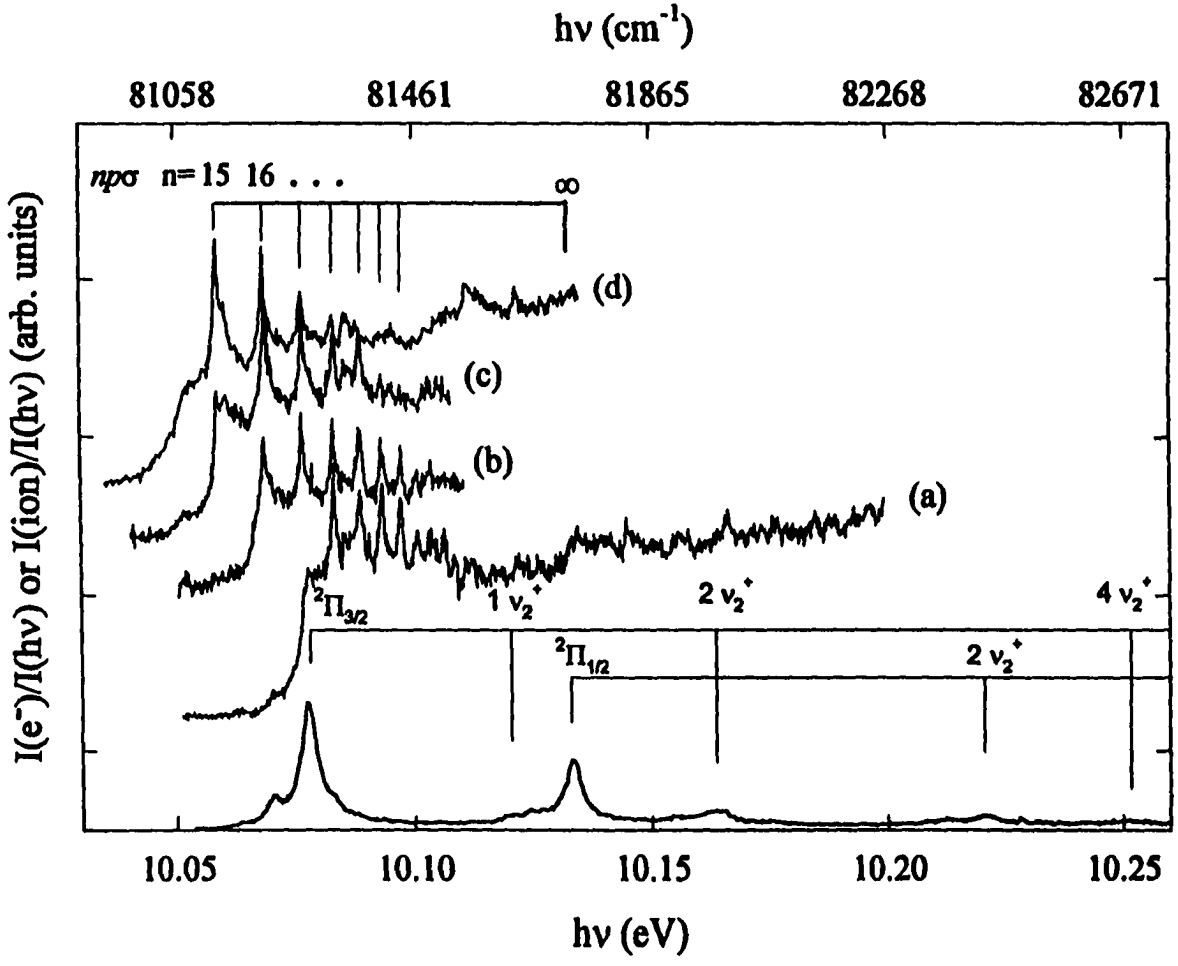

FIG. 3. PIE spectra for CS_2 in the energy range of 80 890-82 260 cm^{-1} (10.03-10.20 eV) measured using monochromatized undulator synchrotron radiation and at (a) F = 0.67 V/cm, (b) F = 220 V/cm, (c) F = 583 V/cm and (d) F = 1071 V/cm. Photon energy resolution achieved for the PIE measurements = 0.3 meV or 2.4 cm^{-1} (FWHM). The TPE spectrum for CS_2 in the energy range of 10.055-10.260 eV obtained at F = 0.1 V/cm is plotted in the bottom of the figure. Photon energy resolution achieved for the TPE measurements = 0.5 meV or 4 cm^{-1} (FWHM).

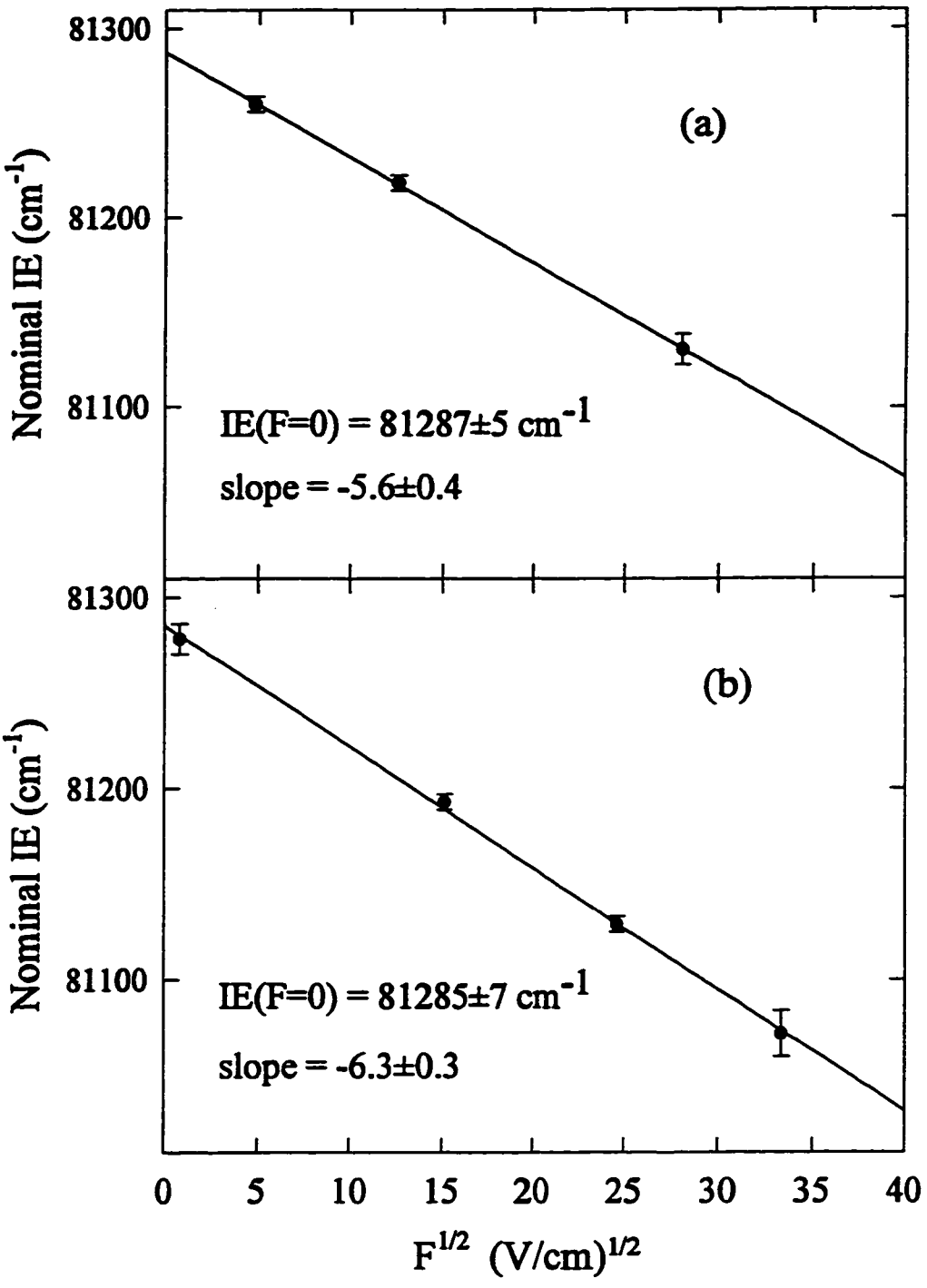

FIG. 4. Plots of nominal IE versus $F^{1/2}$ observed in the PIE spectra obtained using (a) VUV laser radiation and (b) monochromatized undulator synchrotron radiation. The linear least square fits yield slopes of -5.6 ± 0.4 and -6.3 ± 0.3 and intercepts (i.e., IE values at F = 0) of 81 287 ± 5 and 81 285 ± 7 cm^{-1} for the plots in (a) and (b), respectively.

using the VUV laser and synchrotron source, respectively. Here, the nominal IE is taken to be the mid-point of the steep rise of the photoionization onset. The uncertainties represent the photon energy spans of the steep rises. The respective slopes for the linear square fits of the plots in Fig. 4(a) and 4(b) are -5.6 ± 0.4 and -6.3 ± 0.3, in good agreement with the classically predicted value of -6.1 after taking into account the experimental uncertainties. The extrapolation of the linear plots to F = 0 V/cm in Figs 4(a) and 4(b) yields values of 81 287 ± 5 and 81 285 ± 7 cm^{-1}, respectively, for the "true" IE[$CS_2^+(\tilde{X}\,^2\Pi_{3/2})$]. These values are in excellent accord with the IE value of 81 286 ± 5 cm^{-1} obtained in the recent N2P-PFI-PE study of Fischer *et al.*[30]

In addition to having the effect of lowering the ionization onsets, a high F used also induces broadening or mixings of high-*n* Rydberg levels. Thus, the PIE spectrum measured at F = 0.67 V/cm [Fig. 3(a)] represents the least perturbed spectrum. In accord with the previous experiments,[28,29] the PIE spectrum of Fig. 3(a) exhibits a second step at 10.133 eV corresponding to the IE[$CS_2^+(^2\Pi_{1/2})$]. However, this step is not evident in the PIE spectrum [Fig. 2(a)] obtained using the VUV laser. The signal-to-noise (S/N) ratios for the PIE spectrum of Fig. 2 in the energy region of 10.129-10.142 eV are poor due to low VUV laser intensities. The fluctuation of the PIE data is partly due to the poor S/N ratios for the photoelectric signals of the VUV light detector. When the VUV signal is low and comparable to the background noise of the VUV light detector, the correction of the background of the photoelectric signal is also more difficult. The stronger autoionizing resonances observed in the spectrum of Fig. 2(a) compared to those resolved in Fig. 3(a) can be attributed to the higher resolution of the VUV laser than that of the monochromatized synchrotron radiation. Comparing the spectra of

Figs. 3(a) and 3(d), we conclude that the onset for the formation of $CS_2^+(^2\Pi_{1/2})$ is also lowered by a Stark shift comparable to that observed for the $CS_2^+(\tilde{X}\,^2\Pi_{3/2})$ onset.

Complex autoionizing structures are evident in the PIE spectrum of Fig. 2(a). The positions [$\nu(n)$ cm^{-1}] of the most prominent autoionization Rydberg series (series I) for CS_2 identified in the PIE spectrum are listed in Table I. We note that the first three members [$\nu(n)$ = 81 127.3, 81 210.4 and 81 274.8 cm^{-1}] of series I are observed in the Stark shifted PIE spectra of Figs. 2(a)-2(c) and Figs. 3(d). The positions of these states may be perturbed by the applied electric fields. The $\nu(n)$ values listed in Table I have not been corrected for the Stark shift and mixing effects. The $\nu(n)$ value at 81 127.3 cm^{-1} determined by the PIE spectrum of Fig. 3(d) is expected to be less accurate than the other $\nu(n)$ values determined by the PIE spectra measured using the VUV laser. We estimate that the uncertainties for the $\nu(n)$ values determined by the PIE spectra of Figs. 2(a)-2(c) are ±0.5 cm^{-1}. The positions of some of these Rydberg states have been observed previously in absorption[35,53] and PIE studies.[28] The $\nu(n)$ values reported previously by Ono *et al.*[28] have uncertainties of ±10 cm^{-1} and are in agreement with the results of this study after taking into account the experimental uncertainties of both experiments. We have fitted the observed $\nu(n)$ values [except $\nu(n)$ = 81 127.3 cm^{-1}] to the Rydberg formula,

$$\nu(n) = IE[CS_2^+(^2\Pi_{1/2})] - Ry/(n - \mu)^2, \qquad (1)$$

where Ry is the Rydberg constant (109 737.3153 cm^{-1}) and μ is the quantum defect. Assuming that μ is constant, we have obtained by the least square fit a value of 81 727.1 ± 0.1 cm^{-1} for the converging limit of series I (see Fig. 5). However, since the laser energy calibration is only accurate to 0.2 cm^{-1}, we have conservatively assigned uncertainties of ±0.5 cm^{-1} for the

Table I. Autoionizing Rydberg series I, II and III converging to the excited $CS_2^+(^2\Pi_{1/2})$ spin-orbit state.

n^a	$\nu(n)^b$ (cm^{-1})	$n^* (= n - \mu)^c$	μ^d
Rydberg series I $[^2\Pi_{1/2}]np\sigma_u$			
15	81 127.3[e]	13.526	1.474
16	81 210.4[e]	14.573	1.427
17	81 274.8[e]	15.576	1.424
18	81 327.5	16.572	1.428
19	81 371.7	17.572	1.428
20	81 409.0	18.574	1.426
21	81 440.7	19.574	1.426
22	81 467.8	20.572	1.428
23	81 491.3	21.573	1.427
24	81 511.8	22.576	1.424
25	81 529.5	23.566	1.434
26	81 545.3	24.569	1.431
27	81 559.1	25.558	1.442
28	81 571.9	26.591	1.409
29	81 582.5	27.548	1.452
30	81 593.0	28.606	1.394
31	81 602.0	29.617	1.383
∞	81 727.1 ± 0.5[f]		1.430[g]
Rydberg Series II $[^2\Pi_{1/2}]nf_u$			
14	81 165.0[e]	13.972	0.028
15	81 234.8[e]	14.930	0.070
16	81 296.7	15.968	0.032
17	81 345.4	16.956	0.044
18	81 386.2	17.942	0.058
19	81 421.9	18.962	0.038
20	81 450.6	19.922	0.078
21	81 477	20.947	0.053
22	81 499	21.934	0.066
23	81 519	22.964	0.036
24	81 535 ± 1	23.901	0.099
25	(81 551 ± 1)	24.963	0.037
∞	81 727.1 ± 0.5[f,h]		0.053[g]

Table I. (continued)

n[a]	$\nu(n)$[b] (cm^{-1})	n^* ($=n-\mu$)[c]	μ[d]
Rydberg series III [$^2\Pi_{1/2}$]$np\pi_u$			
17	81 264.0[e]	15.394	1.606
18	81 316.2	16.342	1.658
19	81 363.6	17.375	1.625
20	81 401.5	18.358	1.642
21	81 437.0	19.449	1.551
22	81 463.1	20.388	1.612
∞	81 727.1 ± 0.5[f]		1.616[g]

[a]Principal quantum number.

[b]Position of autoionizing Rydberg states observed in the PIE spectrum of CS_2 shown in Fig. 2. Unless specified, the uncertainties of these positions are ±0.5 cm^{-1}.

[c]Effective quantum number $n^* = n - \mu$, where μ is the quantum defect. The n^* values are calculated according to the Rydberg equation: $\nu(n) = IE[CS_2(^2\Pi_{1/2})] - Ry/(n^*)^2$, where $IE[CS_2^+(^2\Pi_{1/2})] = 81\ 727.1 \pm 0.5$ cm^{-1} is used as the converging limit and Ry = 109 737.3153 cm^{-1} is the Rydberg constant.

[d]The μ values for Rydberg series I, II and III are determined by the assignments of these series. The $IE[CS_2(^2\Pi_{1/2})] = 81\ 727.1 \pm 0.5$ cm^{-1} is used as the converging limit. See the text.

[e]The observation of these autoionizing Rydberg states are induced by the Stark shift effect. These positions have been not corrected for possible perturbation by the Stark fields.

[f]$IE[CS_2^+(^2\Pi_{1/2})] = 81\ 727.1 \pm 0.5$ cm^{-1} is determined by the least square fitting the observed $\nu(n)$, n = 16-31, values for series I to the Rydberg Eq. (1). This value is used as the converging limit for Rydberg series II and III in the calculation of n^* values.

[g]Average μ values.

[h]By fitting the ν(n) values for series II to the Rydberg formula [Eq. (1)], we obtain a value of $81\ 726.3 \pm 1.0$ cm^{-1}. See the text.

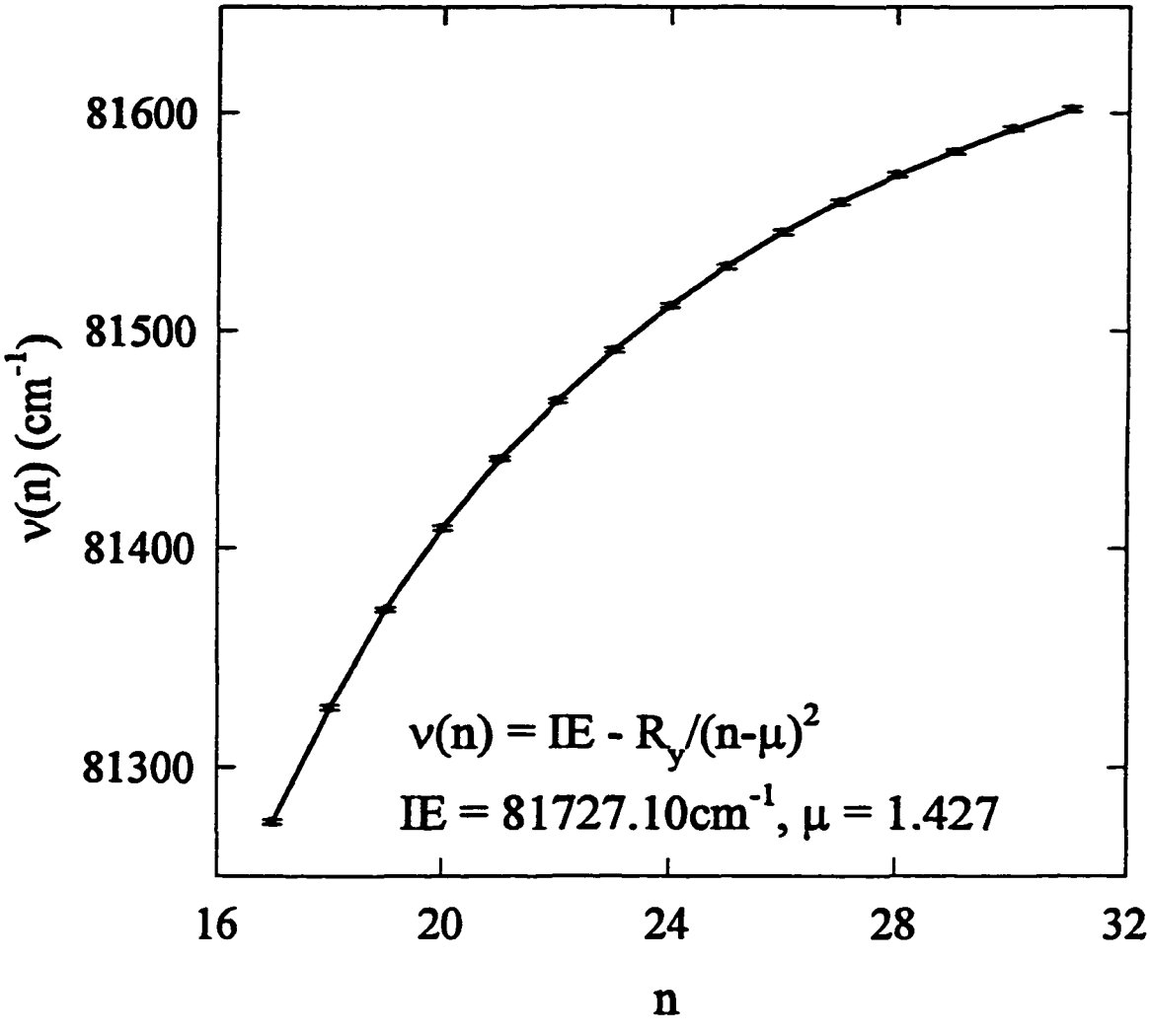

FIG. 5. Least square fit (solid line) of the experimental $\nu(n)$ values (·) to the Rydberg formula [Eq.(1)]. The best fit yields 81 727.10 ± 0.09 cm^{-1} for the converging limit and 1.427 for the average μ. Taking into account the accuracy of ±0.2 cm^{-1} for the energy calibration, we recommend IE[$CS_2^+(^2\Pi_{1/2})$] = 81 727.1 ± 0.5 cm^{-1}. See the text.

converging limit, i.e., IE[$CS_2^+(^2\Pi_{1/2})$]. The effective quantum numbers n^* ($= n - \mu$) for the corresponding $\nu(n)$ states of series I are calculated in Table I. The IE[$CS_2^+(^2\Pi_{1/2})$] value determined by the converging limit of Rydberg series I agrees with the results determined by Stark shift extrapolation given above and by the N2P-PFI-PE studies.[30] However, the accuracy for the IE value determined by the Rydberg series analysis is significantly higher than that obtained by other methods.

Based on the dipole allowed selection rule and assuming that the Rydberg states of interest here converge to the excited $CS_2^+(^2\Pi_{1/2})$ spin-orbit state, we expect that the symmetries of these Rydberg states formed by excitation from the vibrationless $CS_2(\tilde{X}\,^1\Sigma_g^+)$ ground state are derived from the $^2\Pi_g$ ion core and an *ungerade* (e.g., *p* or *f*) Rydberg electron. It is generally accepted that Rydberg series I listed in Table I are associated with the $[^2\Pi_{1/2}]np\sigma_u$ configuration.[54,55] This assignment yields an average μ of 1.427. Including the calculated μ = 1.474 for n = 15, we obtain an average μ value of 1.430 (see Table I). The latter value is in accord with the expected μ value for an *np*-Rydberg series for simple sulfur-containing molecules.[56] The irregularity in intensity observed for the autoionizing Rydberg states of series I can be attributed to perturbations due to predissociation.

In addition to Rydberg series I, many weaker autoionizing features are also resolved in the PIE spectrum of Fig. 2(a). We have been able to group some of these weaker features into Rydberg series II and III converging to IE[$CS_2^+(^2\Pi_{1/2})$]. The $\nu(n)$ values for series II and III are also listed in Table I. The observations of the first two members [$\nu(n)$ = 81 165.0 and 81 234.8 cm^{-1}] of series II and the first member [$\nu(n)$ = 81 264.0 cm^{-1}] of series III are induced by the

Stark field. Unless specified, the uncertainties of these values are ±0.5 cm^{-1}. The n^* values for series I and II are calculated according Eq. (1) with IE[$CS_2^+(^2\Pi_{1/2})$] = 81 727.1 cm^{-1}. On the basis of this analysis, we have associated Rydberg series II with the $[^2\Pi_{1/2}]nf_u$ configuration having an average μ = 0.053. When $\nu(n)$ values for series II are fitted to Eq. (1), the least square fit yields a converging limit of 81 726.3 ± 0.5 cm^{-1}. Taking into account the accuracy of ±0.2 cm^{-1} for laser frequency calibration, we have assigned uncertainties of ±1.0 cm^{-1} for the latter converging limit. That is, an independent fit of series II to the Rydberg formula leads to IE[$CS_2^+(^2\Pi_{1/2})$] = 81 726.3 ± 1.0 cm^{-1}. The latter value is consistent with, but less accurate than the value of 81 727.1 ± 0.5 cm^{-1} determined using series I. In the recent resonance enhanced multi-photon ionization (REMPI) study of Morgan *et al.*,[57] Rydberg members, n = 4-10, belonging to the $[^2\Pi_{3/2,1/2}]nf \leftarrow \tilde{X}\,^1\Sigma_g^+$ Rydberg series have been identified. These $[^2\Pi_{3/2,1/2}]nf$ transitions have not been observed in previous absorption studies.[35,53] Similar Rydberg states have also been identified in absorption and REMPI studies of CO_2.[58] Since the average μ value of 0.053 for Rydberg series II identified here is consistent with that of 0.07 found for the $[^2\Pi_{1/2}]nf$ series observed by Morgan *et al.*,[57] we conclude that the $[^2\Pi_{1/2}]nf$, n = 4-10, Rydberg states identified in the REMPI study are lower members of Rydberg series II.

Rydberg series III has an average μ value of 1.616, characteristic of an *np*-series. The previous experimental analysis[54] indicates that the μ value for an $np\pi_u$ series is greater than that for an $np\sigma_u$ series. Thus, we have assigned Rydberg series III as a $[^2\Pi_{1/2}]np\pi_u$ series. Following this assignment, we may conclude that the autoionizing intensities for the $np\sigma_u$ states are significantly stronger than those for the $np\pi_u$ states, presumably due to different efficiencies

in predissociation. The high resolution absorption study currently in progress[61] should shed light on this interpretation.

Other minor autoionizing structures which are not members of series I, II and III are likely members of Rydberg series converging to higher vibronic states of CS_2^+. Weak autoionizing Rydberg structures are also evident at energies above IE[$CS_2^+(^2\Pi_{1/2})$]. The autoionizing features resolved in Figs. 2(a) and 3(a) indicate that predissociation becomes more important at energies above ≈10.117 eV.

B. Assignment of vibronic structures and simulation of the origin band rotational contour resolved in the VUV-PFI-PE spectrum

Figure 6 shows the VUV/PFI-PE spectrum for CS_2 in the energy region of 81 100-82 100 cm^{-1}. This energy region covers the transitions from $CS_2(\tilde{X}\,^1\Sigma_g^+; \nu_1 = 0\text{-}1, \nu_2 = 0\text{-}2, \nu_3 = 0)$ to $CS_2^+(^2\Pi_{3/2,1/2}; \nu_1^+ = 0\text{-}1, \nu_2^+ = 0\text{-}2, \nu_3^+ = 0)$. For a linear molecule, such as $CS_2^+(^2\Pi_{3/2,1/2})$, with ν_2^+ bending quanta, the vibrational angular momenta along the molecular axis can have values of $l_v\hbar$, where $l_v = \nu_2^+, \nu_2^+\text{-}2, ..., 0$ or 1. Since the electronic orbital angular momentum has a nonzero projection of $\Lambda\hbar$ along the molecular axis, the Renner-Teller coupling between Λ and l_v forms a new quantum number, $K = |\Lambda \pm l_v|$. Including coupling to the projection of the spin angular momentum on the molecular axis, Σ, the total projected angular momentum is $P = \Lambda + l_v + \Sigma$. We expect that vibronic structures involving $\nu_2^+ \geq 2$ may have complex patterns. The N2P-PFI-PE study[30] has resolved the Renner-Teller splitting for the $\Delta_{3/2}$ and $\Sigma_{1/2}^-$ components of the $(0,\nu_2^+ = 1, 0)$ state. The recent theoretical investigation[38] of

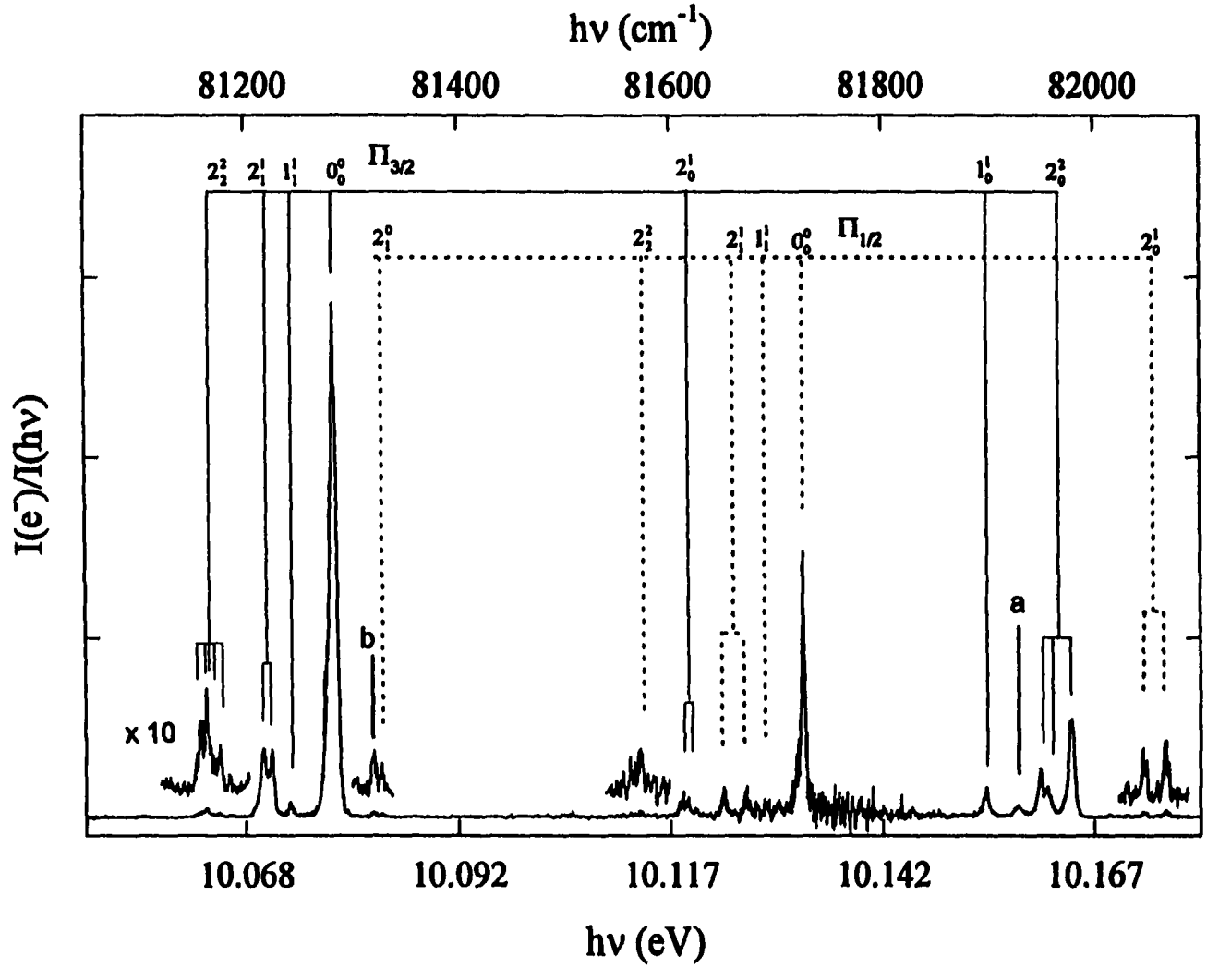

FIG. 6. VUV/PFI-PE spectrum for CS_2 in the energy region of 81 100-82 100 cm^{-1} obtained using VUV laser radiation and a pulsed field of 0.3 V/cm. See the text for the assignments of the vibronic structures. Peaks a and b marked in the figure are unassigned.

the $CS_2^+(^2\Pi_{3/2,1/2})$ Renner-Teller system has rendered insight into the characteristics of the vibronic states observed in previous experimental studies.[30,42-45] In many cases, the assignment of the vibronic structure to a "pure state" is not possible.

The positions of vibronic structures resolved in the VUV-PFI-PE and N2P-PFI-PE spectra are compared in Table II. These positions have been corrected for the Stark shifts of 1.5 cm^{-1} in the present study and 3.7 cm^{-1} in the N2P-PFI-PE experiment.[30] The predicted positions based on the theoretical calculations of Ref. 38 and the known energies for the $(\nu_1,0,0)$ and $(0,\nu_2,0)$ levels[37] are also included in the table. We have assumed that the $CS_2^+(\tilde{X}\,^2\Pi_{3/2}; 0,0,0) \leftarrow CS_2(\tilde{X}\,^1\Sigma_g^+; 0,0,0)$ transition energy is equal to 81 284.8 cm^{-1}. The comparison of the vibronic structures resolved in the spectrum of Fig. 6 and N2P-PFI-PE spectrum of Fischer *et al.* indicates that the resolution attained in the present experiment is slightly higher, allowing the identification of additional Renner-Teller structures. The slightly higher resolution achieved here is most likely due to the lower pulsed field (0.24 V/cm) used in this experiment compared to that of 1-2 V/cm used in the N2P-PFI study.[30] The assignments of the vibronic structures given in the spectrum of Fig. 6 and in Table II are mostly based on those of the N2P-PFI-PE and theoretical studies.[30,38] Nearly all the vibronic transitions identified in the N2P-PFI-PE spectrum are also found in the VUV-PFI-PE spectrum. As shown in the table, the positions of vibronic features identified in the N2P-PFI-PE spectrum differ from those found in the VUV-PFI-PE spectrum by ≤ 3 cm^{-1}.

The $\Pi_{3/2}(0_0^0)$ and $\Pi_{1/2}(0_0^0)$ bands are identified at 81 284.8 and 81 725.9 cm^{-1} with widths of 4.7 and 3.5 cm^{-1} (FWHM), respectively.[59] Thus, the VUV-PFI-PE spectrum yields

Table II. Comparison of experimental and calculated vibronic PFI-PE bands of $CS_2^+(^2\Pi_{3/2,1/2})$.

Assignment	Experimental Energy[a] (cm^{-1}) VUV/PFI-PE[b]	Experimental Energy[a] (cm^{-1}) N2P-PFI-PE[c]	Calculated Energy[d] (cm^{-1}) Ref. 38
$^2\Pi_{3/2}(\nu_1^+,\nu_2^+,\nu_3^+) \leftarrow {}^1\Sigma_g^+(\nu_1,\nu_2,\nu_3)$			
$(0,0,0,) \leftarrow (0,1,0)$	...[e]	80 888	80 886.6
$(0,2,0)^2\Pi_{1/2} \leftarrow (0,2,0)^1\Sigma_g^+$	...[f]	81 164	81 166.3 (81 148.9)[g]
$(0,2,0)^2\Pi_{1/2} \leftarrow (0,2,0)^1\Delta_g$	...[f]		81 176.3 (81 158.9)[g]
$(0,2,0)^2\Phi_{7/2} \leftarrow (0,2,0)^1\Delta_g$	...[f]		81 177.5 (81 166.8)[g]
$(0,2,0)^2\Pi_{3/2} \leftarrow (0,2,0)^1\Sigma_g^+$	...[f]		81 180.3 (81 177.8)[g]
$(0,2,0)^2\Pi_{3/2} \leftarrow (0,2,0)^1\Delta_g$	...[f]		81 190.3 (81 187.8)[g]
$(0,1,0)^2\Sigma_{1/2}^+ \leftarrow (0,1,0)$	81 217.6	81 222	81 226.4
$(0,1,0)^2\Delta_{5/2} \leftarrow (0,1,0)$	81 225.7		81 231.4
$(1,0,0) \leftarrow (1,0,0)$	81 242.6	81 244	81 220.1
$(0,0,0) \leftarrow (0,0,0)$	81 284.8	81 286	81 284.8[h]
$(0,1,0)^2\Sigma_{1/2}^+ \leftarrow (0,0,0)$	81 613.1	81 618	81 622.4
$(0,1,0)^2\Delta_{5/2} \leftarrow (0,0,0)$	81 618.1[i]		81 627.4
$(1,0,0) \leftarrow (0,0,0)$	81 901.1	81 900	81 899.8
	81 930.7[j]		
$(0,2,0)^2\Pi_{1/2} \leftarrow (0,0,0)$	81 950.9	81 950	81 968.3
$(0,2,0)^2\Phi_{7/2} \leftarrow (0,0,0)$	81 958.8[i]		81 969.5
$(0,2,0)^2\Pi_{3/2} \leftarrow (0,0,0)$	81 979.8		81 982.3

Table II. (continued)

Assignment	Experimental Energy[a] (cm^{-1}) VUV/PFI-PE[b]	N2P-PFI-PE[c]	Calculated Energy[d] (cm^{-1}) Ref. 38
$^2\Pi_{1/2}(\nu_1^+,\nu_2^+,\nu_3^+) \leftarrow {}^1\Sigma_g^+(\nu_1,\nu_2,\nu_3)$			
	81 322.4[j]		
$(0,0,0) \leftarrow (0,1,0)$	81 329.9[k]	81 328	81 329.9
$(0,2,0)^2\Phi_{5/2} \leftarrow (0,2,0)^1\Delta_g$	...[l]	81 564	81 593.7
$(0,2,0)^2\Pi_{3/2} \leftarrow (0,2,0)^1\Sigma_g^+$	...[l]		81 629.1
$(0,2,0)^2\Pi_{1/2} \leftarrow (0,2,0)^1\Sigma_g^+$	...[l]		81 633.6
$(0,2,0)^2\Pi_{3/2} \leftarrow (0,2,0)^1\Delta_g$	...[l]		81 639.1
$(0,2,0)^2\Pi_{1/2} \leftarrow (0,2,0)^1\Delta_g$	...[l]		81 643.6
$(0,1,0)^2\Delta_{3/2} \leftarrow (0,1,0)$	81 651.3	81 648	81 661.9
$(0,1,0)^2\Sigma_{1/2}^- \leftarrow (0,1,0)$	81 672.6	81 670	81 681.9
$(1,0,0) \leftarrow (1,0,0)$	(81 689)[m]	81 686	81 686.9
$(0,0,0) \leftarrow (0,0,0)$	81 725.9	81 726	81 725.9[n]
$(0,1,0)^2\Delta_{3/2} \leftarrow (0,0,0)$	82 047.2[f]	82 046	82 057.9
$(0,1,0)^2\Sigma_{1/2}^- \leftarrow (0,0,0)$	82 068.3	82 068	82 077.9

[a]Values have been corrected for the Stark shifts of 1.5 cm^{-1} and 3.7 cm^{-1} for the VUV-PFI-PE (this work) and N2P-PFI-PE studies (Ref. 30).

[b]This work.

[c]Reference 30.

[d]The calculations use the known transition energies: (ν_1 = 1,0,0) (658.0 cm^{-1}), (0,ν_2 = 1,0) (396.0 cm^{-1}), (0,ν_2 = 2,0) $^1\Delta_g$ (792 cm^{-1}) and (0,ν_2 = 2,0) $^1\Sigma_g^+$ (802 cm^{-1}) of Ref. 36 and the vibronic energies for $CS_2^+(\tilde{X}\,^2\Pi_{3/2,1/2};\nu_1^+,\nu_2^+)$ given in Ref. 38.

[e]Not covered in the energy range of the present study.

Table II. (continued)

[f]Multiple peaks are resolved in the predicted energy range for these transitions. See Fig. 8 for comparison between predicted positions and experimental structures.

[g]Values calculated using the vibronic level energies for $CS_2(^1\Sigma_g^+; 0,2,0)$ [see footnote (d)] and $CS_2^+(^2\Pi_{3/2}; 0,2,0)$. From the analysis of the $^2\Pi_{3/2}(2_0^2)$ vibronic band, we obtained the Renner-Teller level energies of 666, 674 and 695 cm^{-1} for (0,2,0) $^2\Pi_{1/2}$, (0,2,0) $^2\Phi_{7/2}$ and (0,2,0)$^2\Pi_{3/2}$, respectively, for $CS_2^+(^2\Pi_{3/2}; 0,2,0)$ [measured with respect to $CS_2^+(^2\Pi_{3/2}; 0,0,0)$].

[h]$IE[CS_2^+(^2\Pi_{3/2})]$ determined by the VUV-PFI-PE spectrum.

[i]The assignments of 81 618.1 and 81 958.8 cm^{-1} to the transitions (0,1,0) $^2\Delta_{5/2} \leftarrow$ (0,0,0) and (0,2,0) $^2\Phi_{7/2} \leftarrow$ (0,0,0) are questionable because these transitions are highly forbidden.

[j]Unassigned.

[k]Tentative assignment.

[l]The peak maximum of the experimental feature is at 81 574.5 cm^{-1}. The detailed Renner-Teller components cannot be identified due to poor S/N ratios.

[m]Estimated value.

[n]$IE[CS_2^+(^2\Pi_{1/2})]$ determined by the VUV-PFI-PE spectrum.

IE[$CS_2^+(\tilde{X}\,^2\Pi_{3/2})$] = 81284.8 ± 4.7 cm^{-1} (10.0780 ± 0.0006 eV) and IE[$CS_2^+(^2\Pi_{1/2})$] = 81 725.9 ± 3.5 cm^{-1} (10.1327 ± 0.0004 eV), in excellent agreement with the values determined by the N2P-PFI-PE, the Rydberg series and the Stark shift extrapolation methods. The difference between the $^2\Pi_{3/2}(0_0^0)$ and $^2\Pi_{1/2}(0_0^0)$ bands observed here gives a value for A = -441.1 ± 0.5 cm^{-1}, again in agreement with the literature value of -440 cm^{-1}.[30,38,41]

We have compared the structures of the $\Pi_{3/2}(0_0^0)$ and $\Pi_{1/2}(0_0^0)$ bands in Fig. 7(a). The branching ratio for the production of $CS_2^+(\tilde{X}\,^2\Pi_{3/2})$ to that of $CS_2^+(^2\Pi_{1/2})$ is estimated to be 1.9 based on the measured ratio for the intensities of the $^2\Pi_{3/2}(0_0^0)$ and $^2\Pi_{1/2}(0_0^0)$ bands. The main difficulty in the determination of the relative intensities for the $^2\Pi_{3/2}(0_0^0)$ and $^2\Pi_{1/2}(0_0^0)$ bands is the low VUV light intensities at the energy range of the $^2\Pi_{1/2}(0_0^0)$ bands, thus making it difficult to make the background correction for the photoelectric detector. We estimate the uncertainties for the ratio of the intensities to be ±0.3, i.e., the branching ratio for $CS_2^+(^2\Pi_{3/2})/CS_2^+(^2\Pi_{1/2})$ = 1.9 ± 0.3.

A simulation of the $^2\Pi_{3/2}(0_0^0)$ and $^2\Pi_{1/2}(0_0^0)$ band profiles has been made by calculating the absorption spectrum of CS_2 near the $CS_2^+(\tilde{X}\,^2\Pi_{3/2,1/2})$ thresholds corresponding to a superposition of $p + f$ complexes for a very large value of n. This method has been used with success for simulating the PFI-PE of CO_2.[46] The values for the transition moments to the p and f states are taken from *ab initio* calculations,[60] which have been slightly corrected to agree with the absorption spectrum of the first np and nf complexes.[61] The respective transition moments of the $p\pi^1\Sigma$, $p\sigma^1\Pi$, $f\pi^1\Sigma$, $f\sigma^1\Pi$ and $f\delta^1\Pi$ states are 3.0, 1.0, 2.32, 2.82 and 1.43. The mean IE has been fixed at 81 506 cm^{-1}, while the known A = -440 cm^{-1} is used. The rotational

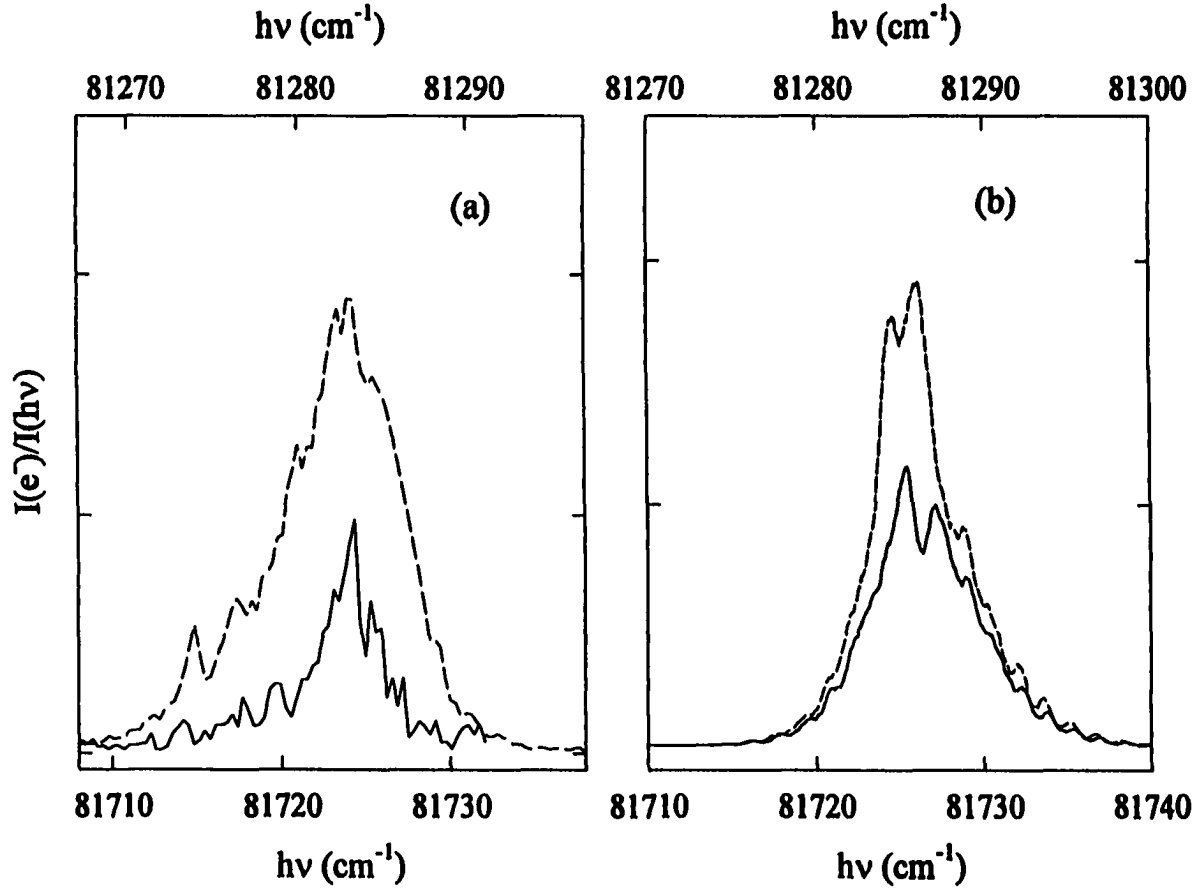

FIG. 7. (a) Comparison of the 0_0^0 bands for $CS_2^+(^2\Pi_{3/2})$ (---) and $CS_2^+(^2\Pi_{1/2})$ (solid line) observed in the VUV-PFI-PE spectra obtained using VUV laser radiation and a pulsed field of 0.3 V/cm. The ratio of the peak intensities yield a branching ratio of 1.9 ± 0.3 for the production of $CS_2^+(^2\Pi_{3/2})$ and $CS_2^+(^2\Pi_{1/2})$. (b) Simulated profiles for the $^2\Pi_{3/2}(0_0^0)$ (---) and $^2\Pi_{1/2}(0_0^0)$ (solid line) bands. Rotational temperature = 10 K. The linewidth used in the simulation is similar to the experimental width of ≈1 cm^{-1}. The upper and lower energy scales apply to the $^2\Pi_{3/2}(0_0^0)$ and $^2\Pi_{1/2}(0_0^0)$ bands, respectively. See the text.

constants[60] used for $CS_2(\tilde{X}\,^1\Sigma_g^+)$ and $CS_2^+(\tilde{X}\,^2\Pi_{3/2,1/2})$ are 0.109126 and 0.10914 cm^{-1}, respectively. The calculation also assumes a rotational temperature of 10 K for $CS_2(\tilde{X}\,^1\Sigma_g^+)$.

Without considering the lifetimes of the Rydberg states, the calculated $^2\Pi_{3/2}(0_0^0)$ and $^2\Pi_{1/2}(0_0^0)$ bands for n = 2000 have equal areas or equal intensities as observed in the HeI photoelectron spectrum for CS_2.[31] Each of these band profiles consists of two peaks; one on the left and one on the right which correspond to the negative and positive branches of $\Delta J = J^+ - J''$, respectively, where J^+ and J'' are the total angular momentum for CS_2^+ and CS_2. In order to explain the observed branching ratio of 1.9 ± 0.3 for $CS_2^+(^2\Pi_{3/2})/CS_2^+(^2\Pi_{1/2})$, it is necessary to take into account the decay by spin-orbit and rotational autoionization of the rotational levels using the method described in Ref. 62 and the fitted μ values obtained in Ref. 60. The decay of the $^2\Pi_{1/2}$ part is stronger than the $^2\Pi_{3/2}$ part due to the larger number of open decay channels. If a value of n = 270 corresponding to the Stark shift level, is used, after a delay of 3.8 μs, the $^2\Pi_{1/2}$ peak is predicted to disappear completely. It is well-known that the l-mixing due to the Stark effect introduces a lengthening of the lifetimes.[34] Here l is the orbital angular momentum of the Rydberg electron. Assuming as in Ref. 62 that this lengthening is the same for each rotational level and each l-complex, a qualitative agreement with the experimental branching ratio is obtained by multiplying n a scaling factor of 6 [see Fig. 7(b)]. This corresponds to a "dilution" factor of 220, close to the n value, namely to a decay rate in n^{-4} instead of n^{-3} as expected. The $^2\Pi_{3/2}$ band is dominated by the p contribution because the decay by rotational autoionization is not very important. For the $^2\Pi_{1/2}$ band, the decay of the p contribution by both the spin-orbit and the rotational autoionization is more important than the decay of the f

contribution. This is due to the fact that the decay is proportional to the difference between the μ values of the singlet and triplet states, which is larger for the *p* states than for the *f* states. Consequently, it is the *f* contribution which dominates the $^2\Pi_{1/2}$ band.

The assignments of vibronic transitions involving the $CS_2^+(\tilde{X}\,^2\Pi_{3/2})$ state are given in the first half of Table II. The hot band 2_1^0, identified at 80 888 cm^{-1} in the N2P-PFI-PE spectrum, is not covered in the energy range of the present experiment. The peak at 81 901.1 cm^{-1} is 616.3 cm^{-1} above the $^2\Pi_{3/2}(0_0^0)$ band and is identified as $^2\Pi_{3/2}(1_0^1)$. This assignment is consistent with the previous N2P-PFI-PE and theoretical prediction of 81 899.8 cm^{-1} for the $^2\Pi_{3/2}(1_0^1)$ band. The 81 242.6 cm^{-1} peak which is 658.5 cm^{-1} below the $^2\Pi_{3/2}(1_1^1)$ band is thus assigned to $^2\Pi_{3/2}(1_0^1)$. The $^2\Pi_{3/2}(2_0^1)$ band is predicted to be a doublet at 81 622.4 and 81 627.4 cm^{-1}, corresponding to the transitions $(0,1,0)^2\Sigma_{1/2}^+ \leftarrow (0,0,0)$ and $(0,1,0)^2\Delta_{5/2} \leftarrow (0,0,0)$. The N2P-PFI-PE spectrum only reveals one peak at 81 618 cm^{-1}. This peak is resolved into two peaks at 81 613.6 and 81 618.1 cm^{-1} in the VUV-PFI-PE spectrum. Although these values are lower than the corresponding theoretical predictions by $\approx$9 cm^{-1}, the observed separation of 5 cm^{-1} is identical to the theoretical prediction. However, since the $(0,1,0)^2\Delta_{5/2} \leftarrow (0,0,0)$ transition is highly forbidden, the peak observed at 81 618.1 cm^{-1} may not be due to this transition. The vibronic band at 81 222 cm^{-1} observed in the N2P-PFI-PE spectrum is also resolved into a doublet at 81 217.6 and 81 225.7 cm^{-1} in the present experiment. These peaks are assigned to the transitions $(0,1,0)^2\Sigma_{1/2}^+ \leftarrow (0,1,0)$ and $(0,1,0)^2\Delta_{5/2} \leftarrow (0,1,0)$, respectively. The corresponding positions predicted for these transitions are 81 226.4 and 81 231.4 cm^{-1}. Since the S/N ratio for the 2_1^1 band is significantly better than that for the 2_0^1 band, the Renner-

Teller splitting for the (0,1,0) state of $CS_2^+(\tilde{X}\,^2\Pi_{3/2})$ is more reliably determined by the 2_1^1 band to have a value of 8 cm^{-1}. The previous N2P-PFI-PE study observed a single peak at 81 950 cm^{-1} for the 2_0^2 band. This band is predicted to be a triplet at 81 968.3, 81 969.5 and 81 982.3 cm^{-1}. We have assigned the three peaks at 81 950.9, 81 958.8 and 81 979.8 cm^{-1} resolved in the spectrum of Fig. 6 to the transitions $(0,2,0)^2\Pi_{1/2} \leftarrow (0,0,0)$, $(0,2,0)^2\Phi_{7/2} \leftarrow (0,0,0)$ and $(0,2,0)^2\Pi_{3/2} \leftarrow (0,0,0)$, respectively. The discrepancies between the experimental and theoretical values for the $(0,2,0)^2\Pi_{1/2} \leftarrow (0,0,0)$, $(0,2,0)^2\Phi_{7/2} \leftarrow (0,0,0)$ and $(0,2,0)^2\Pi_{3/2} \leftarrow (0,0,0)$ transitions are 17.4, 10.7 and 2.5 cm^{-1}, respectively. However, these differences are within the theoretical accuracy of 10-20 cm^{-1}. We caution that the association of the peak at 81 969.5 cm^{-1} to the $(0,2,0)^2\Phi_{7/2} \leftarrow (0,0,0)$ transition is subject to future verification because this transition is highly forbidden. Taking into account the anharmonicity, the (0,2,0) state of the $CS_2(\tilde{X}\,^1\Sigma_g^+)$ ground state is split into 2 levels: $^1\Delta_g$ at 792 cm^{-1} and $^1\Sigma_g^+$ at 802 cm^{-1} above the $CS_2(\tilde{X}\,^1\Sigma_g^+;\ 0,0,0)$ state.[37] Thus, the 2_2^2 band is predicted to consist of 5 transitions: $(0,2,0)^2\Pi_{1/2} \leftarrow (0,2,0)^1\Sigma_g^+$ at 81 166.3 cm^{-1}, $(0,2,0)^2\Pi_{1/2} \leftarrow (0,2,0)^1\Delta_g$ at 81 176.3 cm^{-1}, $(0,2,0)^2\Phi_{7/2} \leftarrow (0,2,0)^1\Delta_g$ at 81 177.5 cm^{-1}, $(0,2,0)^2\Pi_{3/2} \leftarrow (0,2,0)^1\Sigma_g^+$ at 81 180.3 cm^{-1} and $(0,2,0)^2\Pi_{3/2} \leftarrow (0,2,0)^1\Delta_g$ at 81 190.3 cm^{-1}. As shown in Fig. 8, the pattern of these predicted transition energies seems to lie at a slightly higher energy compared to the position of the 2_2^2 band. From the analysis of the 2_0^2, we have obtained the Renner Teller vibronic energies of 666, 674 and 695 cm^{-1} for $(0,2,0)^2\Pi_{1/2}$, $(0,2,0)^2\Phi_{7/2}$ and $(0,2,0)^2\Pi_{3/2}$, respectively, above $CS_2^+(^2\Pi_{3/2};$ 0,0,0). In accordance with these values, the transition energies are predicted as: $(0,2,0)^2\Pi_{1/2} \leftarrow$

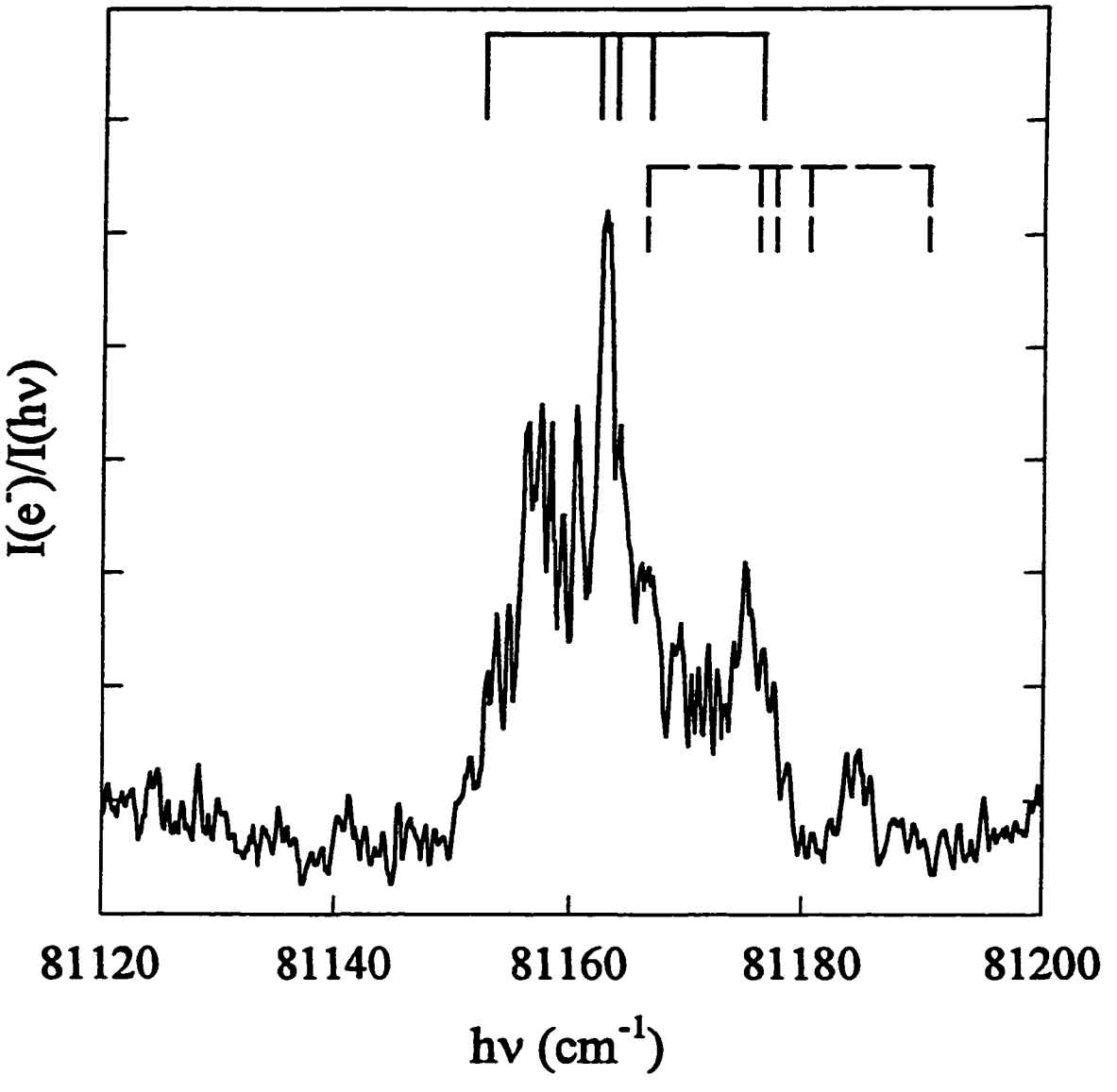

FIG. 8. Comparison of the observed structures for the $^2\Pi_{3/2}(2_2^2)$ band and the predicted transition energies. The solid vertical marks are predicted positions based on level energies from the analysis of the Renner-Teller structure of the $^2\Pi_{3/2}(2_0^2)$ band. The dashed vertical marks are energies predicted by theoretical level energies from Ref. 38. See the text. Part of the observed features should be due to rotational structures.

$(0,2,0)^1\Sigma_g^+$ at 81 148.9 cm^{-1}, $(0,2,0)^2\Pi_{1/2} \leftarrow (0,2,0)^1\Delta_g$ at 81 158.9 cm^{-1}, $(0,2,0)^2\Phi_{7/2} \leftarrow (0,2,0)^1\Delta_g$ at 81 166.8 cm^{-1}, $(0,2,0)^2\Pi_{3/2} \leftarrow (0,2,0)^1\Sigma_g^+$ at 81 177.8 cm^{-1}, and $(0,2,0)^2\Pi_{3/2} \leftarrow (0,2,0)^1\Delta_g$ at 81 187.8 cm^{-1} (see Table II). A better match between this latter set of predicted energies and experimental structures for the 2_2^2 band is observed in Fig. 8. However, the experimental peak at 81 185 cm^{-1} seems to be unaccounted for by the predicted positions. We note that the nature is not known for the band observed at 81 930.7 cm^{-1} in the VUV-PFI-PE spectrum.

Similar vibronic transitions to the excited $CS_2^+(^2\Pi_{1/2})$ spin-orbit state are identified as given in the second half of Table II. Subtracting the known level position of 396 cm^{-1} for $(0,\nu_2 = 1, 0)$ from the energy (81 725.9 cm^{-1}) for the 0_0^0 band, we obtain the energy of 81 329.9 cm^{-1} for the hot band transition $(0,0,0) \leftarrow (0,1,0)$. The previous N2P-PFI-PE study identified a band at 81 328 cm^{-1} for this transition. Two peaks at 81 322.4 and 81 329.9 cm^{-1} are found in the spectrum of Fig. 6. We tentatively assign the latter peak to be the $^2\Pi_{1/2}(2_1^0)$ band. The peak at 81 322.4 is left unassigned here. The assignments of the 2_1^1 and 2_0^1 vibronic bands are in excellent agreement with that of the N2P-PFI-PE study, yielding a Renner-Teller splitting of 21.4 cm^{-1} for the $(0,1,0)^2\Delta_{3/2}$ and $(0,1,0)^2\Sigma_{1/2}^-$ states. Although the theoretical prediction (20 cm^{-1})[38] for the splitting of the $(0,1,0)^2\Delta_{3/2}$ and $(0,1,0)^2\Sigma_{1/2}^-$ states are in agreement with the experimental observation, the absolute transition energy for $(0,1,0)^2\Delta_{3/2} \leftarrow (0,0,0)$, $(0,1,0)^2\Sigma_{1/2}^- \leftarrow (0,0,0)$, $(0,1,0)^2\Delta_{3/2} \leftarrow (0,1,0)$ and $(0,1,0)^2\Sigma_{1/2}^- \leftarrow (0,1,0)$ are higher than the corresponding experimental energies by $\approx$10 cm^{-1}. The N2P-PFI-PE study identifies the $(1,0,0) \leftarrow (1,0,0)$ transition at 81 686 cm^{-1}. Due to the poor S/N ratios in this energy region, the value of 81 689

cm^{-1} obtained here from the VUV-PFI-PE spectrum is a crude estimate. The $^2\Pi_{1/2}(2_2^2)$ vibronic band is also predicted to have 5 peaks: $(0,2,0)^2\Phi_{5/2} \leftarrow (0,2,0)^1\Delta_g$ at 81 593.7 cm^{-1}, $(0,2,0)^2\Pi_{3/2} \leftarrow (0,2,0)^1\Sigma_g^+$ at 81 629.1 cm^{-1}, $(0,2,0)^2\Pi_{1/2} \leftarrow (0,2,0)^1\Sigma_g^+$ at 81 633.6 cm^{-1}, $(0,2,0)^2\Pi_{3/2} \leftarrow (0,2,0)^1\Delta_g$ at 81 639.1 cm^{-1} and $(0,2,0)^2\Pi_{1/2} \leftarrow (0,2,0)^1\Delta_g$ at 81 643.6 cm^{-1}. These predicted transition energies are at the high energy side of the observed structure attributable to the $^2\Pi_{1/2}(2_2^2)$ band (peak maximum at 81 574.5 cm^{-1}) (see Fig. 6). The detailed Renner-Teller components for the $^2\Pi_{1/2}(2_2^2)$ band cannot be identified here because of poor S/N ratios. Nevertheless, the profiles for the $^2\Pi_{3/2}(2_2^2)$ band and $^2\Pi_{1/2}(2_2^2)$ band (peak maximum at 81 574.5 cm^{-1}) appear to be similar.

The rotational temperature for the CS_2 pulsed beam is assumed to be 10 K in this study. However, since the rotational constant for CS_2 is small, a significant number of rotational states are still populated. Observed multiple peak structures may be of vibronic as well as rotational origin. Thus the suggested assignments of Renner-Teller structures are not definitive.

C. Relative vibronic band intensities observed in the VUV-PFI-PE, N2P-PFI-PE and TPE spectra

The major difference between the N2P- and VUV-PFI-PE spectra is the relative intensities for the vibronic bands. Noticeably, the relative intensities for the vibronic bands close to the $\Pi_{1/2}(0_0^0)$ band in the energy region of 81 550-81 800 cm^{-1} observed in the VUV-PFI-PE spectrum are significantly lower than those observed in the N2P-PFI-PE spectrum. Furthermore, the doublet for the $^2\Pi_{1/2}(2_0^1)$ band resolved in VUV-PFI-PE spectrum is also weaker than that found in the N2P-PFI-PE spectrum. We note that the published N2P-PFI-PE

spectrum has not been normalized by the laser intensities. Thus, the above comparison may not be meaningful. It has been shown previously in other N2P-PFI-PE studies that the relative intensities for vibronic bands observed in the N2P-PFI-PE spectrum can be different from those in the single photon or VUV photoelectron spectrum because of the mediation of a dissociative state in the N2P study.[63,64]

The TPE spectrum for CS_2 in the energy region of 10.055-10.260 eV obtained at ALS and F = 0.1 V/cm is plotted at the bottom of Fig. 3. The electron energy resolution achieved for the TPE spectrum is 3 meV (FWHM). The TPE spectrum obtained here is in excellent agreement with that reported previously using a similar energy resolution.[32] Based on the detailed assignment of the VUV-PFI-PE spectrum above, we conclude that the first two prominent peaks of the TPE spectrum are the $\tilde{X}\,^2\Pi_{3/2}(0_0^0)$ and $^2\Pi_{1/2}(0_0^0)$ bands, marking IE[$CS_2^+(\tilde{X}\,^2\Pi_{3/2})$] and IE[$CS_2^+(^2\Pi_{1/2})$]. The other minor peaks marked in the spectrum are vibronic bands consisting of Renner-Teller structures due to excitation of 2 and 4 quanta of ν_2^+.[32] The small peak resolved in the TPE spectrum below the IE[$CS_2^+(^2\Pi_{3/2})$] is due to the hot band $^2\Pi_{3/2}(2_1^1)$. The comparison of the TPE spectrum and the PIE spectrum of Fig. 3(a) indicates that the IEs determined by step-like features in PIE measurements and peaks in TPE measurements at a low F are in excellent agreement.

We have also compared the VUV-PFI-PE and TPE spectra in Figs. 9(a) and 9(b), respectively. Although the resolution of the TPE spectrum is significantly lower than that achieved in the VUV-PFI-PE study, the agreement between the IE[$CS_2^+(\tilde{X}\,^2\Pi_{3/2,1/2})$] values determined by the peak positions of the two prominent photoelectron bands resolved in the

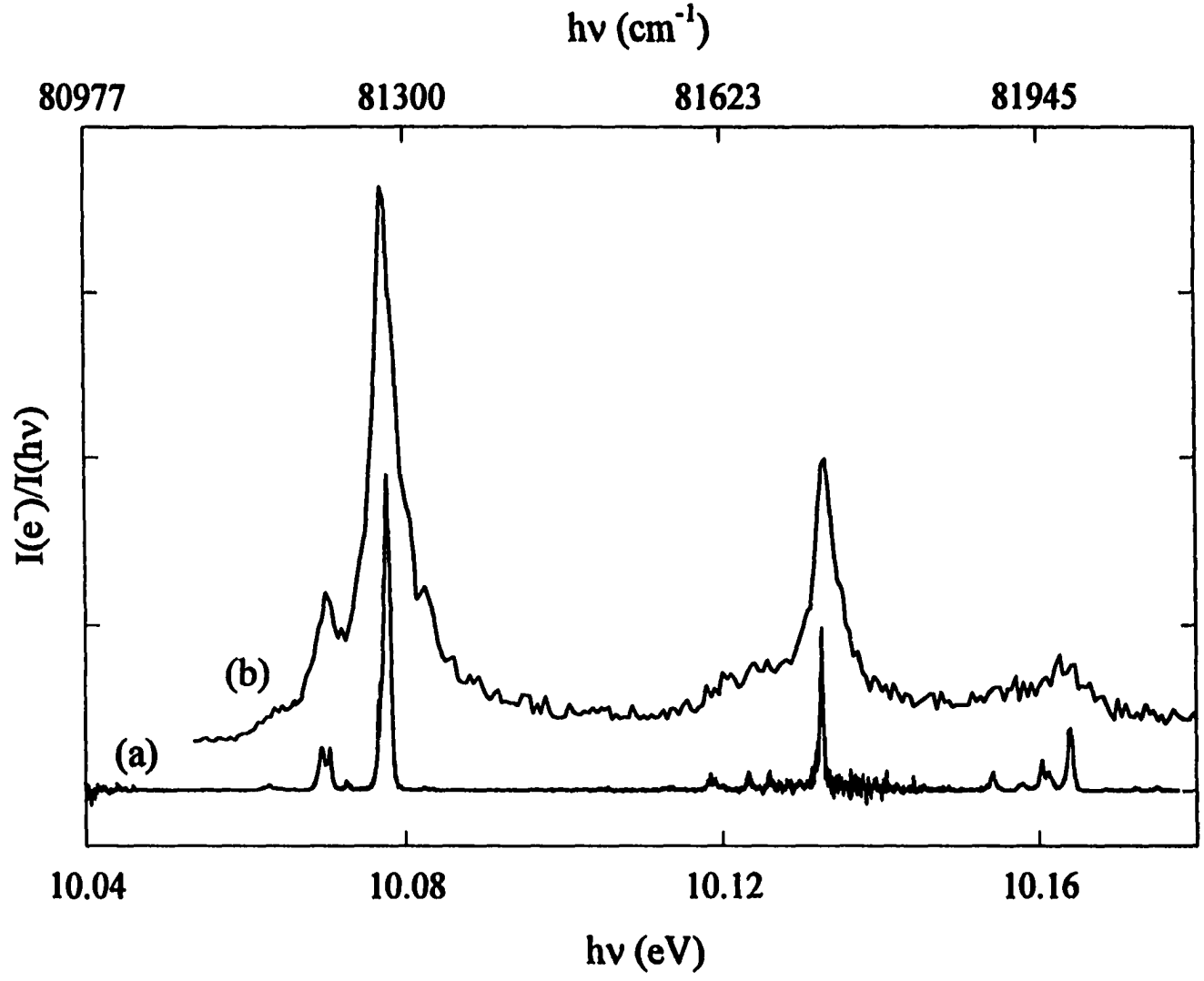

FIG. 9. Comparison of the (a) VUV-PFI-PE and (b) TPE spectra in the energy region of 81 100-82 100 cm^{-1}.

spectra of Figs. 9(a) and 9(b) is excellent. This observation indicates that using the width of a photoelectron band to set the experimental uncertainties for the IEs may be too conservative. Other weaker vibronic structures observed in the VUV-PFI-PE spectrum are also evident in the TPE spectrum.

Most interestingly, the relative intensities for the vibronic bands observed in the TPE and VUV-PFI-PE spectrum are found to be in excellent accord. While the intensities for the $^2\Pi_{3/2}(0_0^0)$ and $^2\Pi_{1/2}(0_0^0)$ photoelectron bands observed in the HeI photoelectron spectrum of CS_2 are comparable,[31] a ratio of $\approx$2 is observed for the intensity of the $^2\Pi_{3/2}(0_0^0)$ band to that of the $^2\Pi_{1/2}(0_0^0)$ band found in the VUV-PFI-PE and TPE spectra. The explanation for the relative intensities of the $^2\Pi_{3/2}(0_0^0)$ and $^2\Pi_{1/2}(0_0^0)$ bands observed in the VUV-PFI-PE spectrum has been given above. The high intensity for the $^2\Pi_{3/2}(0_0^0)$ band compared to that of the $^2\Pi_{1/2}(0_0^0)$ band found in the TPE spectrum is likely due to contribution by nearby autoionizing Rydberg levels.

We have examined the widths of the $\tilde{X}\,^2\Pi_{3/2}(0_0^0)$ and $^2\Pi_{1/2}(0_0^0)$ bands under different experimental conditions. The width [$\geq$4.7 cm^{-1} (FWHM)] for the $\tilde{X}\,^2\Pi_{3/2}(0_0^0)$ band is found to be greater than that [$\geq$3.5 cm^{-1} (FWHM)] of the $^2\Pi_{1/2}(0_0^0)$ band. We note that the strong Rydberg state $17p\sigma_u$, is only about 10 cm^{-1} lower than the position of $\tilde{X}\,^2\Pi_{3/2}(0_0^0)$, whereas no strong autoionizing features are found in the vicinity of the position of $^2\Pi_{1/2}(0_0^0)$. It is possible that the Stark field induced ionization of the $17p\sigma_u$ state contributes to the observed width of the $\tilde{X}\,^2\Pi_{3/2}(0_0^0)$ band. Figure 10 compares a scan of the $\tilde{X}\,^2\Pi_{3/2}(0_0^0)$ band observed at F = 0.6 V/cm and a portion of the PIE spectrum shown in Fig. 2(a). The minor features marked by

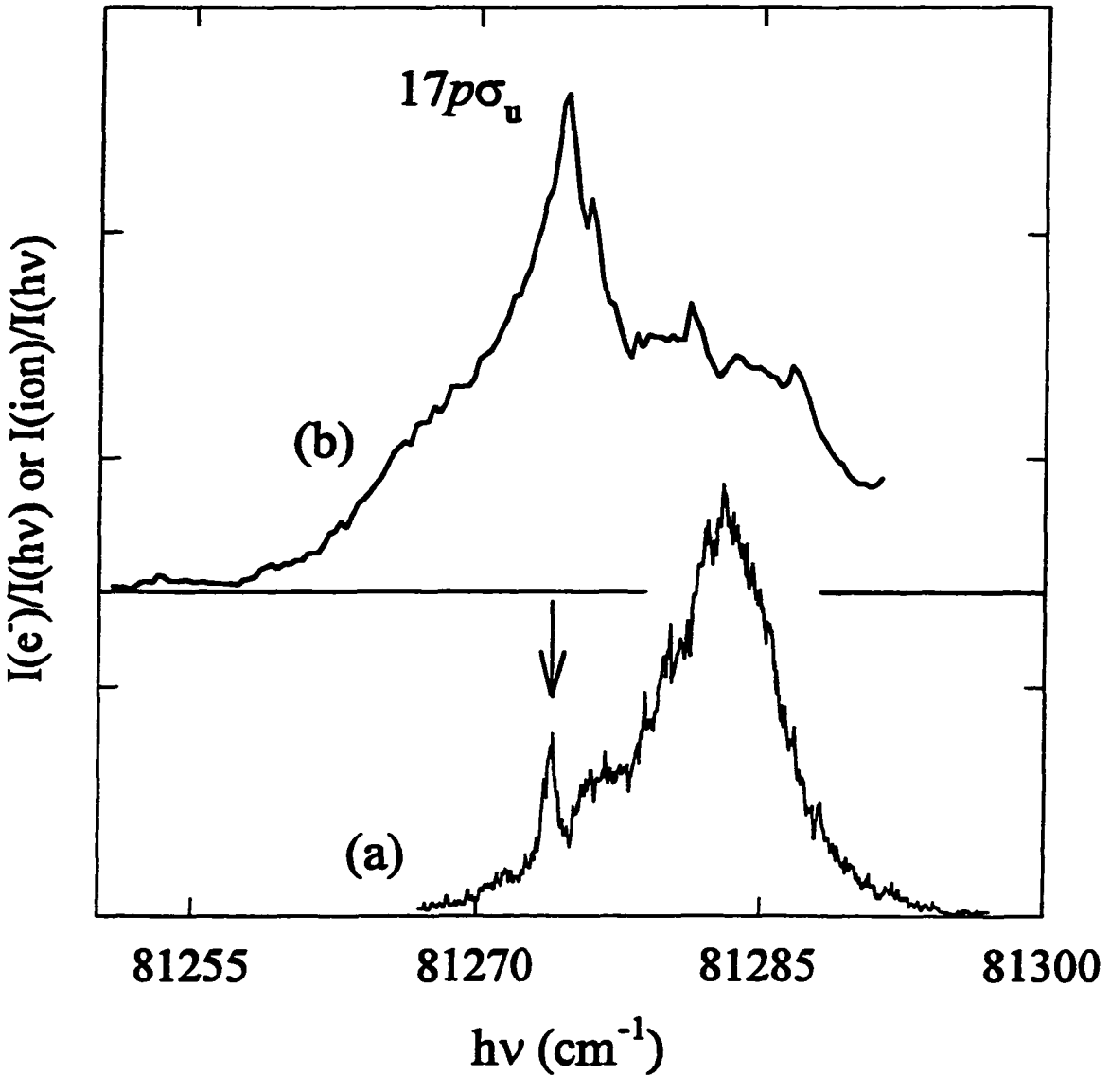

FIG. 10. Comparison of (a) the $^2\Pi_{3/2}(0_0^0)$ band and (b) the PIE spectrum for CS_2 in the energy region of 81 710-81 740 cm^{-1} obtained using the VUV laser. The PIE spectrum and PFI-PE band are obtained at F = 23 V/cm and a pulsed field of 0.6 V/cm, respectively. The structure marked by arrow in the $^2\Pi_{3/2}(0_0^0)$ band coincides with the position of $17np\sigma_u$.

The arrow in the $^2\Pi_{3/2}(0_0^0)$ band is found to coincide with the position of the $17np\sigma_u$ autoionizing state. The strength of this feature is most likely derived from initial excitation to the $17np\sigma_u$ Rydberg state. In the recent mass analyzed threshold ion (MATI) study of Ne,[10] the MATI peak for the $Ne^+(^2P_{3/2})$ state is also found to be affected by the nearby Rydberg state $13s'$. The latter Rydberg state is ≈18 cm^{-1} below IE[$Ne^+(^2P_{3/2})$].[10]

IV. CONCLUSION

We have performed a high resolution VUV photoionization, VUV-PFI-PE, TPE and Stark field ionization studies of CS_2 near the $CS_2^+(\tilde{X}\,^2\Pi_{3/2,1/2})$ thresholds. The VUV-PFI-PE spectrum has allowed the identification of more detailed Renner-Teller structures. An interesting observation is that the Franck-Condon factors for vibronic bands resolved in the VUV-PFI-PE and TPE spectra are in excellent agreement. A theoretical simulation of the $^2\Pi_{3/2}(0_0^0)$ and $^2\Pi_{1/2}(0_0^0)$ VUV-PFI-PE band profiles reproduces the observed branching ratio of two for $CS_2^+(^2\Pi_{3/2})/CS_2^+(^2\Pi_{1/2})$. Evidence is also found that the optically allowed autoionizing Rydberg state ($17p\sigma_u$), which is ≈10 cm^{-1} below IE[$CS_2^+(\tilde{X}\,^2\Pi_{3/2})$, contributes to the PFI-PE $^2\Pi_{3/2}(0_0^0)$ band structure. The analysis of the PIE spectra reveals three Rydberg series with the configurations $[^2\Pi_{1/2}]np\sigma_u$, $[^2\Pi_{1/2}]np\pi_u$ and $[^2\Pi_{1/2}]nf_u$ converging to the excited $CS_2^+(^2\Pi_{1/2})$ spin-orbit state. The Stark field study shows that it is important to correct for the Stark shift in IE measurements using the PIMS method.

Table III summaries the IE[$CS_2^+(\tilde{X}\,^2\Pi_{3/2,1/2})$], ν_1^+, ν_2^+ and A values determined in the present experiment and the previous N2P-PFI-PE study. As shown in the table, the IE values

Table III. Comparison of Spectroscopic constant for $CS_2(^1\Sigma_g^+)$ and $CS_2^+(\tilde{X}\,^2\Pi_{3/2,1/2})$.[a]

Method	State	IE(cm^{-1})	ν_1^+(cm^{-1})[b]	ν_2^+(cm^{-1})[b]	A(cm^{-1})
N2P-PFI-PE[c]	$^2\Pi_{3/2}$	81 286 ± 5	614	332	
	$^2\Pi_{1/2}$	81 726 ± 5	624[d]	320[e]($^2\Delta_{3/2}$)	-440
				342[e]($^2\Sigma^-$)	
VUV-PFI-PE	$^2\Pi_{3/2}$	81 284.8 ± 4.7	616	330($^2\Sigma^+$)	
				336($^2\Delta_{3/2}$)	
	$^2\Pi_{1/2}$	81 725.9 ± 3.5	...	321($^2\Delta_{3/2}$)	-441
				342($^2\Sigma^-$)	
Rydberg series					
Series I	$^2\Pi_{1/2}$	81 727.1 ± 0.5			
Series II	$^2\Pi_{1/2}$	81 726.3 ± 1.0			
Stark Shift	$^2\Pi_{3/2}$	81 287 ± 5[f]			
		81 285 ± 7[g]			

[a]All values except those of the N2P-PFI-PE study are obtained in the present experiment.
[b]Energies for the vibronic levels corresponding to excitation of one quantum of ν_1^+ or ν_2^+. Energies are measured with respect to that of $CS_2^+(\tilde{X}\,^2\Pi_{3/2}; 0,0,0)$ or $CS_2^+(^2\Pi_{1/2}; 0,0,0)$.
[c]Table 1 of Reference 30.
[d]Table 2 of Reference 30.
[e]Values of 341 and 391 cm^{-1} are given in Table 2 of Ref. 30.
[f]VUV laser experiment.
[g]Synchrotron study.

determined by the N2P-PFI-PE, VUV-PFI-PE, Rydberg series analysis and Stark field extrapolation methods agree to within ±1 cm^{-1}, indicating that the IE[$CS_2^+(\tilde{X}\,^2\Pi_{3/2,1/2})$] values determined here and in the previous N2P-PFI-PE experiment are highly accurate. Taking the average of these independent determinations, we recommend a value of 81 285.7 ± 2.8 cm^{-1} for IE[$CS_2^+(\tilde{X}\,^2\Pi_{3/2})$]. For IE[$CS_2^+(^2\Pi_{1/2})$], we prefer the value of 81 727.1 ± 0.5 cm^{-1} determined by the Rydberg series analysis. The ν_1^+, ν_2^+ and A values derived from the VUV and N2P studies are also in excellent agreement.

ACKNOWLEDGEMENTS

C.Y.N. is grateful to Prof. J. Hepburn for valuable discussion and assistance concerning the experimental arrangements for the generation of coherent VUV radiation. C.Y.N. acknowledges the donors of Petroleum Research Fund, administered by the American Chemical Society, for partial support of this research. This work was supported by the Director, Office of Energy Research, Office of Basic Energy Sciences, Chemical Sciences Division of the U.S. Department of Energy under Contract No. W-7405-Eng-82 for the Ames Laboratory and Contract No. DE-AC03-76SF00098 for the Lawrence Berkeley National Laboratory. C.Y.N. also acknowledges NSF for a Chemical Instrumentation Grant (CHE-9509795) which supports part of the construction of the VUV laser system used in this study. Y.S.C. is a Henry Gilman Fellow, (1996-1997). M.E. is a GAANN Fellowship recipient, 1993-1995 and 1996-1997.

Note added in proof. The 81274 cm^{-1} peak of the PFI-PE spectrum [Fig. 10(a)] appears to be more satisfactorily assigned as $[(0,1,0)^2\Sigma_{1/2}^-]18p\sigma \leftarrow (0,1,0)^1\Pi_u^-$ (see C. Cossart-Magos, Philo. Roy. Soc. Series A, **355**, to be published in June 1997).

REFERENCES

[1] *Vacuum Ultraviolet Photoionization and Photodissociation of Molecules and Clusters*, eidted by C. Y. Ng, (World Scientific, Singapore, 1991).

[2] J. A. R. Samson, *Techniques of Vacuum Ultraviolet Spectroscopy* (Wiley, New York, 1967).

[3] J. W. Hepburn, in *Vacuum Ultraviolet Photoionization and Photodissociation of Molecules and Clusters*, edited by C. Y. Ng (World Scientific, Singapore, 1991), p. 435.

[4] A. H. Kung and Y. T. Lee, in *Vacuum Ultraviolet Photoionization and Photodissociation of Molecules and Clusters*, edited by C. Y. Ng (World Scientific, Singapore, 1991), p. 487.

[5] R. H. Page, R. J. Larkin, A. H. Kung, Y. R. Shen, and Y. T. Lee, Rev. Sci. Instrum. **58**, 1616 (1987).

[6] A. H. Kung, Opt. Lett. **8**, 24 (1983).

[7] E. Cromwell, T. Trickl, Y. T. Lee, and A. H. Kung, Rev. Sci. Instrum. **60**, 2888 (1989).

[8] J. W. Hepburn, in *Laser Techniques in Chemistry*, edited by A. Meyers and T. R. Rizza (Wiley, New York, 1994).

[9] P. Heimann, M. Koike, A. H. Kung, C. Y. Ng, M. G. White, and A. Wodtke, Lawrence Berkeley Laboratory Workshop Report on Application of Synchrotron Radiation in Chemical Dynamics, Feb., 1993, Oakland CA.

[10] C.-W. Hsu, M. Evans, P. Heimann, T.-K. Lu, Y.-J. Chen, and C. Y. Ng, J. Chem. Phys., **105**, 3950 (1996).

[11] P. A. Heimann, C.-W. Hsu, M. Evans, C. Y. Ng, M. Koike, D. Blank, X. M. Yang, C. Flaim, A. G. Suits, and Y. T. Lee, Rev. Sci. Instrum. (submitted).

[12] *High Resolution Laser Photoionization and Photoelectron Studies, Wiley Series in Ion Chemistry and Physics* edited by I. Powis, T. Baer, and C. Y. Ng (Wiley, Chichester, 1995).

[13] M. Koike, P. A. Heimann, A. H. Kung, T. Namioka, R. DiGennaro, B. Gee, and N. Yu, Nucl. Instrum. Methods A **347**, 282 (1994).

[14] When ALS is operated in the multi-bunch mode, the entire orbit contains 320 bunches. An individual bunch has a duration of 50 ps and is separated from adjacent bunches by 2 ns. There is a 16 ns gap at the end of ring period. Thus, the synchrotron radiation at ALS has a repetition rate of 488.5 MHz and is effectively a cw VUV source.

[15] R. Hilbig and R. Wallenstein, IEEE J. QE **19**, 1759 (1983).

[16] R. Hilbig, G. Hilberg, and R. Wallenstein, Appl. Phys. B **41**, 225 (1986).

[17] K. Müller-Dethefs, M. Sander, and E. W. Schlag, Z. Naturforsch. Teil **A 39**, 1089 (1984).

[18] K. Müller-Dethefs and E. W. Schlag, Annu. Rev, Phys. Chem. **42**, 109 (1991).

[19] P. Guyon and T. Baer, in Ref. 12, p. 1.

[20] Y. Morioka, Y. Lu, T. Matsui, T. Tanaka, H. Yoshi, T. Hayaishi, and R. I. Hall, J. Chem. Phys. **104**, 9357 (1996).

[21] E. Waterstradt, R. Jung, H.-J. Dietrich, and K. Müller-Dethefs, et al. Rev. Sci. Instrum. **64**, 3104 (1993).

[22] K.-M. Weitzel and F. Güthe, Chem. Phys. Lett. **251**, 295 (1996).

[23] L. Zhu and P. Johnson, J. Chem. Phys. **94**, 5769 (1991).

[24] C. Jouvet, C. Dedonder-Lardeux, S. Martrenchard-Barra, and D. Soldagi, Chem. Phys. Lett. **198**, 419 (1992).

[25] H. Krause and H. J. Neusser, J. Chem. Phys. **97**, 5923 (1992).

[26] S. T. Pratt, J. Chem. Phys. **98**, 9241 (1993).

[27] H. Krause and H. J. Neusser, J. Chem. Phys. **99**, 6278 (1993).

[28] Y. Ono, S. H. Linn, H. F. Prest, M. E. Gress, and C. Y. Ng, J. Chem. Phys. **73**, 2523 (1980).

[29] W. M. Trott, N. C. Blais, and E. A. Walters, J. Chem. Phys. **71**, 1692 (1979).

[30] I. Fischer, A. Lochschmidt, A. Strobel, G. Niedner-Schatteburg, K. Müller-Dethefs, and V. E. Bondybey, Chem. Phys. Lett. **202**, 542 (1993).

[31] L.-S. Wang, J. E. Reutt, Y. T. Lee, and D. A. Shirley, J. Electron Spectrosc. Relat. Phenom. **47**, 167 (1988).

[32] R. Frey, B. Gotchev, W. B. Petman, H. Pollak, and E. W. Schlag, Int. J. Mass Spectrom. Ion Phys. **26**, 137 (1978).

[33] I. Reineck, B. Wanneberg, H. Veenhuizen, C. Nohre, R. Maripuu, K. E. Norell, L. Mattson, L. Karlsson, and K. Siegbahn, J. Electron Spectrosc. **34**, 235 (1984).

[34] W. A. Chupka, J. Chem. Phys. **98**, 4520 (1993).

[35] Y. Tanaka, A. S. Jursa, and F. J. LeBlanc, J. Chem. Phys. **32**, 1205 (1960).

[36] The electronic configuration is predicted by calculations using the GAUSSIAN 94 for Window package. M. J. Frisch *et al.*, GAUSSIAN 94 (Gaussian, Pittsburgh, PA 1994).

[37] C. Blanquet, E. Baeten, I. Cauuet, J. Walrand, and C. P. Courtoy, J. Mol. Spectrosc. **112**, 55 (1985).

[38] M. Brommer and P. Rosmus, Chem. Phys. Lett. **206**, 540 (1993).

[39] S. Carter and N. C. Handy, Mol. Phys. **52**, 1367 (1984).

[40] S. Carter, N. C. Handy, P. Rosmus, and G. Chambaud, Mol. Phys. **71**, 605 (1990).

[41] G. Herzberg, *Molecular Spectra and Molecular Structure III* (Van Nostrand, New York, 1966).

[42] W. J. Balfour, Can. J. Phys. **54**, 1969 (1976).

[43] M. Endoh, M. Tsuji, and Y. Nishimura, Chem. Phys. Lett. **109**, 35 (1984).

[44] V. E. Bondybey, J. H. English, T. A. Miller, J. Chem. Phys. **70**, 1621 (1979).

[45] V. E. Bondybey and J. H. English, J. Chem. Phys. **73**, 3098 (1980).

[46] R. T. Wiedmann, M. G. White, H. Lefebvre-Brion, and C. Cossart-Magos, J. Chem. Phys. **103**, 10417 (1995).

[47] C.-W. Hsu, D. P. Baldwin, C.-L. Liao, and C. Y. Ng, J. Chem. Phys. **100**, 8047 (1994).

[48] C.-W. Hsu and C. Y. Ng, J. Chem. Phys. **101**, 5596 (1994).

[49] C.-W. Hsu, C.-L. Liao, Z.-X, Ma, P. J. H. Tjossem, and C. Y. Ng, Chem. Phys. Lett. **199**, 78 (1992).

[50] C.-W. Hsu, C.-L. Liao, Z.-X. Ma, P.J. H. Tjossem, and C. Y. Ng, J. Chem. Phys. **97**, 6283 (1992).

[51] A. G. Suits, P. Heimann, X.-M. Yang, M. Evans, C.-W. Hsu, K.-T. Lu, Y. T. Lee, and A. H. Kung, Rev. Sci. Instrum. **66**, 4841 (1995).

[52] T. Baer, W. B. Peatman, and E. W. Schlag, Chem. Phys. Lett. **4**, 243 (1969).

[53] W. C. Price and D. M. Simpson, Proc. R. Soc. London, Ser. A **165**, 272 (1938).

[54] M. Larzilliere and N. Damany, Can. J. Phys. **56**, 1150 (1978).

[55] F. R. Greening and G. W. King, J. Mol. Spectrom. Ion Phys. **1**, 111 (1968).

[56] E. Lindholm, Arkiv Fysik. **40**, 97 (1968).

[57] R. A. Morgan, M. A. Baldwin, A. J. Orr-Ewing, M. N. R. Ashfold, W. J. Buma, J. B. Milan, and C. A. de Lange, J. Chem. Phys. **104**, 6117 (1996).

[58] C. Cossart-Magos and H. Lefebvre-Brion, Mol. Phys. **85**, 821 (1995), and references therein.

[59] We have examined the width of the $^2\Pi_{3/2}(0_0^0)$ and $^2\Pi_{1/2}(0_0^0)$ bands at different experimental conditions. These widths represent the smallest values obtained.

[60] C. Cossart-Magos, M. Horani, M. Jungen, and F. Launay, J. Chem. Phys. **104**, 7412 (1996).

[61] C. Cossart-Magos, M. Jungen, and F. Launay, J. Chem. Phys. (to be submitted).

[62] H. Lefebvre-Brion, Chem. Phys. Lett. **253**, 43 (1996).

[63] N. Knoblauch, A. Strobel, I. Fischer, and V. E. Bondybey, J. Chem. Phys. **103**, 5417 (1995).

[64] A, Strobel, A. Lochschmidt, I. Fisher, G. Niedner-Schatteburg, and V. E. Bondybey, J. Chem. Phys. **99**, 733 (1993).

CHAPTER 5. VACUUM ULTRAVIOLET LASER PULSED FIELD IONIZATION PHOTOELECTRON STUDIES OF POLYATOMIC SPECIES: ACCURATE IONIZATION ENERGIES OF CH_3SH AND CH_3CH_2SH

A paper published in the Journal of Chemical Physics

Y.-S. Cheung, J.-C. Huang and C. Y. Ng

ABSTRACT

The vacuum ultraviolet (VUV) pulsed field ionization photoelectron (PFI-PE) spectra for CH_3SH and CH_3CH_2SH have been obtained near their ionization thresholds. Using a semi-empirical simulation scheme, we have obtained satisfactory fits to fine structures resolved in the VUV-PFI-PE spectra, yielding accurate ionization energies of 76 256.3 ± 2.9 cm^{-1} (9.45458 ± 0.00036 eV) and 74 948.7 ± 2.9 cm^{-1} (9.29246 ± 0.00036 eV) for CH_3SH and CH_3CH_2SH, respectively.

I. INTRODUCTION

Accurate ionization energies (IEs) for molecular species are of fundamental importance to chemists,[1] which are used for prediction of chemical reactivity, such as in electron transfer reactions. The combination of the IE and heat of formation at 0 K ($\Delta_f H°_0$) of a neutral molecule yields the $\Delta_f H°_0$ value for the corresponding cation. Thus, accurate experimental IE determination is valuable to ion chemistry in general. A great number of IE values for molecules in the literature has been measured by single-photon vacuum ultraviolet (VUV) photoionization mass spectrometry[2,3] and photoelectron spectroscopy[4-6] using monochromatized laboratory discharge lamps and synchrotron radiation as the light sources.

Due to the limitation in the photon energy resolution for these monochromatized light sources, the uncertainties for IE values measured are in the range of 0.003-0.10 eV.[1,2] As a result of the hot band and kinetic shift effects, the accurate IE determination for polyatomic molecules is specially challenging.[2] The application of molecular beam techniques has shown to reduce the hot band effect and thus improve the actual experimental resolution.[7] In the theoretical front, IE values of small and medium size molecules and radicals consist of some main group elements can now be predicted by high level *ab initio* calculations[8] to an accuracy of <0.15 eV, comparable to experimental uncertainties.[9] This theoretical achievement challenges experimentalists to make IE measurements with higher accuracy.

In the past decade, significant advances have also been made in experimental techniques for accurate IE measurements.[10,11] Due to the development of modern vacuum ultraviolet (VUV) light sources, such as tunable VUV lasers[12,13] and third generation synchrotron radiations,[14] together with new experimental schemes,[10,11,14,15] IE values for many polyatomic species have been reported to uncertainties of 1-8 cm^{-1}.[10,16] The uncertainties for the IE values of a few polyatomic species are lower than 1 cm^{-1}.[16] One of the most general and accurate techniques for IE measurements is VUV pulsed field ionization photoelectron (PFI-PE) spectroscopy.[15] When a rotationally resolved PFI-PE spectrum of a molecule is obtained, the analysis of the spectrum could lead to a definitive IE value. The obtainable resolution for VUV-PFI-PE spectroscopy is limited by both the resolution of the VUV laser and the nature of the pulsed electric field.[10] The common resolutions achieved in PFI-PE measurements are in the range of 1-3 cm^{-1}.[10,16] Since the rotational constants for polyatomic species are usually 10 fold smaller than this resolution range, the PFI-PE spectrum for a polyatomic molecule is not

expected to be fully rotational-resolved. A typical PFI-PE vibrational band for a polyatomic molecule exhibits a FWHM of 10-20 cm^{-1}.[17,18] Nevertheless, fine structures should still be observable in PFI-PE vibrational bands measured at a resolution of 1-3 cm^{-1}.[18] These fine structures are resulted from the overlap of many unresolved rotational transitions. An appropriate simulation of the spectra would provide information about the IE to an accuracy close to the instrumental PFI-PE resolution (1-3 cm^{-1}) instead of an uncertainty set by the FWHM (10-20 cm^{-1}) of the PFI-PE vibrational band. A successful simulation of the PFI-PE bands for nascent CH_3S radicals formed in the photodissociation of CH_3SH and CH_3SSCH_3 has been made previously.[18] Despite that the CH_3S radicals are rovibronically excited, we have obtained an IE value for CH_3S to an accuracy of 8 cm^{-1}.[18]

If the molecular species of interest is cooled by pulsed supersonic expansion prior to the PFI-PE measurement, the contours of rotational bands are expected to be sharper and thus providing more detailed features for spectral simulation. Theoretical models for accurate predictions of transition line strengths in rotationally-resolved photoelectron studies of polyatomic species are not available. Our goal is to employ a semi-empirical scheme for simulating contours of rotational branches resolved in high resolution photoelectron spectra of cold polyatomic molecules. As demonstrated below, we have obtained more accurate IE values for CH_3SH and CH_3CH_2SH by the simulation of fine structures resolved in the first (or 0-0) vibrational VUV-PFI-PE bands of these molecules. In the previous non-resonance two-photon PFI-PE (N2P-PFI-PE) studies of CH_3SH and CH_3CH_2SH, the values for IE of these molecules were determined to the uncertainties of ±5 cm^{-1}.[17] The latter results are based on the assumption that the peak positions observed in the 0-0 vibrational N2P-PFI-PE bands

correspond to the true adiabatic IE values for CH_3SH and CH_3CH_2SH. Since rotational fine structures were not observed in the N2P-PFI-PE study, we were not able to perform a simulation to support this assumption. We find that the resolution achieved in VUV-PFI-PE measurements[19] is generally higher than those[17,20] observed in N2P-PFI-PE studies. The fact that the ultraviolet laser beam has to be focused at the target molecules in N2P-PFI-PE studies is expected to promote multi-photon ionization and dissociation processes. The saturation effect and higher electron background generated from these multi-photon processes might degrade the obtainable resolution.

II. EXPERIMENT

The experimental apparatus and procedures used are similar to those described previously.[19] The apparatus consists of a tunable VUV laser source, a pulsed molecular beam source, an ion time-of-flight (TOF) mass spectrometer and an electron detector for PFI-PE detection.

The VUV laser system is comprised of one excimer laser (Lambda Physik EMG201), two dye lasers (Lambda Physik FL3002) and a Kr gas cell. The XeCl (308 nm) output (200-250 mJ) of the excimer laser was split to pump the two dye lasers. The output frequencies ω_1 and ω_2 of the dye lasers were mixed in a Kr gas cell. In this experiment, the VUV frequencies used correspond to the difference frequencies $2\omega_1 - \omega_2$. One dye laser is fixed at the ultraviolet frequency ω_1 = 47 046.87 cm^{-1}, which matches the two-photon resonance of the Kr $4p \rightarrow 5p$ transition. The other dye laser is tuned in the visible frequency (ω_2) range of 18 519-20 000 cm^{-1}. The visible laser beam is merged with the ultraviolet laser beam by a dichromic mirror.

Both beams were then focused into the Kr cell (pressure = 30 Torr) by a focusing lens (focal length = 15 cm). The gas cell has a quartz entrance window and a MgF_2 exit windows, which serves to isolate the gas cell from the photoexcitation/photoionization (PEX/PI) chamber. With a transmission cut-off wavelength of ≈115 nm, the MgF_2 window allows the VUV different frequency to transmit while absorbing the VUV sum frequency.

A photoelectric detector made out of Cu was used to measure the VUV laser photon intensities. In addition to monitoring the VUV light intensities, the photoelectric detector also served as a light trap for ω_1, ω_2 and VUV radiations. However, by blocking the visible laser beam, we found that ≈90% of photoelectric current is contributed by the ultraviolet laser beam. Fortunately, this background is constant because the UV frequency is fixed. We find that the intensity of the VUV difference frequency is also nearly constant over the VUV range of ≈1000 cm^{-1} in this study. Thus, the PFI-PE data presented here have not been normalization by the VUV intensities.

To calibrate the laser frequencies, a small fraction of the dye laser (ω_2) output was directed into a uranium hollow cathode tube with Ne as the buffer gas. The Ne absorption spectrum recorded simultaneously during the experiment provided accurate calibration of the PFI-PE spectra. The bandwidths of the dye lasers are 0.2 cm^{-1} for the fundamental and ≈0.4 cm^{-1} for the second harmonic outputs. For a two-photon excitation, the resolution is ≈0.8 cm^{-1}. Thus, the resolution for the VUV laser radiation generated by difference frequency mixing is estimated to be ≤1 cm^{-1}. The accuracy of photon frequencies given here is expected to be ±0.2 cm^{-1}.

The samples (CH_3SH or CH_3CH_2SH) are introduced into the vacuum chamber by a pulsed valve operated at 10 Hz with a 300-μs open time. A typical gas mixture used is 20% of the sample buffered by He or Ar at a total pressure of ≈1290 Torr. The molecular beam is skimmed by a conical skimmer (1-mm diameter, 3.8 cm from the nozzle) before intersecting with a tunable VUV laser beam (90°, 8.3 cm downstream from the skimmer). The molecular beam source chamber was pumped by a freon-trapped, 6-in. diffusion pump (pumping speed ≈ 2,000 L/s), while the photoionization chamber and the ion-TOF tube were evacuated by turbomolecular pumps with pumping speeds of 250 and 50 L/s, respectively. During the experiment, the beam source chamber and the photoionization chamber were maintained at pressures of $\approx 5 \times 10^{-5}$ and $\approx 5 \times 10^{-7}$ Torr, respectively.

Electrons and ions formed at the PE/PI region are extracted at opposite directions and orthogonal to both VUV and molecular beams. One set of channel plates is installed at the end of the ion TOF drift tube to detect ions and the other set of channel plates is located right below the PEX/PI region to detect electrons. The signals from the electron detector (or ion detector) and the photoelectric VUV detector were fed into two identical boxcar integrators (Stanford Research SR250), which were interfaced to an IBM/PC computer. The electron (or ion) and VUV laser signals were averaged for 30 laser shots at each VUV frequency. The spectra shown here represent the averages of 4-5 independent scans obtained at the same experimental conditions.

The firing sequence of the pulsed valve, dye laser and pulsed electric field is controlled by two digital delay units (Stanford Research DG535). In this experiment, the firing of the VUV excitation laser was delayed by 520 μs with respect to the triggering pulse for opening the

pulsed valve. After a typical delay of 2.5 μs with respect to the firing of the VUV laser, a pulsed (duration = 1 μs) electric field of ≈0.9 V/cm was used to field-ionize the high-*n* Rydberg species as well as to extract the electrons to the microchannel plate detector.

III. RESULTS AND DISCUSSION

We have obtained the VUV-PFI-PE spectra for CH_3SH and CH_3CH_2SH in the photon energy ranges of 76 100-77 000 and 74 600-75 800 cm^{-1}, respectively. The VUV-PFI-PE spectrum for CH_3SH in the region of 76 210-76 310 cm^{-1} is shown in Fig. 1(a), while that for CH_3CH_2SH in the region of 74 922-74 985 cm^{-1} is depicted in Fig. 2(a). Since the other portions of the VUV-PFI-PE spectra for CH_3SH and CH_3CH_2SH are essentially identical to those reported in the N2P-PFI-PE study,[17] they are not shown here. The VUV photoionization efficiency spectra for CH_3SH and CH_3CH_2SH (not shown here) have also been recorded. These spectra are also in agreement with those observed in previous N2P[17] and VUV photoionization efficiency studies.[21] We note that due to multi-photon ionization and dissociation processes, the photoionization efficiency spectrum for CH_3CH_2SH could not observed in the previous N2P-PIE study.[17]

We have compared in Table I the peak positions of vibrational bands observed in the VUV-PFI-PE and N2P-PFI-PE[17] spectra for CH_3CH_2SH. These positions are measured with respect to the peak position of the 0-0 vibrational PFI-PE band for CH_3CH_2SH. The previous *ab initio* calculations show that CH_3CH_2SH and $CH_3CH_2SH^+$ may exit as the *trans*- or *gauche*-conformer.[17] For both CH_3CH_2SH and $CH_3CH_2SH^+$, the *gauche*-conformer is predicted to be slightly more stable than the *trans*-conformer. The theoretical predictions for the relevant

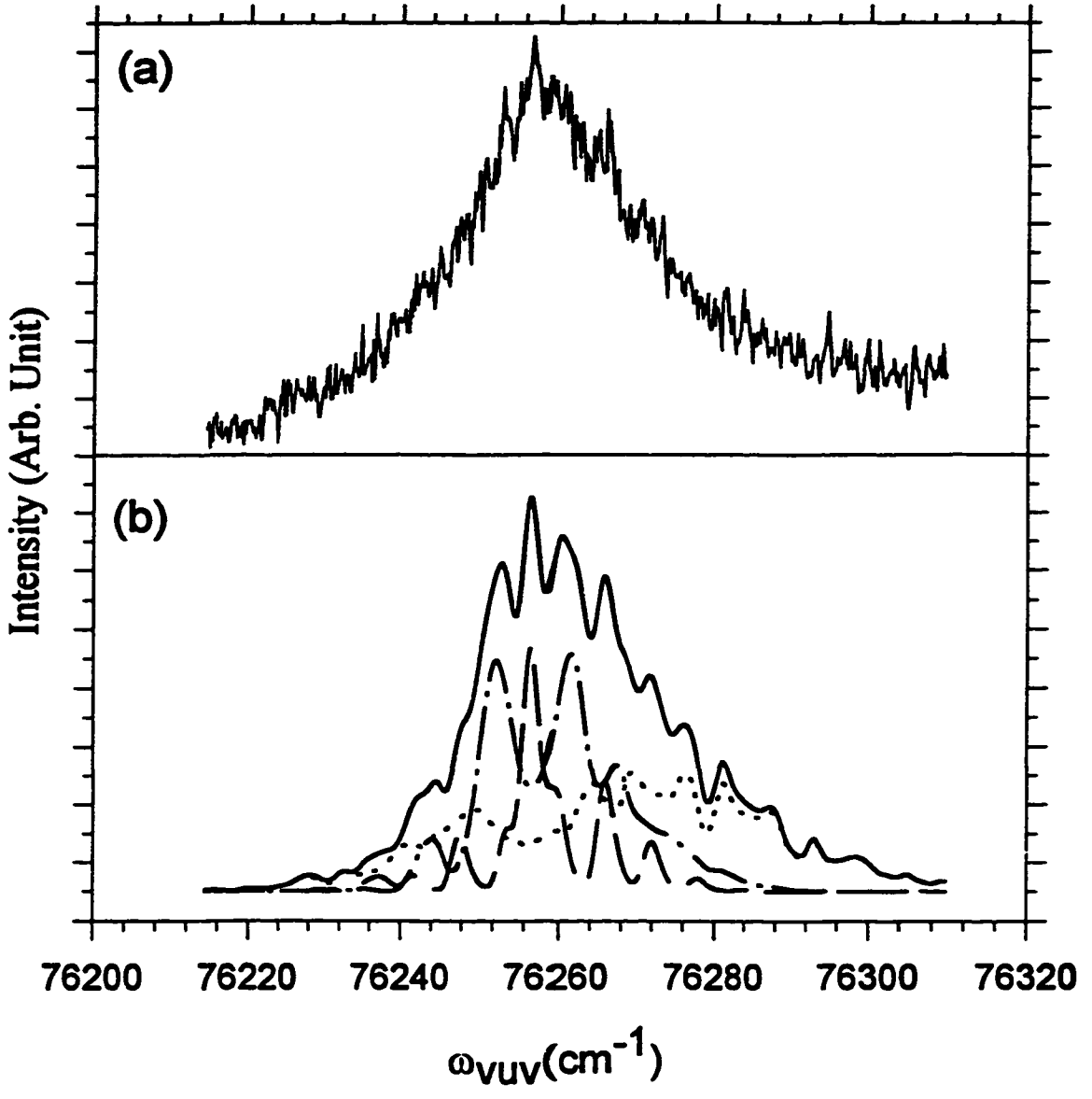

FIG. 1. (a) VUV-PFI-PE spectrum of CH_3SH in the photon energy range of 76 210-76 310 cm^{-1}. (b) Simulated spectrum for CH_3SH (solid line) obtained by using a rotational temperature of 20 K and a Gaussian width of 2 cm^{-1} (FWHM). The contributions by various rotational branches are marked: (dashed curve) ($\Delta J = 0$; $\Delta K = 0, \pm 1$), (dash-dotted curve) ($\Delta J = \pm 1$; $\Delta K = 0, \pm 1$) and (dotted curve) [($\Delta J = 0, \pm 1$; $\Delta K = \pm 2$) plus ($\Delta J = \pm 2$; $\Delta K = 0, \pm 1, \pm 2$)].

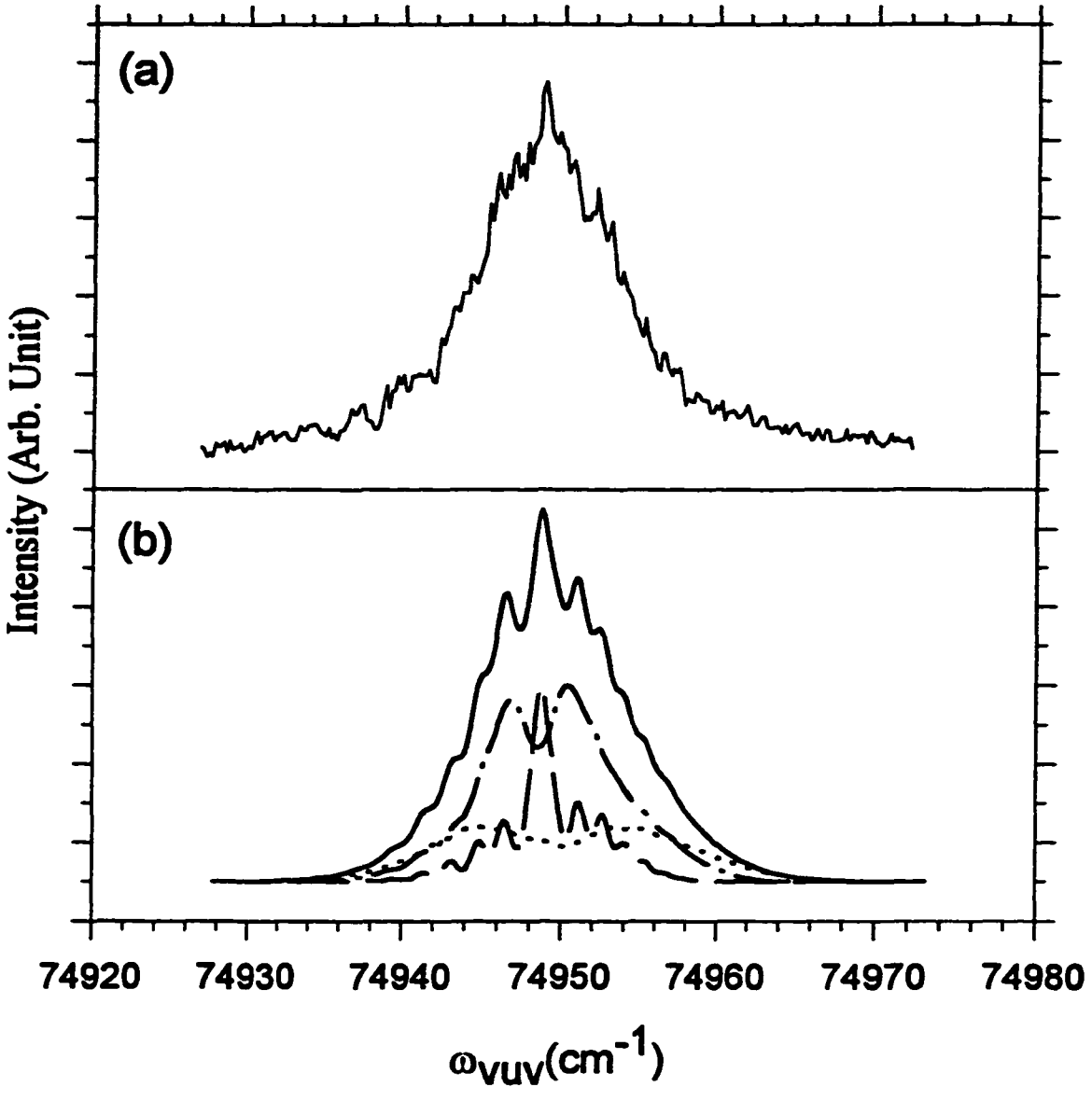

FIG. 2. (a) VUV-PFI-PE spectrum of CH_3CH_2SH in the photon energy range of 74 927-74 973 cm^{-1}. (b) Simulated spectrum for CH_3CH_2SH (solid line) obtained by using a rotational temperature of 15 K and Gaussian width of 1 cm^{-1} (FWHM). The contributions by various rotational branches are marked: (dashed curve) ($\Delta J = 0$; $\Delta K = 0, \pm 1$), (dash-dotted curve) ($\Delta J = \pm 1$; $\Delta K = 0, \pm 1$) and (dotted curve) [($\Delta J = 0, \pm 1$; $\Delta K = \pm 2$) plus ($\Delta J = \pm 2$; $\Delta K = 0, \pm 1, \pm 2$)].

Table I. Comparison of experimental and theoretical vibrational frequencies for $CH_3CH_2SH^+$.

Assignment[a]	Theoretical (cm^{-1})[a]	N2P-PFI-PE (cm^{-1})[a]	VUV-PFI-PE (cm^{-1})[b]
ν_1 $e_2 \rightarrow e_1^+$	-129	—	-149
ν_1^+ $e_1 \rightarrow e_2^+$	93	116	119
$o_1 \rightarrow o_2^+$	169	144	145
ν_3^+	289	288	292
ν_4^+	615	628	623

[a]Reference 17.
[b]This work.

vibrational frequencies of CH_3CH_2SH and $CH_3CH_2SH^+$, are also included in Table I.[17] Taking into account the experimental uncertainties, the vibrational quanta for ν_3^+ and ν_4^+ observed in this VUV study and the N2P-PFI-PE experiment are in good agreement. The positions of the doublet observed in the N2P-PFI-PE experiment[17] at 116 and 144 cm^{-1} are also confirmed at 119 and 145 cm^{-1} in the VUV-PFI-PE spectrum for CH_3CH_2SH. This doublet has been attributed to the transitions from the vibrational states e_1 and o_1 of the torsional potential for CH_3CH_2SH to the respective vibrational states e_2^+ and o_2^+ of the torsional potential for $CH_3CH_2SH^+$. The VUV-PFI-PE spectrum reveals a band at -149 cm^{-1}, which is assigned to the $e_2 \rightarrow e_1^+$ hot band transition. The latter transition is predicted to be at -129 cm^{-1} by the theoretical calculations.[17]

The assignment[17] of the vibrational structures for the CH_3SH/CH_3SH^+ and CH_3CH_2SH/CH_3CH_2SH systems is based on the assumption that the peak positions of the 0-0 PFI-PE vibrational bands of CH_3SH^+ and *gauche*-$CH_3CH_2SH^+$ correspond to the adiabatic IEs of CH_3SH and *gauche*-CH_3CH_2SH, respectively. A careful examination of the 0-0 PFI-PE

bands for CH_3SH [Fig. 1(a)] and CH_3CH_2SH [Fig. 2(a)] reveals fine structures, which are not observed in the N2P-PFI-PE study.[17] As indicated above, the main purpose of this article concerns the simulation of these fine structures observed in the 0-0 VUV-PFI-PE bands for CH_3SH and CH_3CH_2SH. The geometries of most polyatomic molecules and radicals are low symmetry species, as in the case of CH_3SH and CH_3CH_2SH. Thus, the semi-empirical scheme used and rationalization presented here should be generally applicable for simulating the photoelectron or PFI-PE spectra of other polyatomic species obtained with a similar energy resolution.

In order to perform the simulation, we need the rotational constants for the neutrals and their cations in their ground states. The rotational constants for the neutrals (A″, B″, C″), CH_3SH and CH_3CH_2SH and the cations (A^+, B^+, C^+), CH_3SH^+ and $CH_3CH_2SH^+$, obtained by *ab initio* calculations at the restricted Hartree-Fock level with the 6-31G(d) basis set are listed in Table II. These calculations were made using the Gaussian 94 package program.[22] The calculations indicate that the neutral CH_3SH (CH_3CH_2SH) and cation CH_3SH^+ ($CH_3CH_2SH^+$) have similar geometries as shown by the rotational constants in the table. The asymmetry parameters (κ) [defined as $(2B'' - A'' - C'')/(A'' - C'')$ for the neutrals and $(2B^+ - A^+ - C^+)/(A^+ - C^+)$ for the ions] are -0.99 for CH_3SH and CH_3SH^+ and -0.96 for $CH_3CH_2SH/CH_3CH_2SH^+$. Hence, the four species are all asymmetric top molecules. Here, the rotational energies (E_{rot}) of these asymmetric top molecules are obtained by diagonalization of the Hamiltonian matrix using the symmetric top rotational basis set.[23] Since the κ values are very close to -1, CH_3SH (CH_3CH_2SH) and CH_3SH^+ ($CH_3CH_2SH^+$) are near prolate top molecules. Thus, it is reasonable

Table II. Calculated rotational constants (A″, B″, C″) for CH_3SH and CH_3CH_2SH, and (A^+, B^+, C^+) for CH_3SH^+ and $CH_3CH_2SH^+$.

Molecule or ion	A″ or A^+ (cm^{-1})	B″ or B^+ (cm^{-1})	C″ or C^+ (cm^{-1})
CH_3SH	3.50	0.43	0.41
CH_3CH_2SH	0.965	0.177	0.162
CH_3SH^+	3.46	0.46	0.44
$CH_3CH_2SH^+$	0.937	0.182	0.166

to assume that K_a'' (K_a^+) is a good quantum number for the neutral (ion) species. Here, we represent K_a'' (K_a^+) as K″ (K^+).

Under this assumption, the rotational eigenstates for CH_3SH (CH_3CH_2SH) and CH_3SH^+ ($CH_3CH_2SH^+$) can be characterized as $|J'', K''\rangle$ and as $|J^+, K^+\rangle$, where J″ and J^+ are the total angular momentum quantum numbers for the neutral and ion species, respectively. In the case of PFI-PE measurements, the final state $|J', K'\rangle$ consists of an ion core and a high-n ($n \geq 100$) Rydberg electron. Considering that the Rydberg electron are only weakly bound to the ion core, the final state wavefunction (excluding electron spins) to a first approximation can be described by the product of the rotational state $|J^+, K^+\rangle$ for the ion core and the Rydberg state $|n, \ell, m_l\rangle$ for the electron,

$$|J', K'\rangle = |J^+, K^+\rangle |n, \ell, m_l\rangle, \quad (1)$$

where

$$J' = J^+ + \ell \quad (2)$$

and

$$K' = K^+ + m_l. \quad (3)$$

The dipole transition selection rules from $|J'', K''\rangle$ to $|J', K'\rangle$ for the parallel bands are

$$\Delta J_n = 0, \pm 1 \text{ and } \Delta K_n = 0 \text{ for } K'' \neq 0 \text{ and} \quad (4a)$$

$$\Delta J_n = \pm 1 \text{ and } \Delta K_n = 0 \text{ for } K'' = 0. \quad (4b)$$

For perpendicular bands, we have

$$\Delta J_n = 0, \pm 1 \text{ and } \Delta K_n = \pm 1, \quad (5)$$

where $\Delta J_n = J' - J''$ and $\Delta K_n = K' - K''$. The selection rules can be expressed in terms of $\Delta J = J^+ - J''$ and $\Delta K = K' - K''$. Using Eqs. (2)-(4), we obtain the selection rules for $\ell = 0$ as given by Eqs. (6a) and (6b) for parallel bands, and by Eq. (7) for perpendicular bands.

$$\Delta J = 0, \pm 1 \text{ and } \Delta K = 0 \text{ for } K'' \neq 0 \text{ and} \quad (6a)$$

$$\Delta J = \pm 1 \text{ and } \Delta K = 0 \text{ for } K'' = 0. \quad (6b)$$

$$\Delta J = 0, \pm 1 \text{ and } \Delta K = \pm 1. \quad (7)$$

For $\ell = 1$, the selection rules for parallel and perpendicular bands are given in Eqs.(8) and (9), respectively.

$$\Delta J = 0, \pm 1, \pm 2 \text{ and } \Delta K = 0, \pm 1 \quad (8)$$

$$\Delta J = 0, \pm 1, \pm 2 \text{ and } \Delta K = 0, \pm 1, \pm 2. \quad (9)$$

We use the conventional labeling O, P, Q, R and S branches for $\Delta J = J^+ - J'' = -2, -1, 0, 1$ and 2, respectively. Similarly, the consideration of $\ell \geq 2$ for the electron would allow contributions from $|\Delta J| \geq 3$ and $|\Delta K| \geq 3$ transitions. We note that for molecular species of low symmetry, such as CH_3SH/CH_3SH^+ and $CH_3CH_2SH/CH_3CH_2SH^+$, J^+ and J'' are identical to the rotational quantum numbers N^+ for the cation and N'' for the neutral, respectively, without consideration of the electron spin and orbital angular momenta. For threshold photoelectron (TPE) measurements, a first order wavefunction for the final state $| J', K' \rangle$ can be considered as the

product of the cation wavefunction $|J^+, K^+\rangle$ and the outgoing electron wavefunction $|\ell, m_l\rangle$. The couplings of the J^+ and ℓ and K^+ and m_l follow Eqs. (2) and (3), respectively, which result in the same selection rules for PFI-PE measurements involving a high-n Rydberg electron with the same ℓ value. The formation of an outgoing electron in a final angular momentum state ℓ from an ℓ'' state associated with the electronic ground state of the molecule can be considered in part the result of an angular momentum exchange arising from interaction (or scattering) of the ion core and the photoexcited electron involved. Knowing the rotational distribution of the ion core from experimental measurements, we can deduce the distribution of angular momentum states ℓ's of the outgoing electron by the conservation of angular momentum. The formation of an electron in a high-ℓ continuum state is not favorable in a threshold photoionization process. At the photoionization threshold, the high centrifugal barrier for an electron in a high-ℓ state prevents it from escaping into the ionization continuum.[24] Hence, the probability is also small for a large change in rotational quantum number of the ion core upon photoionization.

The physical interpretation of the selection rules for the TPE or high-*n* Rydberg electron formation is that the electron can exchange a finite angular momentum with the ion core during the photoexcitation or photoionization process. This interaction in effect relaxes of the optical selection rules for bound-bound rovibronic transitions, allowing finite probabilities for $|\Delta J|>1$ and $|\Delta K|>1$ transitions. However, these higher $|\Delta J|$ and $|\Delta K|$ transitions are expected be less probable than those for $|\Delta J| \leq 1$ and $|\Delta K| \leq 1$. Experimentally, ΔJ up to ± 4 has been invoked to fit the N2P-PFI-PE spectrum for CH_3S.[17]

Similar to the fitting procedure used previously, the intensity for a rotational transition from a (J″, K″) level [$I_{PE}(J'', K'')$] within a given rotational branch is assumed to be proportional to the rotational population of the neutral molecule according to Eq. (10).

$$I_{PE}(J'', K'') \propto r_B(2J'' + 1)\exp[-\Delta E_{rot}''/kT_{rot}] \quad (10)$$

Here, T_{rot} is the rotational temperature of CH_3SH (CH_3CH_2SH), $\Delta E_{rot}''$ is the rotational energy measured with respect to the ground rovibronic state of CH_3SH (CH_3CH_2SH), and r_B is a scaling parameter for a given rotational branch, which is adjusted to obtain the best fit to the experimental spectrum. The transition probabilities from different $|J'', K''\rangle$ levels within each rotational branches are assumed to be equal.

Figure 1(b) shows the simulated spectrum for CH_3SH obtained using a T_{rot} value of 20 K and a Gaussian linewidth of 2 cm^{-1} (FWHM). The simulated spectrum for CH_3CH_2SH plotted in Fig, 2(b) is obtained using a T_{rot} value of 15 K and a Gaussian linewidth of 1 cm^{-1} (FWHM). In Figs. 1(b) and 2(b), we also show the contributions by various rotational branches: ($\Delta J = 0$; $\Delta K = 0, \pm 1$) (dashed curve), ($\Delta J = \pm 1$; $\Delta K = 0, \pm 1$) (dash-dotted curve) and [($\Delta J = 0, \pm 1$; $\Delta K = \pm 2$) plus ($\Delta J = \pm 2$; $\Delta K = 0, \pm 1, \pm 2$)] (dotted curve). In both CH_3SH and CH_3CH_2SH, the sharp spike at the center of the 0-0 PFI-PE vibrational band is identified as the $\Delta J = 0$ and $\Delta K = 0$ branch. The $\Delta J = -1$ (P) and $\Delta J = +1$ (R) branches contribute to the broader structures to the left and right of the center peak, respectively. The contributions from the $\Delta J = \pm 2$ and $\Delta K = \pm 2$ branches have the effect of further broadening the vibrational band and provides a more satisfactory fit to the experimental spectrum. Since adding contributions from higher ΔJ rotational branches yields little improvement to the fits, we conclude that the

rotational branches corresponding to $|\Delta J| \geq 3$ transitions are not important in the photoionization of CH_3SH and CH_3CH_2SH.

The identification of central peak to be the $\Delta J = 0$ and $\Delta K = 0$ rotational branch of the 0-0 PFI-PE vibrational bands for CH_3SH^+ ($CH_3CH_2SH^+$) allows a more accurate determination of the IE for CH_3SH (CH_3CH_2SH). Since the FWHM's of the central peaks associated with the $\Delta J = 0$ and $\Delta K = 0$ branches are 2.9 cm^{-1}, we have assigned uncertainties of ± 2.9 cm^{-1} for the IE values. The IEs for CH_3SH (76256.3±2.9 cm^{-1}) and *gauche*-CH_3CH_2SH (74948.7±2.9 cm^{-1}) determined here are in agreement with results [IE(CH_3SH) = 76 262 ± 5 cm^{-1} and IE(CH_3CH_2SH) = 74 951 ± 5 cm^{-1}] of the N2P-PFI-PE study,[17] which assumes that the peak positions of the 0-0 vibrational bands is close to the IEs of CH_3SH and CH_3CH_2SH. We note that the latter assumption is not always valid, e.g., the 0-0 PFI-PE vibrational bands for CH_3SCH_3 consists of a split peak.[25] Thus, a simulation as described above is essential to obtain a more accurate IE value when the resolution used is insufficient to fully resolve rotational structures in the PFI-PE or TPE spectrum of a polyatomic molecule or radical.

In an accurate theoretical treatment, the actual individual rotational line strengths depend on the electronic matrix elements that couple the initial neutral states to the cation plus photoelectron states. The angular momentum ℓ carried away by the photoelectron must be balanced by the rotational angular momentum change of the ion core. In this respect, photoionization can be viewed as a scattering process. The semi-empirical treatment described here is consistent with the angular momentum balance requirement between the photoelectron and the ion core. The main assumption of the semi-empirical scheme is that the line strengths

for rotational transitions of a given rotational branch are identical and are measured by the scaling parameter r_B. We note that the semi-empirical fits to the experimental spectra obtained here may not be unique.

IV. CONCLUSION

Fine structures due to rotational branch contours are observed in the 0-0 vibrational VUV-PFI-PE bands for CH_3SH^+ and $CH_3CH_2SH^+$. The semi-empirical simulation of these 0-0 vibrational bands has yielded more accurate IE of 76 256.3 ± 2.9 and 74 948.7 ± 2.9 cm^{-1} for CH_3SH and CH_3CH_2SH, respectively. Furthermore, the simulation shows that contributions from rotational branches corresponding to $|\Delta J| \geq 3$ are not important in the photoionization of CH_3SH and CH_3CH_2SH.

ACKNOWLEDGEMENTS

This work was supported by the Director, Office of Energy Research, Office of Basic Energy Sciences, Chemical Science Division of the U.S. Department of Energy under Contract No. W-7405-Eng-82 for the Ames Laboratory. YSC was the recipient of the Henry Gilman Fellowship and the Nelson Chemistry Scholarship for 1996-1997.

REFERENCES

[1] S. G. Lias, J. E. Bartmess, J. F. Liebman, L. Holmes, R. D. Levin, and W. G. Mallard, J. Phys. Chem. Ref. Data 17, Suppl. No. 1 (1988).

[2] H. M. Rosenstock, M. K. Draxl, B. W. Steiner, and J. T. Herron, J. Phys. Ref. Data 6, Suppl. 1 (1977), p. 1.

[3] J. Berkowitz and B. Ruscic, in *Vacuum Ultraviolet Photoionization and Photodissociation of Molecules and Clusters*, edited by C. Y. Ng (World Scientific, Singapore, 1991), p.1.

[4] D. W. Turner, C. Baker, A. D. Baker, C. R. Brundle, *Molecular Photoelectron Spectroscopy* (Wiley, London, 1970).

[5] J. W. Rabalais, *Principle of Ultraviolet Photoelectron Spectroscopy* (Wiley, New York, 1977).

[6] K. Kimura, S. Katsumata, Y. Achibi, T. Yamazaki, and S. Iwata, *Handbook of HeI Photoelectron Spectra of Fundamental Organic Molecules*, (Halsted, Toyko/New York, 1981).

[7] C. Y. Ng, in *Vacuum Ultraviolet Photoionization and Photodissociation of Molecules and Clusters*, edited by C. Y. Ng (World Scientific, Singapore, 1991), p. 169.

[8] K. Raghavachar, B. B. Stefanov, L. A. Curtiss, J. Chem. Phys. **106**, 6764 (1997) and references therein.

[9] C. Y. Ng, in *The Struture, Energetics, and Dynamics of Organic Ions*, edited by T. Baer, C. Y. Ng, and I. Powis, Wiley Series in Ion Chem. and Phys. (Wiley, Chichester, 1996), pp. 35-124; C. Y. Ng, in Adv. Photochem. **22**, 1 (1997).

[10] *High Resolution Laser Photoionization and Photoelectron Studies*, edited by I. Powis, T. Baer, and C. Y. Ng, Wiley Series in Ion Chem. and Phys. (Wiley, Chichester, 1995), and references therein.

[11] E. W. Schlag, *ZEKE Spectroscopy* (Cambridge University Press, Cambridge, 1996).

[12] J. W. Hepburn, in *Vacuum Ultraviolet Photoionization and Photodissociation of Molecules and Clusters*, edited by C. Y. Ng (World Scientific, Singapore, 1991), p. 435; J. W. Hepburn, in *Laser Techniques in Chemistry*, edited by A. Meyers and T. R. Rizzo (Wiley, New York, 1994).

[13] A. H. Kung and Y. T. Lee, in *Vacuum Ultraviolet Photoionization and Photodissociation of Molecules and Clusters*, edited by C. Y. Ng (World Scientific, Singapore, 1991), p. 487.

[14] C.-W. Hsu, M. Evans, P. Heimann, K. T. Lu, and C. Y. Ng, J. Chem. Phys. **105**, 3950 (1996); C.-W. Hsu, M. Evans, C. Y. Ng, and P. Heimann, Rev. Sci. Instrum. **68**, 1694 (1997); P. Heimann, M. Koike, C.-W. Hsu, M. Evans, K. T. Lu, C. Y. Ng, A. Suits, and Y. T. Lee, *ibid.* **68**, 1945 (1997); C.-W. Hsu, M. Evans, S. Stimson, C. Y. Ng, and P. Heimann, J. Chem. Phys. **106**, 8931 (1997).

[15] K. Müller-Dethlefs, M. Sander, and E. W. Schlag, Z. Naturforsch. A **39A**, 1089 (1984); K. Müller-Dethlefs and E. W. Schlag, Ann. Rev. Phys. Chem. **42**, 109 (1991).

[16] An up-to-date reference list for PFI-PE studies of molecules and radicals can be found in the ZEKE Webpage (http://eos.phys.chemie.tu-muenchen.de/zeke).

[17] Y.-S. Cheung, C.-W. Hsu, C. Y. Ng, W.-K. Li, and S.-W. Chiu, Int. J. Mass Spectrom. Ion Processes **159**, 13 (1996).

[18] C.-W. Hsu and C. Y. Ng, J. Chem. Phys. **101**, 5596 (1994).

[19] J.-C. Huang, Y.-S. Cheung, M. Evans, C.-X. Liao, C. Y. Ng, C.-W. Hsu, P. Heimann, H. Lefebvre-Brion, and C. Cossart-Magos, J. Chem. Phys. **106**, 864 (1997).

[20] I. Fischer, A. Lochschmidt, A. Strobel, G. Niedner-Schatteburg, K. Müller-Dethefs, and V. E. Bondybey, Chem. Phys. Lett. **202**, 542 (1993).

[21] Y.-J. Chen and C. Y. Ng, unpublished results.

[22] Gaussian 94, Revision B.2, M. J. Frisch, G. W. Trucks, H. B. Schlegel, P. M. W. Gill, B. G. Johnson, M. A. Robb, J. R. Cheeseman, T. Keith, G. A. Petersson, J. A. Montgomery, K. Raghavachari, M. A. Al-Laham, V. G. Zakrzewski, J. V. Ortiz, J. B. Foresman, C. Y. Peng, P. Y. Ayala, W. Chen, M. W. Wong, J. L. Andres, E. S. Replogle, R. Gomperts, R. L. Martin, D. J. Fox, J. S. Binkley, D. J. Defrees, J. Baker, J. P. Stewart, M. Head-Gordon, C. Gonzalez, and J. A. Pople, Gaussian, Inc., Pittsburgh PA, 1995.

[23] P. F. Bernath, "Spectra of Atoms and Molecules", (Oxford Univ. Press, Oxford, 1995), p. 187-194.

[24] H. D. Cohen and U. Fano, Phys. Rev. **150**, 30 (1966).

[25] Y.-S. Cheung, C.-W. Hsu, and C. Y. Ng, (unpublished).

CHAPTER 6. VACUUM ULTRAVIOLET SINGLE PHOTON AND ULTRAVIOLET NON-RESONANT TWO-PHOTON PULSED FIELD IONIZATION PHOTOELECTRON STUDY OF CH_3SCH_3

A paper accepted for publication in the International Journal of Mass Spectrometry

Y.-S. Cheung and C. Y. Ng

Abstract

The vacuum ultraviolet (VUV) single-photon and ultraviolet non-resonant two-photon (N2P) pulsed field ionization photoelectron (PFI-PE) spectra for CH_3SCH_3 have been obtained in the energy range of 69 500-72 500 cm^{-1}. Vibrational structures observed in the VUV-PFI-PE and N2P-PFI-PE spectra are similar. Guided by the *ab initio* theoretical harmonic frequencies, we have assigned the vibrational bands resolved in these spectra. Using a semi-empirical simulation scheme, together with *ab initio* theoretical rotational constants for CH_3SCH_3 and $CH_3SCH_3^+$, we have also obtained a good fit to the contours of rotational branches resolved in the origin band of the VUV-PFI-PE spectrum. Taking into account the uncertainty of the simulation model used, we obtain a value of 70 097.3 ± 2.0 cm^{-1} (8.69096 ± 0.00016 eV) for the adiabatic ionization energy of CH_3SCH_3.

1. Introduction

Accurate ionization energies (IE's) for molecular species, which are used for prediction of chemical reactivity, are of fundamental importance to chemists [1,2]. The IE of a gaseous molecule can be determined routinely in a photoionization [2] or a photoelectron [3,4] experiment. Ionization energy determinations made in conventional photoionization and

photoelectron studies have uncertainties in the range of 3-100 meV (25-250 cm^{-1}). The accuracy of adiabatic IE values measured for polyatomic molecules is especially poor because of the difficulty in assessing the hot band and kinetic shift effects [2]. The fact that the geometries for a neutral polyatomic molecule and its cation are usually different often makes photoionization yields very low near the ionization threshold. The combination of these effects may prevent the observation of the ionization step in the photoionization efficiency (PIE) spectrum of a polyatomic molecule, and thus results in a large uncertainty in the experimental IE value [5]. Recent advances in *ab initio* quantum computation procedures [6,7], such as the GAUSSIAN-2 (G2) type theories [6] and density functional [8] theoretical methods, have shown to provide IE predictions for small polyatomic molecules and radicals of main group elements to an accuracy of <0.15 eV, approaching that achievable in conventional photoionization and photoelectron experiments. This theoretical achievement has set a challenge for experimental IE measurements to be made with higher accuracy.

In the past decade, the most exciting development in the field of photoionization and photoelectron spectroscopy has been the availability of high resolution, tunable ultraviolet (UV) and vacuum ultraviolet (VUV) laser sources [9-11]. For probing electronic structures of cations, photoelectron spectroscopic measurements are preferred over PIE studies. The laser pulsed field ionization photoelectron (PFI-PE) scheme is the current state-of-the-art photoelectron spectroscopic technique and is capable of providing photoelectron energy resolution close to the optical resolution [12-14]. For specific molecular species with IE values below 12 eV, the non-resonant two-photon (N2P) PFI-PE scheme involving the use of a UV laser is an attractive method for high resolution photoelectron measurements [15,16]. Without

doubt, the single-photon PFI-PE technique is the most versatile high-resolution photoelectron spectroscopic method. In the current technical level, VUV laser radiation with usable intensities can be generated at energies up to ≈17.7 eV by nonlinear optical mixing using commercial dye lasers [9]. Most recently, a synchrotron based VUV-PFI-PE technique has also been demonstrated using monochromatized third-generation undulator synchrotron radiation at the photon energy range of 8-27 eV.[17,18] The PFI-PE resolutions achieved in synchrotron, UV laser and VUV laser based measurements are similar. For specific diatomics, triatomics and simple hydrides, N2P-PFI-PE and VUV-PFI-PE measurements have provided IE values with uncertainties less than a few cm^{-1} [12,19]. This accuracy represents a 10 to 100 fold improvement over those achieved in conventional photoionization and photoelectron measurements. In principle, the analysis of a truly rotational resolved photoelectron spectrum of a molecule is expected to yield the definitive IE value.

Despite of this impressive experimental progress in high-resolution photoelectron spectroscopy, the photoelectron energy resolutions [>0.2 cm^{-1}, full-width at half maximum (FWHM)] obtainable in laser or synchrotron based PFI-PE measurements are still not sufficient to resolve rotational transitions in photoelectron spectra of polyatomic molecules. Thus, PFI-PE studies of polyatomic species reported today mostly provide vibrational information for the corresponding cations [12]. In recent VUV-PFI-PE and N2P-PFI-PE studies of CH_3SH and CH_3CH_2SH, we find that the full-width-at-half-maximum (FWHM) for individual vibrational bands are in the range of 15-25 cm^{-1} for supersonically cooled CH_3SH and CH_3CH_2SH samples at rotational temperatures of 20-30 K [20,21]. These experiments also show that the resolution achieved in the VUV-PFI-PE measurement is better than that in the N2P-PFI-PE study

performed under similar experimental conditions [21]. Fine structures arising from contours of rotational branches are resolved in the origin bands of the VUV-PFI-PE spectra for CH_3SH and CH_3CH_2SH. The simulation of these fine structures has provided accurate IE values for CH_3SH and CH_3CH_2SH with uncertainties of ± 2.9 cm^{-1} [21].

Here, we present the results of an N2P-PFI-PE and VUV-PFI-PE study of CH_3SCH_3. As in previous studies [20,21], *ab initio* predictions for vibrational and rotational constants of CH_3SCH_3 and $CH_3SCH_3^+$ are used to assist the assignment and simulation of the PFI-PE spectra. Theoretical predictions obtained using standard *ab initio* program packages [22] for vibrational and rotational constants for small polyatomic species are known to have an accuracy of 10-20%. This experiment, together with previous studies [20,21,23], suggests that with an achievable instrumental resolution of ≈ 0.5-1.0 cm^{-1}, it is advantageous to perform PFI-PE measurements of polyatomic molecules at higher rotational temperatures. The rotational contours resolved in a rotationally hot spectrum contain more information about the rotational structures of the neutral and cationic species as compared to that observed in a rotationally cooled spectrum.

2. Experimental and *ab initio* calculations

The experimental apparatus and procedures used are similar to those described previously [20,21,23-25]. The apparatus consists of a tunable UV or VUV laser source, a pulsed molecular beam source, an ion time-of-flight (TOF) mass spectrometer and an electron detector for PFI-PE detection.

2.1. VUV-PFI-PE and VUV-PIE measurements

The VUV laser system has been described previously in detail [21,25]. Briefly, it comprises of one excimer laser (Lambda Physik EMG201), two dye lasers (Lambda Physik FL3002) and a Xe gas cell for nonlinear optical mixing. The XeCl excimer laser output (308 nm, 200-250 mJ) was split to pump the two dye lasers. For the present study on CH_3SCH_3, the photon energy range of interest is 69 900-71 500 cm^{-1}. The UV frequency ω_1 was generated using coumarin-450 dye in one of the dye lasers followed by frequency doubling with a BBOI crystal. Here, UV frequency was fixed at $2\omega_1$ = 89 860.6 cm^{-1}, corresponding to the two-photon resonance of the Xe 5p $\rightarrow$ 6p transition. The other dye laser is tuned in the visible frequency (ω_2) range of 18 200-20 800 cm^{-1}, which was generated using Coumarin-500 dye. The visible laser beam is merged with the UV laser beam by a dichromic mirror. Both beams were then focused into the Xe gas cell (pressure $\approx$ 21 Torr) by a focusing lens (focal length = 15 cm). The VUV frequencies (ω_{VUV}) were produced by the four-wave difference frequency ($\omega_{VUV} = 2\omega_1 - \omega_2$) mixing in the Xe gas cell. The gas cell has a quartz entrance window and a MgF_2 exit window, which serves to isolate the gas cell from the photoexcitation/photoionization (PEX/PI) chamber. With a transmission cut-off wavelength of $\approx$115 nm, the MgF_2 window allows the VUV different frequencies to transmit while absorbing the VUV sum frequencies.

A photoelectric detector made out of Cu was used to measure the VUV laser photon intensities. In addition to monitoring the VUV light intensities, the photoelectric detector also served as a light trap for ω_1, ω_2 and ω_{VUV}. However, by blocking the visible laser beam, we found that $\approx$90 % of the photoelectric current is contributed by the UV laser (ω_2) beam.

Fortunately, this background is nearly constant because the UV frequency is fixed. We found that the intensity of the VUV difference frequency is also nearly constant over the VUV range of interest here. The VUV-PFI-PE intensities presented here were not normalized by the corresponding VUV light intensities.

To calibrate the laser frequencies, a small fraction of the dye laser (ω_2) output was directed into a uranium hollow cathode lamp with Ne as the buffer gas. The Ne absorption spectrum recorded simultaneously during the experiment provided accurate energy calibration of the PFI-PE spectra. The bandwidth of the dye laser is 0.2 cm^{-1} for the fundamental and ≈0.4 cm^{-1} for the second harmonic output. For a two-photon excitation, the resolution is ≈0.8 cm^{-1}. Thus, the resolution for the VUV laser radiation is estimated to be ≤1 cm^{-1}. The accuracy of photon frequency calibration is expected to be ±0.2 cm^{-1}.

The photoelectron-photoion apparatus [20,21,23,24] used in this study consists of a pulsed molecular beam production system, an ion time-of-flight (TOF) mass spectrometer and an electron detector for PFI-PE detection. The molecular beam source chamber was pumped by a freon-trapped, 6-in. diffusion pump (pumping speed ≈2000 L/s), while the photoionization chamber and the ion TOF tube were evacuated by turbomolecular pumps with pumping speeds of 250 L/s and 50 L/s, respectively. During the experiment, the beam source chamber and the photoionization chamber were maintained at pressures of ≈ 5×10^{-5} and ≈ 5×10^{-7} Torr, respectively.

Ion detection using the ion TOF mass spectrometer has been described previously [23,24]. In this study, a constant electric field at 42 and 167 V/cm was used to extract ions

formed in the PEX/PI region. The PFI-PE detection scheme relies on delayed PFI of long-lived high-*n* Rydberg states populated by laser excitation at a few wave numbers below the ionization threshold [12-14]. In the present experiment, the firing of the excitation laser was delayed by 580 μs with respect to the triggering pulse for opening the pulsed valve. After a typical delay of 2.5 μs with respect to firing of the VUV laser, a forward biased pulsed electric field of 0.24 V/cm and 1-μs duration was used to field ionize the high-*n* Rydberg species as well as to extract the electrons to the micro-channel plate detector. Using this PFI-PE detection scheme, we expect to achieve a resolution of 1.0-1.5 cm^{-1} (FWHM).

Two digital delay units (Stanford Research DG535) control the operating sequence of the pulsed valve, dye laser and pulsed electric field. The signals from the electron detector (or ion detector) and the photoelectric VUV detector were fed into two identical boxcar integrators (Stanford Research SR250), which were interfaced to an IBM/PC computer.

In this experiment, the CH_3SCH_3 molecular beam was produced by seeding the CH_3SCH_3 vapor (≈430 Torr) at ≈20 °C in 640 Torr of Ar and then expanding the mixture through the nozzle (diameter = 50 μm) of a pulsed valve. The CH_3SCH_3 sample (>99% purity) was obtained from Aldrich and used without further purification. The molecular beam is skimmed by a conical skimmer (1-mm diameter, 3.8 cm from the nozzle) before intersecting with the VUV laser beam at 90° and 8.3 cm downstream from the skimmer.

2.2. N2P-PFI-PE measurements

The experimental setup and conditions in the N2P-PFI-PE study [20,23,24] were the same as those in the VUV-PFI-PE study as described above except that only one UV dye laser was used for excitation. Rhodamine-560 dye was used to produce visible light in the range of

17 400-18 100 cm^{-1} (552-575 nm). The second harmonic radiation in the UV range of 34 800-36 200 cm^{-1} was generated using a BBOI crystal. The UV laser radiation thus formed was focused into the PEX/PI region with a 200 mm fused-silica focusing lens (focal length = 200 mm).

2.3. *Ab initio* calculations

Ab initio calculations were performed on CH_3SCH_3 and $CH_3SCH_3^+$ with the GAUSSIAN 94 for Windows installed at a Pentium-166 PC [22]. The G2 energies for CH_3SCH_3 and $CH_3SCH_3^+$ were calculated to obtain the adiabatic IE for CH_3SCH_3. The detail of the G2 procedure has been described previously [6]. The harmonic vibrational frequencies of $CH_3SCH_3^+$ at the MP2/6-31G(d) level were scaled [26] by 0.92 and are employed for the assignment of the vibrational structures obtained in the PFI-PE spectra.

The theoretical geometries of CH_3SCH_3 and $CH_3SCH_3^+$ were calculated at the MP2/6-31(d) level for calculation of their rotational constants. The calculated rotational constants for CH_3SCH_3 (A″, B″, C″) and $CH_3SCH_3^+$ (A^+, B^+, C^+) are listed in Table I. At the MP2/6-31G(d) level of theory, both the geometries for both CH_3SCH_3 and $CH_3SCH_3^+$ are predicted to have the C_{2v} symmetry. The structural parameters [equilibrium bond distances (r), bond angles (∠) and dihedral angles (φ)] for CH_3SCH_3 and $CH_3SCH_3^+$ are summarized in Table I. The H^α and H^β represent hydrogen atoms lying in and out of the C-S-C plane, respectively, in CH_3SCH_3 and $CH_3SCH_3^+$. The differences of the theoretical bond lengths [r(C-S), $r(C-H^\alpha)$ and $r(C-H^\beta)$], bond angles [∠C-S-C, $\angle S-C-H^\alpha$ and $\angle S-C-H^\beta$] and dihedral angles [$\varphi(C-S-C-H^\alpha)$ and $\varphi(C-S-C-H^\beta)$] for CH_3SCH_3 and $CH_3SCH_3^+$ are also calculated in Table I.

Table I. Calculated rotational constants (A''/A^+, B''/B^+ and C''/C^+), bond lengths (r), bond angles ($\angle$) and dihedral angles (φ) for $CH_3SCH_3/CH_3SCH_3^+$ obtained at the MP2/6-31G(d) level of theory.

	CH_3SCH_3	$CH_3SCH_3^+$	Δ (Ion - Neutral)[a]
Rotational constants[b] (cm^{-1})			
A'' or A^+ (cm^{-1})	0.589	0.639	---
B'' or B^+ (cm^{-1})	0.256	0.249	---
C'' or C^+ (cm^{-1})	0.191	0.192	---
Bond lengths[c] (Å)			
r(C-S)	1.804	1.784	-0.020
r(C-H^α)	1.091	1.090	-0.001
r(C-H^β)	1.092	1.095	+0.003
Bond angles[c] (deg.)			
∠C-S-C	98.5	102.5	+4.0
∠S-C-H^α	107.7	108.2	+0.5
∠S-C-H^β	111.3	109.3	-2.0
Dihedral angles[c] (deg.)			
φ(C-S-C-H^α)	180.0	180.0	0.0
φ(C-S-C-H^β)	61.1	59.8	-1.3

[a] Difference of the bond parameter predicted for $CH_3SCH_3^+$ and CH_3SCH_3.

[b] The b-axis is the C_2 symmetry axis bisecting ∠C-S-C; the a-axis is perpendicular to the b-axis and lies in the C-S-C plane; and the c-axis is perpendicular to the C-S-C plane.

[c] Both CH_3SCH_3 and $CH_3SCH_3^+$ belong to the C_{2v} point group. Here H^α and H^β are hydrogen atoms lying on and out of the C-S-C plane, respectively.

3. Results and discussion

3.1. Photoionization efficiency spectrum for CH_3SCH_3

The adiabatic IE of CH_3SCH_3 has been measured to be 8.685 ± 0.005 eV (70 049 ± 40 cm^{-1}) [27] by Watanabe *et al.* and 8.69±0.01 eV (70 090 ± 81 cm^{-1}) [28] by Akopyan *et al.* in previous PIE studies. The G2 calculation of the present study gives an IE(CH_3SCH_3) value of 8.71 eV (70251 cm^{-1}) and is in good agreement with these PIE measurements. Similar to the N2P ionization study of CH_3CH_2SH, efforts to measure the N2P-PIE spectrum for CH_3SCH_3 were not successful. As pointed out previously [20,21], the N2P ionization requires the laser to be focused at the PEX/PI region. Thus, parent $CH_3SCH_3^+$ ions initially formed by the N2P ionization may absorb an additional photon within the same laser pulse and result in further dissociation. The VUV-PIE spectrum for CH_3SCH_3 obtained using a dc electric fields (F) of 42 V/cm at the PEX/PI region is shown in Fig. 1(a). The VUV-PIE spectrum obtained using a higher dc electric field of F = 167 V/cm is depicted in Fig. 1(b). The sharp ionization onsets observed in the PIE spectra indicate that the Franck-Condon factor for the ionization transition is favorable. Since the ionization of CH_3SCH_3 involves the removal of a nonbonding electron localized at the S atom, the geometries for CH_3SCH_3 and $CH_3SCH_3^+$ are expected to be similar. Assuming that the IE is determined by the mid-point of the rapidly rising ionization onset in the PIE spectrum, we obtained IE(CH_3SCH_3) values of 70 032 ± 12 cm^{-1} and 70 060 ± 12 cm^{-1} for F = 167 and 42 V/cm, respectively. The lower IE value observed for F = 167 V/cm than that for F = 42 V/cm is due to the Stark shift effect. By linear extrapolation, the IE at zero electric field is determined to be 70 088 ± 12 cm^{-1}.

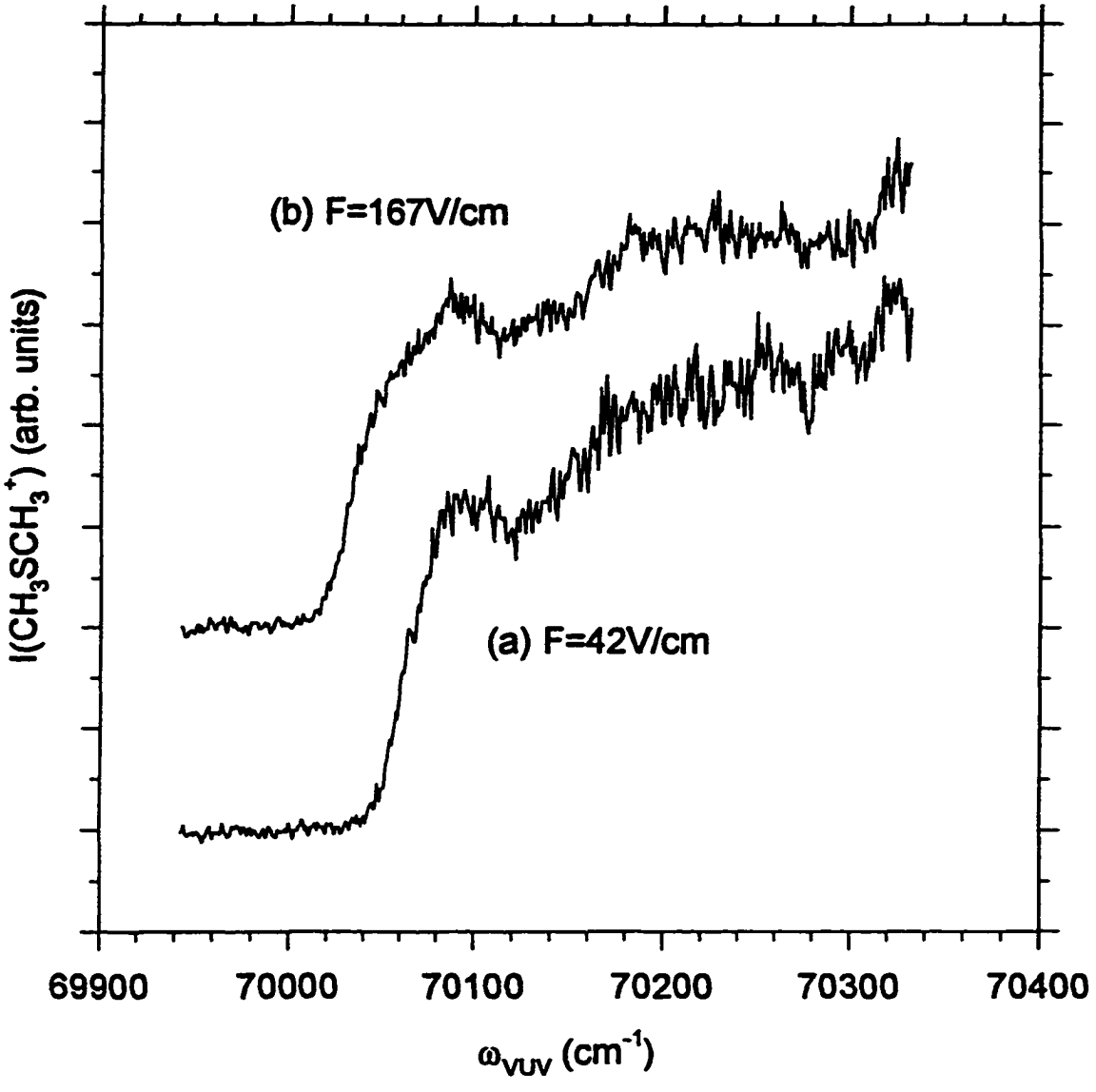

Fig. 1. VUV-PIE spectrum of CH_3SCH_3 in the photon energy range of 69 940-70 330 cm^{-1} recorded using a dc electric field of (a) 42 V/cm and (b) 167 V/cm.

3.2. Comparison and assignment of the VUV-PFI-PE and N2P-PFI-PE spectra for CH_3SCH_3

In both the VUV and N2P experiments, we have measured the PFI-PE spectrum of CH_3SCH_3 covering the energy region of 69 500-72 500 cm^{-1}. The VUV-PFI-PE and N2P-PFI-PE spectra in the energy region of 70 000-71 600 cm^{-1} are plotted in Figs. 2(a) and 2(b), respectively. The spectra of Figs. 2(a) and 2(b) represent the average of more than two independent scans. The signal-to-noise ratio obtained for the N2P-PFI-PE spectrum is better than that for the VUV-PFI-PE spectrum. Taking into account the experimental uncertainties, we conclude that the vibrational bands and their relative intensities observed in the two spectra are nearly identical. The major peaks at 70 094 cm^{-1} observed in Figs. 2(a) and 2(b) have FWHM's of ≈20 cm^{-1} and are assigned as the origin band, corresponding to the ionization transition CH_3SCH_3 ($\tilde{X}\,^1A_1$; $\nu_i = 0$) → $CH_3SCH_3^+$($\tilde{X}\,^2B_1$; $\nu_i^+ = 0$) + e^-. The overwhelmingly high intensity for the origin band is consistent with the prominent ionizing step-like onset observed in the PIE spectrum of Fig. 1. The widths of the vibrational PFI-PE bands resolved in Figs. 2(a) and 2(b) can be attributed to finite rotational excitation of the CH_3SCH_3 sample. As shown in the spectral simulation below (section III.C), the rotational temperature for CH_3SCH_3 achieved in the pulsed supersonic expansion is ≈30 K.

In our recent PFI-PE study of CH_3CH_2SH [20], we suggested that the comparison of corresponding theoretical structural parameters, such as bond lengths, bond angles and dihedral angles, for the neutral and cation is useful in revealing the excitation vibrational modes of the cation. As shown in Table I, the change in r(C-S) is significantly greater than those for $r(C\text{-}H^{\alpha})$ and $r(C\text{-}H^{\beta})$ upon ionization of CH_3SCH_3. This observation indicates that the C-S stretching

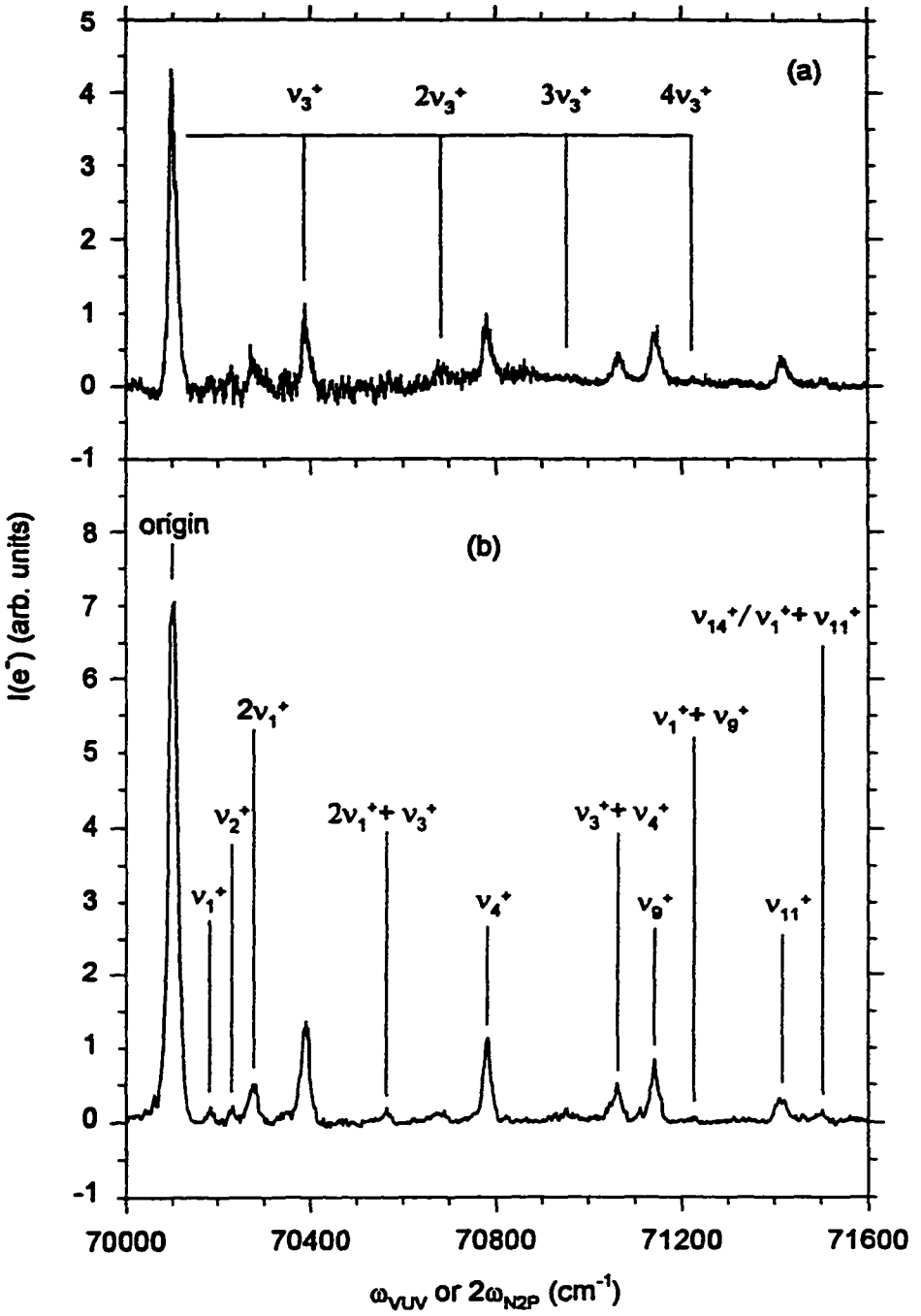

Fig. 2. VUV-PFI-PE spectrum (a) and N2P-PFI-PE spectrum (b) of CH_3SCH_3 in the photon energy range of 70 000-71 600 cm^{-1}. The observed ν_3^+ (symmetric C-S-C bending) vibrational progression for $CH_3SCH_3^+$ is marked in (a). Other assignments of $CH_3SCH_3^+$ vibrational bands are marked in (b). Also see Table 2 for the assignments.

mode is excited in $CH_3SCH_3^+$. Similarly, since finite changes are predicted for ∠C-S-C, ∠S-C-H^β and φ(C-S-C-H^β) upon ionization of CH_3SCH_3, we expect that the C-S-C bending, S-C-H^β bending and torsional modes in $CH_3SCH_3^+$ are also excited. Assuming that the CH_3SCH_3 sample is vibrationally cold, the total vibrational wave function for CH_3SCH_3 in its ground electronic state should be totally symmetric and have the a_1 symmetry. In accord with the Franck-Condon principle, which results from the Born-Oppenheimer approximation, the allowed ionization transitions should give rise to $CH_3SCH_3^+$ vibrational states with a_1 symmetry. Guided by the *ab initio* harmonic frequencies and their symmetries, we have satisfactorily assigned the vibrational bands resolved in the VUV-PFI-PE and N2P-PFI-PE spectra. The comparison between the experimental and theoretical harmonic vibrational frequencies is given in Table II. Here, the energies of the observed vibrational PFI-PE bands are measured with respect to the peak position of the origin band. The assignments of the vibrational bands are also marked in Figs. 2(a) and 2(b).

According to theoretical predictions, the two lowest harmonic frequencies for $CH_3SCH_3^+$ are the asymmetric torsional mode (ν_1^+, predicted frequency = 57 cm^{-1}) and symmetric torsional mode (ν_2^+, predicted frequency = 134 cm^{-1}). The three lowest energy bands observed in the VUV-PFI-PE/N2P-PFI-PE spectra are peaked at 83/86, 130/130 and 175/173 cm^{-1}. If we assign the first peak at 83/86 cm^{-1} to ν_1^+, the third peak at 175/173 cm^{-1} should be assigned to $2\nu_2^+$. The second peak at 130/130 cm^{-1} can be assigned as ν_2^+. Since $2\nu_2^+$ has a_1 symmetry, this assignment accounts for the higher intensity observed for the peak at 175/173 cm^{-1} compared to those of the first and second peaks. We expect that the torsional

Table II. Comparison of experimental and theoretical vibrational frequencies for $CH_3SCH_3^+$.

Assignment[a]	N2P-PFI-PE (cm^{-1})[b,c]	VUV-PFI-PE (cm^{-1})[b,c]	Theoretical[d,e] (cm^{-1})
ν_1^+	83 (w)	86 (w)	57 [asym. torsional (a_2)]
ν_2^+	130 (w)	130 (w)	134 [sym. torsional (b_1)]
$2\nu_1^+$	175 (s)	173 (s)	114
	(166)	(172)	
ν_3^+	291 (s)	290 (s)	276 [C-S-C bending (a_1)]
$2\nu_1^+ + \nu_3^+$	465 (w)	472 (w)	410
	(466)	(463)	
$2\nu_3^+$	577 (w)	578 (w)	$2\nu_3^+ = 552$
	(582)	(580)	
ν_4^+	681 (s)	681 (s)	675 [sym C-S stretch (a_1)]
$3\nu_3^+$	865 (w)	865 (w)	$3\nu_3^+ = 828$
	(873)	(870)	
$\nu_3^+ + \nu_4^+$	963 (s)	967 (s)	951
	(972)	(971)	
ν_9^+	1042 (s)	1042 (s)	1057 [C-H bending (a_1)]
$\nu_1^+ + \nu_9^+$	1131 (w)	1127 (w)	1114
	(1128)	(1125)	
$4\nu_3^+$	(1164)	(1160)	$4\nu_3^+ = 1104$
ν_{11}^+	1312 (s)	1316 (s)	1356 [C-H bending + wagging (a_1)]
ν_{14}^+	1402 (w)	1409 (w)	1416 [C-H bending + scissoring + wagging (a_1)]
$\nu_1^+ + \nu_{11}^+$	(1395)	(1402)	1413

[a] See the text. The frequencies for ν_n^+ are arranged in the increasing order as a function of *n*.

[b] We denote "s" and "w" as strong and weak intensities, respectively

[c] The frequencies given in parentheses are estimated energy positions based on experimental observations. For $2\nu_2^+$ and n ν_3^+, the estimated values have not taken into corrections due to anharmonicities.

[d] Calculated frequencies at the MP2/6-31G(d) level of theory. The theoretical values have been scaled by 0.92.

[e] The σ-plane perpendicular to the C-S-C plane is taken as the σ_v in the symmetry labels.

potentials for CH_3SCH_3 and $CH_3SCH_3^+$ are highly anharmonic. As shown in the VUV-PFI-PE/N2P-PFI-PE study of CH_3CH_2SH [20], more accurate predictions for ionization transitions associated with the $CH_3SCH_3/CH_3SCH_3^+$ torsional modes will require the consideration of transitions between transitions of energy levels supported by the torsional potential for CH_3SCH_3 and those for $CH_3SCH_3^+$.

All other vibrational bands observed at higher energies can be assigned to $CH_3SCH_3^+$ vibrational modes with a_1 symmetry. The three strong vibrational bands observed in the VUV-PFI-PE/N2P-PFI-PE spectra at 290/291, 681/681 and 1042/1042 cm^{-1} can be assigned with confidence to the ν_3^+ (symmetric C-S-C bending mode), ν_4^+ (symmetric C-S stretching mode) and ν_9^+ (symmetric C-H bending mode) for $CH_3SCH_3^+$. These modes are of a_1 symmetry and have the respective scaled MP2/6-31G(d) harmonic frequencies of 276, 675 and 1057 cm^{-1}. The weak structures at 578/577, 865/865 and 1127/1131 cm^{-1} are assigned as $2\nu_4^+$, $3\nu_4^+$ and $4\nu_4^+$, respectively, belonging to members of the ν_4^+ vibrational progression. The weak band at 1127/1131 cm^{-1} may also arise from excitation of $\nu_1^+ + \nu_9^+$. The medium peaks observed at 472/465, 967/963 and 1316/1312 cm^{-1} are assigned to $2\nu_1^+ + \nu_4^+$, $\nu_3^+ + \nu_4^+$ and ν_{11}^+ (symmetric C-H bending and wagging mode) of $CH_3SCH_3^+$, respectively. Based on the observed energies for ν_1^+, ν_3^+ and ν_4^+, the $2\nu_1^+ + \nu_3^+$ and $\nu_3^+ + \nu_4^+$ combination bands are expected to be at 463-466 and 971-972 cm^{-1}, respectively. The weak peak at 1409/1402 cm^{-1} can be attributed to ν_{14}^+ (symmetric C-H bending + scissoring + wagging, predicted frequency = 1416 cm^{-1}) and/or $\nu_1^+ + \nu_{11}^+$. The latter combination band is expected to appear at 1399/1398 cm^{-1}. Both the ν_{11}^+ and ν_{14}^+ are of a_1 symmetry. Comparing the theoretical and experimental vibrational frequencies,

we conclude that the scaled MP2/6-31G(d) frequencies are too low for ν_n^+ ($n \leq 4$) and too high for ν_n^+ ($n = 9$, 11 and 14).

3.3. Simulation of the origin VUV-PFI-PE band for $CH_3SCH_3^+$

Figure 3(a) shows an expanded view of the origin band of the VUV-PFI-PE spectrum for CH_3SCH_3 in the energy region of 70 060-70 130 cm^{-1}. This spectrum represents the average of more than five independent scans. The majority of fine structures of Fig. 3(a) are reproducible. The most noticeable feature is the dip in the center of the PFI-PE band. This feature is contrary to the sharp peaks observed in the centers of the VUV-PFI-PE origin bands for CH_3SH and CH_3CH_2SH [21].

Both CH_3SCH_3 and $CH_3SCH_3^+$ are asymmetric top molecules, which are classified by the moment of inertia I_A, I_B and I_C associated with rotation around the a, b and c molecular axes, respectively [29,30]. For CH_3SCH_3 and $CH_3SCH_3^+$, the symmetry axis z bisecting the ∠C-S-C is identical to the b-axis, the molecular a-axis (symmetry axis y) is perpendicular to the b-axis and lies in the C-S-C molecular plane, and the molecular c-axis (symmetry axis x) is perpendicular to the C-S-C molecular plane. The similar theoretical rotational constants obtained for CH_3SCH_3 and $CH_3SCH_3^+$ (see Table I) are consistent with the fact that the neutral and cationic geometries are quite similar. As indicated above, both CH_3SCH_3 and $CH_3SCH_3^+$ belong to the C_{2v} point group. The asymmetry parameters (κ) [defined as $(2B'' - A'' - C'')/(A'' - C'')$ for the neutral and $(2B^+ - A^+ - C^+)/(A^+ - C^+)$ for the ion] are -0.67 for CH_3SCH_3 and -0.74 for $CH_3SCH_3^+$. Since these κ values are close to -1, CH_3SCH_3 and $CH_3SCH_3^+$ are near prolate top molecules.[29,30]

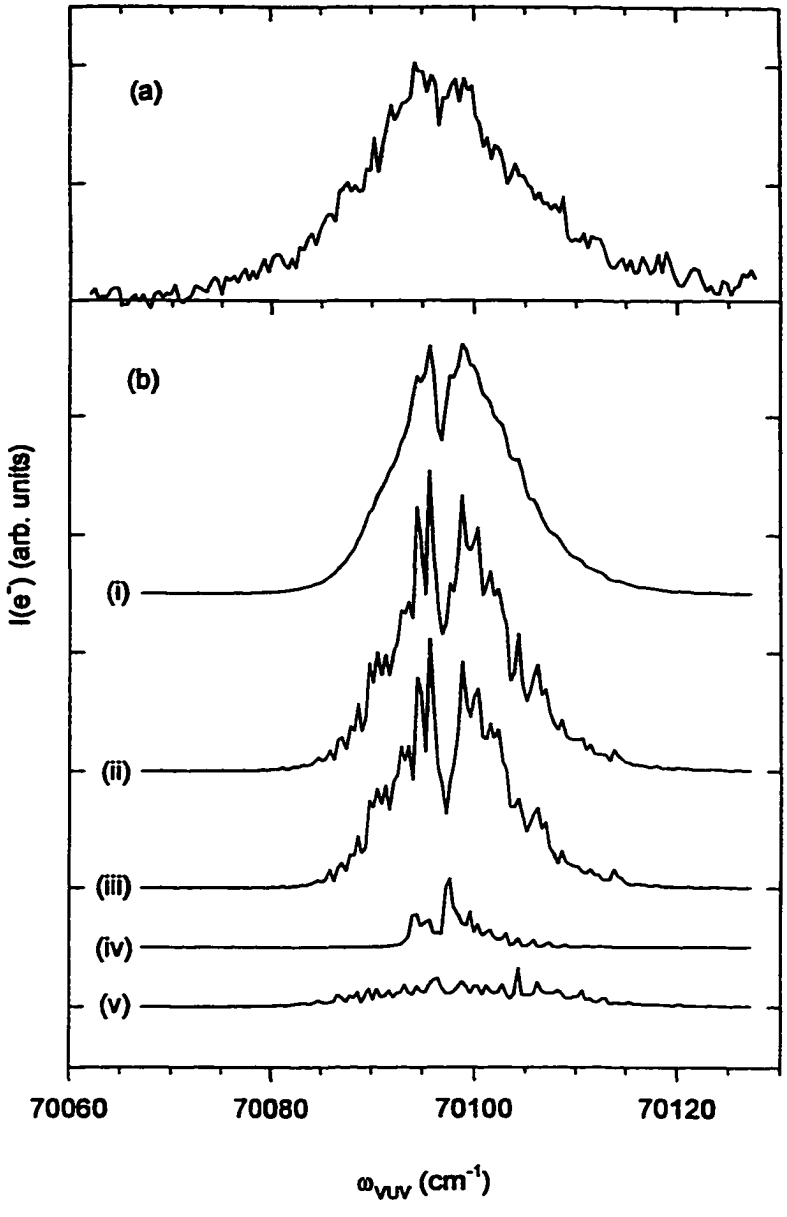

Fig. 3. (a) The origin VUV-PFI-PE band for $CH_3SCH_3^+$ in the energy range of 70 060-70 160 cm^{-1}. (b) Simulated spectra for CH_3SCH_3 obtained by using a rotational temperature of 30 K and a Gaussian width of 0.8 and 0.2 cm^{-1} (FWHM) are marked as curves (i) and (ii), respectively. The respective contributions by the Q branches ($\Delta J = 0$, $\Delta K = 0, \pm 1$) and P plus R branches ($\Delta J = \pm 1$, $\Delta K = 0, \pm 1$) calculated assuming a Gaussian linewidth of 0.2 cm^{-1} (FWHM) are shown as curves (iv) and (iii). The calculated contribution [Gaussian linewidth = 0.2 cm^{-1} (FWHM)] due to rotational branches ($\Delta J = 0, \pm 1$; $\Delta K = \pm 2$) is shown as curve (v). The r_B values used for ($\Delta J = \pm 1$, $\Delta K = 0, \pm 1$) are 5, whereas the r_B values for all other rotational branches are taken to be 1.

We have calculated the rotational energies (E_{rot}) of these asymmetric top molecules by diagonalization of the Hamiltonian matrix using the symmetric top rotational basis set.[29] The asymmetric top energy levels for CH_3SCH_3 and $CH_3SCH_3^+$ are labeled by $J^-_{K_a K_c}$ and $J^+_{K_a^+ K_c^+}$, respectively. Here, J″ and J^+ are good quantum numbers, which represent the respective total angular momentum quantum numbers for the neutral and cation. The project quantum numbers K_a″ (K_a^+) and K_c″ (K_c^+) are good quantum numbers only in the prolate and oblate top limits, respectively. Here , we use the conventional labeling O, P, Q, R and S rotational branches for $\Delta J = N^+ - J'' = -2, -1, 0, +1$ and +2 transitions, respectively.

Depending on the order of the rotational constants and the direction of the transition dipole moment, rotational transitions involving asymmetric top molecules are classified into types-a, -b and -c transitions. The $CH_3SCH_3/CH_3SCH_3^+$ system of interest here is similar to that of the H_2O/H_2O^+, which has been investigated in details [31]. The highest occupied orbital for H_2O (CH_3SCH_3) has the b_1 symmetry and is essentially a p-type atomic orbital pointing out the H-O-H (C-S-C) molecular plane. Thus, the atomic selection rules $\Delta l = \pm 1$ are expected to provide an approximated description of photoionization for these molecules. A*b initio* Schwinger variational calculations on the H_2O/H_2O^+ system indicate dominant kd (l = 2) photoionization continuum, in accord with the atomic model.[32] Calculations based on the multi-channel quantum defect theory (MQDT) show that l = 2 photoionization leads only to type-c rotational transitions, for which the selection rules are ΔK_a = odd; and ΔK_c = even.[33] Rotationally resolved VUV-PFI-PE spectrum for H_2O near its ionization threshold has been reported previously by White and coworkers.[34] Although the strongest transitions can be

assigned to type-c transitions, rotational structures arising from type-c transitions are clearly observed. This observation is attributed to np-nd Rydberg series interactions induced by a finite anisotropy of the H_2O^+ ion core.[35,36] In the MQDT approach, the np-nd mixing could also be induced by a long-range dipolar coupling, which is the manifestation of the anisotropy of the cation potential. The types-a and -c transitions for the H_2O/H_2O^+ system are a general consequence of the parity selection rule for the formation of an l = even (odd) electron. The *ab initio* Schwinger variational study of McKoy and co-workers has shown that for threshold photoionization of H_2O the selection rules are summarized as $\Delta K_a + l$ = odd [36,37]. They show that only type-c (l = even) and type-a (l = odd) photoionization transitions are allowed independent of nuclear symmetry constraints. In view of the similarity between the H_2O/H_2O^+ and $CH_3SCH_3/CH_3SCH_3^+$ systems, we may assume that the threshold photoionization of CH_3SCH_3 also follows types-a and -c transitions. However, our effort to simulate the VUV-PFI-PE spectrum of Fig. 3(a) by assuming types-a and -c transitions was unsuccessful. Since individual rotational transitions are not resolved in the present experiment, this unsuccessful simulation cannot be considered as proof that that the selection rules governing photoionization transitions for the H_2O/H_2O^+ and $CH_3SCH_3/CH_3SCH_3^+$ systems are different.

As shown in Table I, the rotational constants A″ and A^+ are significantly greater than C″ and C^+ indicating that the rotational spacings of CH_3SCH_3 and $CH_3SCH_3^+$ are mostly determined by the A″ and A^+ rotational constants, respectively. In the simulation present below, we have assumed that the photoionization transitions for the $CH_3SCH_3/CH_3SCH_3^+$ are close to the prolate top limit,[29,30] governing by ΔK_a (= ΔK) only.

The intensity for a rotational transition from a neutral level $|\, J'', K_a'', K_\chi''\rangle$ to an ionic state $[I_{PE}(J'', K_a'', K_\chi'')]$ is proportional to the rotational population of the neutral molecule according to the Boltzmann distribution,[21,23]

$$I_{PE}(J'', K_a'', K_\chi'') \propto r_B (2J'' + 1)\exp[-\Delta E_{rot}/(kT_{rot})]. \quad (1)$$

Here, T_{rot} is the rotational temperature of CH_3SCH_3, ΔE_{rot} is the rotational energy measured with respect to the ground rovibronic state of CH_3SCH_3 and r_B is a scaling parameter for a given rotational branch, which is adjusted to obtain the best fit to the experimental spectrum. The main assumption of this semi-empirical scheme is that the transition probabilities from different $|\, J'', K_a'', K_c''\rangle$ levels within a rotational branch are taken to be equal and are measured by the scaling parameter r_B. In an accurate theoretical treatment, the intensity of a rotational transition is proportional to the product of the rotational population and the rotational line strength, which depends on the actual electronic matrix element that couple the initial neutral rotational state to the final cation rotational state plus the photoelectron state.

Curve (i) of Figure 3(b) shows the simulated spectrum for CH_3SCH_3 obtained using a T_{rot} value of 30 K and a Gaussian linewidth of 0.8 cm^{-1} (FWHM). In order to compare the experimental and simulated features, we have also shown the simulated spectrum calculated using a Gaussian linewidth of 0.2 cm^{-1} (FWHM) [see curve (ii)]. The contributions by the Q branches ($\Delta J = 0$; $\Delta K = 0, \pm 1$,) and the P plus R branches ($\Delta J = \pm 1$; $\Delta K = 0, \pm 1$) calculated assuming a Gaussian linewidth of 0.2 cm^{-1} (FWHM) are plotted as curves (iv) and (iii) in Fig. 3(b), respectively. The rotational branches ($\Delta J = 0, \pm 1$; $\Delta K = \pm 2$) calculated using a Gaussian linewidth of 0.2 cm^{-1} (FWHM) are also shown in Fig. 3(b) [see curve (v)]. These $\Delta K = \pm 2$

branches are quite broad. The r_B values used for the rotational branches ($\Delta J = \pm 1$, $\Delta K = 0, \pm 1$) are 5, as compared to the r_B values of 1 for all other rotational branches.

Although the simulated spectrum consisting of the P, Q and R rotational branches captures the main structures observed in the VUV-PFI-PE spectrum of Fig. 3(a), the width of such a simulated spectrum [curve (i) or (ii)] is too narrow compared to the experimental spectrum. We expect that higher rotational branches, i.e., $|\Delta J| > 1$ branches [not shown in Fig. 3(b)], also have minor contributions to the experimental spectrum. The contributions of the $|\Delta J| > 1$ branches should have the effect of broadening the simulated band and thus providing a more satisfactory fit to the experimental spectrum. The most important goal of the simulation is to obtain an accurate value for the adiabatic IE for CH_3SCH_3. Taking into account the uncertainty of the simulation model, the spectral simulation yields a value of 70 097.3 ± 2.0 cm^{-1} (8.69096 ± 0.00016 eV) for the IE of CH_3SCH_3.

4. Conclusion

We have obtained the vibrationally resolved VUV-PFI-PE and N2P-PFI-PE spectra for CH_3SCH_3 near its ionization threshold. Guided by the theoretical harmonic frequencies for $CH_3SCH_3^+$, we have assigned the photoelectron bands to excitations of the torsional (ν_1^+ and ν_2^+), C-S-C bending (ν_3^+), C-S stretching (ν_4^+) and C-H bending (ν_9^+, ν_{11}^+, ν_{14}^+) vibrational modes of $CH_3SCH_3^+$.

Contours of rotational branches are partially resolved in the origin band of the VUV-PFI-PE spectrum. Using the theoretical rotational constants based on the geometries for

CH_3SCH_3 and $CH_3SCH_3^+$ predicted at the MP2/6-31G(d) level, we have calculated the rotational levels of these asymmetric top molecules. On the basis of a semi-empirical simulation, we have obtained an accurate value for the adiabatic IE of CH_3SCH_3.

Acknowledgements

The authors thank Dr. C.-W. Hsu and Dr. J.-C. Huang for their assistance in the early phase of this experiment. This work was supported by the Director, Office of Energy Research, Office of Basic Energy Sciences, Chemical Science Division of the U.S. Department of Energy under Contract No. W-7405-Eng-82 for the Ames Laboratory. YSC was the recipient of the Henry Gilman Fellowship and the Nelson Chemistry Scholarship for 1996-1997.

References

[1] S. G. Lias, J. E. Bartmess, J. F. Liebman, J. L. Holmes, R. D. Levin, W. G. Mallard, J. Phys. Chem. Ref. Data 17 (1988) (Suppl), pp. 40-646.

[2] H. M. Rosenstock, M. K. Draxl, B. W. Steiner, J. T. Herron, J. Phys. Ref. Data 6, (1977) (Suppl).

[3] D. W. Turner, C. Baker, A. D. Baker, C. R. Brundle, Molecular Photoelectron Spectroscopy, Wiley, London, 1970.

[4] K. Kimura, S. Katsumata, Y. Achibi, T. Yamazaki, S. Iwata, Handbook of HeI Photoelectron Spectra of Fundamental Organic Molecules, Halsted Press, New York, 1981.

[5] W.-K. Li, S.-W. Chiu, Z.-X. Ma, C.-L. Liao, C. Y. Ng, J. Chem. Phys. 99 (1993) 8440.

[6] K. Raghavachar, B. B. Stefanov, L. A. Curtiss, J. Chem. Phys. 106 (1997) 6764; and references therein.

[7] C. Y. Ng, in T. Baer, C. Y. Ng, I. Powis (Eds.), The Structure, Energetics and Dynamics of Organic Ions, Wiley Series in Ion Chem. and Phys., Wiley, Chichester, 1996, pp. 35-124; C. Y. Ng, in D. C. Neckers, D. H. Volman, G. von Bunau (Eds.), Adv. Photochemistry, Wiley, New York, 1997, Vol. 22, p.1.

[8] D. P. Chong, C. Y. Ng, J. Chem. Phys. 98 (1993) 759.

[9] J. W. Hepburn, in C. Y. Ng (Eds.), Vacuum Ultraviolet Photoionization and Photodissociation of Molecules and Clusters, World Scientific, Singapore, 1991, p. 435.

[10] J. W. Hepburn, in by A. Meyers, T. R. Rizzo (Eds.) Laser Techniques in Chemistry, Wiley, New York, 1994.

[11] A. H. Kung, Y. T. Lee, in C. Y. Ng (Eds.), Vacuum Ultraviolet Photoionization and Photodissociation of Molecules and Clusters, World Scientific, Singapore, 1991, p. 487.

[12] I. Powis, T. Baer, C. Y. Ng (Eds.), High Resolution Laser Photoionization and Photoelectron Studies, Wiley Series in Ion Chemistry and Physics, Wiley, Chichester, 1995; and references therein.

[13] K. Müller-Dethlefs, M. Sander, E. W. Schlag, Z. Naturforsch. A 39a (1984) 1089.

[14] K. Müller-Dethlefs, E. W. Schlag, Ann. Rev. Phys. Chem. 42 (1991) 109.

[15] A. Strobel, I. Fischer, J. Staecker, G. Niednew-Schatteburg, K. Müller-Dethlefs, V. E. Bondybey, J. Chem. Phys. 97 (1992) 2332.

[16] I. Fischer, A. Lochschmidt, A. Strobel, G. Niedner-Schatteburg, K. Müller-Dethefs, V. E. Bondybey, Chem. Phys. Lett. 202 (1993) 542.

[17] C.-W. Hsu, M. Evans, C. Y. Ng, P. Heimann, Rev. Sci. Instrum. 68 (1997) 1694.

[18] C.-W. Hsu, M. Evans, S. Stimson, C. Y. Ng, P. Heimann, J. Chem. Phys. 106 (1997) 8931.

[19] An up-to-date reference list for PFI-PE studies of molecules and radicals can be found in the ZEKE Webpage (http://eos.phys.chemie.tu-muenchen.de/zeke).

[20] Y.-S. Cheung, C.-W. Hsu, C. Y. Ng, W.-K. Li, S.-W. Chiu, Int. J. Mass Spectrom. Ion Processes 159 (1996) 13.

[21] Y.-S. Cheung, J.-C. Huang, C. Y. Ng, J. Chem. Phys. 109 (1998) 1781.

[22] Gaussian 94, Revision B.2, M. J. Frisch, G. W. Trucks, H. B. Schlegel, P. M. W. Gill, B. G. Johnson, M. A. Robb, J. R. Cheeseman, T. Keith, G. A. Petersson, J. A. Montgomery, K. Raghavachari, M. A. Al-Laham, V. G. Zakrzewski, J. V. Ortiz, J. B. Foresman, C. Y. Peng, P. Y. Ayala, W. Chen, M. W. Wong, J. L. Andres, E. S. Replogle, R. Gomperts, R. L. Martin, D. J. Fox, J. S. Binkley, D. J. Defrees, J. Baker, J. P. Stewart, M. Head-Gordon, C. Gonzalez, and J. A. Pople, Gaussian, Inc., Pittsburgh PA, 1995.

[23] C.-W. Hsu, C. Y. Ng, J. Chem. Phys. 101 (1994) 5596.

[24] C.-W. Hsu, D. P. Baldwin, C.-L. Liao, C. Y. Ng, J. Chem. Phys. 100 (1994) 8047.

[25] J.-C. Huang, Y.-S. Cheung, M. Evans, C.-X. Liao, C. Y. Ng, C.-W. Hsu, P. Heimann, H. Lefebvre-Brion, C. Cossart-Magos, J. Chem. Phys. 106 (1997) 864.

[26] S.-W. Chiu, W.-K. Li, W.-B. Tzeng, C. Y. Ng, J. Chem. Phys. 97 (1992) 6557.

[27] K. Watanabe, T. Nakayma, J. Mottl, J. Quant. Spectrosc. Radiat. Trans. 2 (1962) 369.

[28] M. E. Akopyon, Y. L. Sergeev, F. I. Vilesov, Khim. Vys. Energ. 4 (1970) 305 [English translation, High Energy Chem, 4 (1970) 265].

[29] P. F. Bernath, Spectra of Atoms and Molecules, Oxford Univ. Press, Oxford, 1995.

[30] G. Herzberg, Molecular Spectra and Molecular Structure III. Electronic Spectra and Electronic Structure of Polyatomic Molecules, Van Nostrand, New York, 1966.

[31] R. T. Wiedmann, M. G. White, in I. Powis, T. Baer, C. Y. Ng (Eds.), High Resolution Laser Photoionization and Photoelectron Studies, Wiley Series in Ion Chem. and Phys., Wiley, Chichester, 1995, p. 79; and references therein.

[32] L. E. Machdo, L. M. Brescansin, M. A. P. Lima, M. Braunstein, V. McKoy, J. Chem. Phys. 92 (1990) 2362.

[33] M. S. Child, Ch. Jungen, J. Chem. Phys. 93 (1990) 7756.

[34] R. G. Tonkyn, R. T. Wiedmann, E. R. Grant, M. G. White, J. Chem. Phys. 95 (1991) 7033.

[35] R. D. Gilbert, M. S. Child, Chem. Phys. Lett. 187 (1991) 153.

[36] M.-T. Lee, K. Wang, V. McKoy, R. G. Tonkyn, R. T. Wiedmann, E. R. Grant, M. G. White, J. Chem. Phys. 96 (1992) 7848.

[37] M.-T. Lee, K. Wang, V. McKoy, J. Chem. Phys. 97 (1992) 3108.

CHAPTER 7. CONSTRUCTION OF A COMPREHENSIVE VACUUM ULTRAVIOLET LASER SYSTEM

1. Introduction

The study of vacuum ultraviolet (VUV) chemistry has been performed extensively. In the past, it mainly relied on laboratory discharge lamps[1] and synchrotron light sources. Due to advances in laser technology, generation of intense and coherent VUV light is possible.[2-7] The VUV laser system provides much higher light intensity and energy resolution than conventional discharge lamps. The VUV laser system provides higher energy resolution than the synchrotron radiation source. Also important is the cost. The major components of a VUV laser system are commercially available lasers, which are affordable to many research laboratories. The pulsed nature of a coherent VUV laser source is an advantage in time-of-flight (TOF) mass spectrometry and pulsed-field-ionization photoelectron (PFI-PE) spectroscopy studies.[8]

As shown in Chapters 4 to 6 of this thesis, an existing apparatus has been modified to a VUV laser system for photoionization studies. The results are encouraging. To fully utilize the VUV laser technique, it is necessary to make significant modifications to the apparatus. Since the original apparatus was designed for multi-photon ionization (MPI) studies only, many desirable modifications are difficult or even impossible (e.g., due to limit space available).

In spite of the emerging impact of coherent VUV laser sources in experimental chemical research, currently only a few laboratories in the world have a comprehensive tunable VUV laser system[9], even though many already have the ability to construct such

systems. For example, in North America, to our knowledge, only the John W. Hepburn group at the University of Waterloo in Canada and the Michael G. White group at the Brookheaven National Laboratory have actively participated in research using a comprehensive VUV laser system. Recognizing the potential importance of the coherent VUV light source in many related fields, it is worthy to build a dedicated multi-user VUV laser research facility.

The construction of such a facility has been started and I have participated in it. At the moment, the construction is not finished. However, I am glad that the critical parts of the new apparatus have been completed and are functioning very well. The final stage is expected to be finished soon. When operating, the new system is expected to provide many new and interesting research opportunities. In this chapter, the new system is introduced and the progress is reported.

2. Principle of coherent VUV light generation

The coherent frequency mixing technique is used in a VUV laser system to generate coherent VUV light. In the classical picture, the principle of coherent frequency mixing depends on the nonlinear response of a medium to applied electric fields.[10] This is normally expressed as a series expansion in terms of the applied oscillating electric field $\mathbf{E}(\omega)$:

$$\mathbf{P}(\omega) = \chi^{(1)}\cdot\mathbf{E}(\omega) + \chi^{(2)}\cdot\mathbf{E}(\omega)\cdot\mathbf{E}(\omega) + \chi^{(3)}\cdot\mathbf{E}(\omega)\cdot\mathbf{E}(\omega)\cdot\mathbf{E}(\omega) + \ldots, \qquad (1)$$

where $\mathbf{P}(\omega)$ is the induced polarization and $\chi^{(n)}$ is the n^{th} order susceptibility of the medium. The nonlinear terms, $\chi^{(2)}\cdot\mathbf{E}(\omega)\cdot\mathbf{E}(\omega)$, $\chi^{(3)}\cdot\mathbf{E}(\omega)\cdot\mathbf{E}(\omega)\cdot\mathbf{E}(\omega)$, etc., allow induced oscillating

polarization, which is the source of the generated light, to appear at frequencies other than ω, which is the frequency of the applied electric fields (and that of the input light).

For second harmonic generation, $\chi^{(2)}$ must be nonzero, requiring a nonlinear medium without a center of symmetry, such as crystalline materials. Up to date, the shortest wavelength of laser light generated by a nonlinear process with crystalline materials is 189 nm.[11] To generate laser light of wavelength shorter than 189 nm by nonlinear mixing, gaseous atoms must be used as the nonlinear medium.

In general, the more polarizable an atom is, the larger the value of $|\chi^{(3)}|^2$ will be. Commonly used nonlinear gaseous media are rare gases (such as Kr and Xe)[5,12-14] and metal vapors (such as Hg and Mg).[15-17] Since there is a center of symmetry in gaseous atoms, all the even order susceptibilities, including $\chi^{(2)}$, vanish. The $\chi^{(3)}$ term is then the first nonzero nonlinear term in Eq. (1).

In general, if there are three light beams, with frequencies ω_1, ω_2 and ω_3, are merged in a nonlinear medium, the resultant light frequency (ω_s) generated due to the $\chi^{(3)}$ term depends on the interaction of the three oscillating electric fields of frequencies ω_1, ω_2 and ω_3. Hence, we have

$$\omega_s = \omega_i \pm \omega_j \pm \omega_k \qquad (i, j, k = 1, 2, 3) \qquad (2)$$

Since ω_s results from four electric fields oscillating simultaneously in the nonlinear medium, this type of frequency generation is called four-wave mixing.

A special case of four-wave mixing is the third harmonic generation (THG), i.e., the frequency of the generated wave is three times that of the fundamental frequency: $\omega_s = 3\omega_1$.

Obviously, only laser light with single frequency (ω_1) is necessary in THG. The intensity of the generated third harmonic is described by:

$$I_{3\omega} = N^2 \mid \chi^{(3)}(3\omega) \mid^2 I_\omega^3 F(b\Delta k) \qquad (3)$$

where I_ω is the intensity of the fundamental, N is the number density of the nonlinear medium and $\chi^{(3)}(3\omega)$ is the third order susceptibility for the third harmonic generation. The factor $F(b\Delta k)$ results from the macroscopic properties of the medium and the focussing of the fundamental, and it represents the phase matching between the input light and the generated VUV. For THG with focused laser beams at the medium, $F(b\Delta k)$ is non-zero only if the refractive index at 3ω is less than that at ω. Since $F(b\Delta k)$ is pressure dependent (pressure dependence of Δk), one cannot simply increase N to improve $I_{3\omega}$, but the $N^2F(b\Delta k)$ term as a whole must be optimized. Although Eq. (3) is valid only for third harmonic generation, similar equations apply to the other forms of four-wave mixing. The very strong intensity dependence indicated by the $I_{3\omega}$ term essentially restricts four-wave mixing to pulsed lasers, although it is possible to generate cw coherent VUV.

The conversion efficiency of the nonlinear process can be greatly increased through resonant enhancement of $\chi^{(3)}$ when either ω, 2ω or 3ω absorption is resonant with a transition in the nonlinear medium. Since a resonance at ω or 3ω leads to absorption of the input fundamental or the generated third harmonic light, a two-photon resonance is best for enhancing $|\chi^{(3)}|^2$. With only one input frequency, fixing ω to make 2ω correspond to a resonance will not allow for tuning of the generated third harmonic light because 3ω is also fixed. As a result, two independently-tunable fundamental frequencies, ω_1 and ω_2, must be

used to obtain both resonant enhancement and tunability of the generated light. In this case, we have $\omega_s = 2\omega_1 \pm \omega_2$. The two frequencies generated, $2\omega_1 + \omega_2$ and $2\omega_1 - \omega_2$, are called resonant sum frequency (RSFM) and resonant difference frequency (RDFM), respectively. The much higher conversion efficiency in RSFM and RDFM can be rationalized with a quantum mechanical picture. The absorption of the first two ω_1 photon is a resonance process in RSFM and RDFM but a non-resonance process in THG. As a result, the efficiency for the overall three-photon process is much higher in RSFM and RDFM than in THG (by a few orders of magnitude).

The range of VUV frequency generated by THG, RSFM and RDFM depends on 1) the value of ω_1 which depends on the nonlinear medium used, 2) the range of ω_2 which can be produced by an individual dye laser system, and 3) the phase matching condition in the mixing process chosen. The phase matching condition is the same for THG and RSFM but less stringent for RDFM. In practice, the most convenient methods for generating VUV light are: 65.5-100 nm by RSFM in pulsed jets of Kr and Xe; 109-190 nm by RDFM in gas cells of Kr and Xe; 100-109 nm (the gap between the RSFM and RDFM ranges of Kr and Xe) by THG in pulsed jets of Kr and Ar. The range of 105-190 nm can also be generated by RSFM and RDFM in gas cells of Hg and Mg vapors. These practical schemes allow the generation of coherent VUV laser light in the wavelength range of 65.5-190 nm without gap. Depending on the wavelength region, the VUV light intensity in the range 10^9-10^{14} photon/pulse can be achieved.[2,7,17,18]

3. Components of the system

In Fig.1, the schematic setup of the system is shown. Basically, commercial lasers are used to generate coherent light with frequencies ω_1 and ω_2. The two laser beams are combined with a dichromatic mirror and brought into the jet chamber for VUV light generation. The outgoing beam consists of a mixture of light (with frequencies of ω_1, ω_2 and $2\omega_1 \pm \omega_2$, for example) and are separated at the grating in the monochromator chamber. The light of desired frequency (either $2\omega_1 + \omega_2$ or $2\omega_1 - \omega_2$) goes to the main chamber. At the same time, the molecular beam comes from the source chamber in the direction perpendicular to the VUV laser beam direction. Ions and electrons formed from ionization are extracted upward to the mass spectrometer and downward to the electron detector, respectively (see Fig. 2). A light detector is located downstream from the photoionization/photoexcitation (PI/PEX) region to measure the VUV light intensity for spectrum normalization.

In the following part, different components of the system are described in detail. The differences between the new system and the modified apparatus (which was used to perform the VUV experiments in Chapters 4 to 6 in this thesis) will also be discussed.

3.1. Lasers

There are three lasers in the system: one pump laser and two dye lasers. The pump laser is a Nd-YAG laser (GCR-290, Spectra Physics) with output of about 1.6 J/pulse at 1064 nm. A harmonic generation unit is added to generate harmonic light for pumping the dye lasers. The second, third and fourth harmonics (532, 355 and 226 nm, respectively) can be

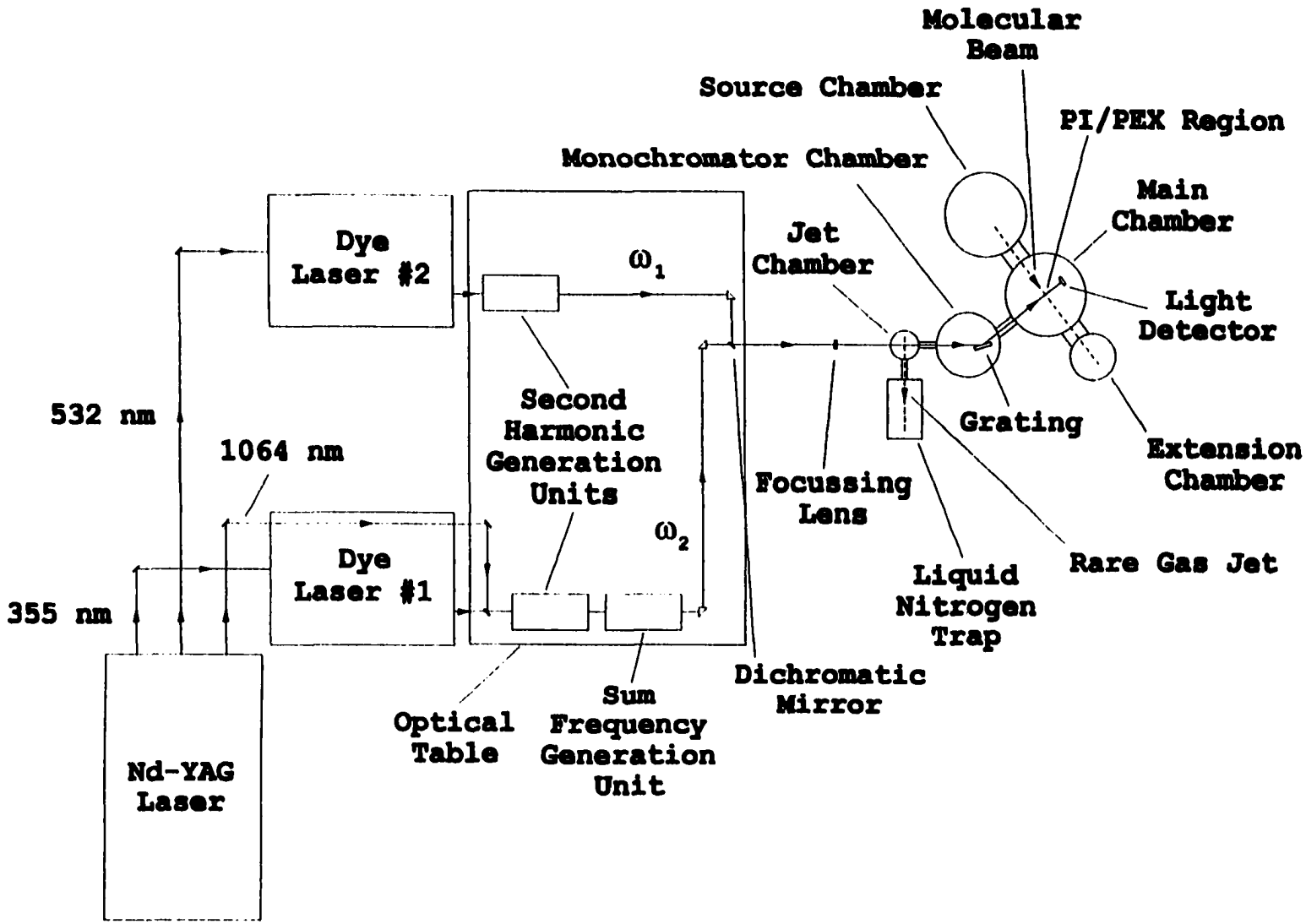

Fig. 1. Schematic setup of the new VUV laser system.

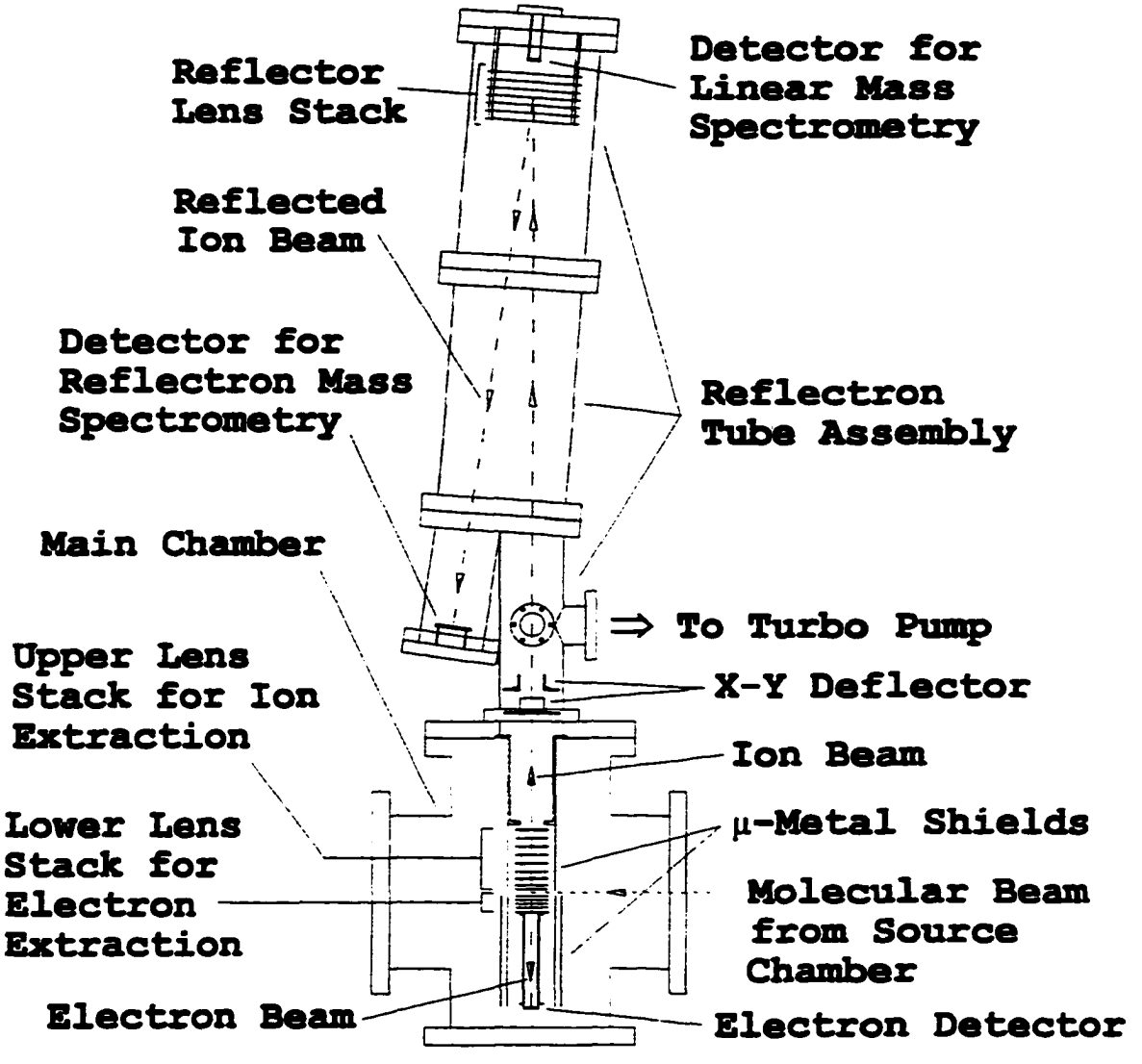

Fig. 2. Cross-section side view for the main chamber and reflectron mass spectrometor of the new VUV laser system. Also shown are the ion, electron and molecular beam paths.

generated (though the third and fourth harmonics cannot be generated at the same time).

The dye lasers can be pumped by either 532 or 355 nm, depending on the range of the outputs desired (which in turn depends on the range of the VUV desired). In terms of pumping light intensity, the worst case would be pumping both dye lasers at 355 nm. The maximum output at 355 nm is about 480 mJ/pulse, i.e., each dye laser is pumped by light energy of 240 mJ/pulse. For the purpose of comparison, the maximum pump beam power of the modified apparatus [by a ten-year old excimer laser (EMG 201 MSG, Lambda Physik) at 308 nm] is usually 250-300 mJ/pulse, i.e., each dye laser is pumped by light energy of ≥150 mJ/pulse. Also, the use of longer wavelength pump beam (355 versus 308 nm) on dye laser pumping results in higher conversion efficiency (by a low percentage). Therefore, the new system is expected to provide higher light intensity from the dye lasers.

Both dye lasers (LDL252, LAS) of the new system are equipped with harmonic generation units to produce continuously tunable laser light from the UV to the IR region. One of the harmonic generation units laser is simply a second harmonic generation unit whereas the other one consists of a second harmonic generation unit and a sum frequency unit. Such an assembly allows a dye laser to generate laser light of wavelength down to 189 nm by mixing the Nd-YAG laser fundamental output and the second harmonic of the dye laser fundamental output.[11]

On the other hand, the dye lasers of the modified apparatus (FL3002, Lambda Physik) are pumped by 308-nm light and the shortest wavelength of photons is only 198 nm (by frequency-tripling of dye laser output at 594 nm).

Also important in high-resolution experiment is the bandwidth of the laser light. The LDL252 dye lasers used in the new system have ultra-narrow bandwidth of about 0.04 cm^{-1}, cf. 0.2 cm^{-1} of the one in the modified apparatus. As a result, the bandwidth of the VUV light generated in the new system is estimated to be $\sqrt{(2\times 2\times 0.04)^2 + 0.04^2} = 0.16\ cm^{-1}$.

3.2. Optics components

A couple of standard commercial optics components are used in the new system. Among them, two are specially designed for utilizing a light beam of two different frequencies, and they require extra description.

The first one is a dichromatic mirror. The content of the surface coating is designed in such a way that the mirror has high reflectivity for one frequency but high transmission for the other one. In our case, the mirror is highly reflective for a narrow range of an UV frequency (ω_1) but has a broad-band transmission for the visible region (covering ω_2). In this way, the two laser beams with different frequencies can be combined, and this kind of mirror is used in both the new system and the modified apparatus.

The second one is an achromatic focussing lens to focus the combined laser beam into the jet chamber. An achromatic focussing lens is an assembly of a convex lens and a concave lens of different curvatures and usually with coated lens surfaces. In the modified apparatus, a simple focussing lens is used. One of the problems of the simple focussing lens is that it has different focal lengths for the different components in the combined beam because the refractive index is different for different frequencies. Hence, the two components are

focussed at different spots. On the other hand, the achromatic focussing lens corrects this problem. When the two components are focused at the same spot, the VUV generation is expected to be more efficient.

3.3. Jet-mixing chamber

A pulsed valve inside the jet-mixing chamber introduces the nonlinear medium (Kr or Xe) as a free jet for VUV generation. The gas density of the non-linear medium near the tip is very high and it is the location at which the combined laser beams are focused. At the opposite port is a liquid-N_2 cooled trap (see Fig. 1) which allows recycling of the expensive Kr and Xe gases. A 210 L/s turbo pump maintains the vacuum. The pressure of the chamber is in the range of 10^{-4} Torr.

Gas cells of nonlinear media has been used in previous experiments performed with the modified apparatus (see Chapters 4-6). The best window material for light transmission is LiF, which has a cut-off of 105 nm. Therefore, the use of gas cells limits the wavelength of the VUV light generated to be >105 nm. On the other hand, the jet-mixing chamber can be connected to the downstream chambers without a window, and the wavelength of the VUV light generated can be extended to <105 nm.

3.4. Monochromator chamber

The VUV light generated in the jet mixing chamber (together with lights of other frequencies) goes into the monochromator chamber (Model 343, McPherson) to have the undesired wavelengths removed before entering the main chamber (see Fig. 1). The vacuum

of the chamber is maintained at about 10^{-7} Torr by a 520 L/s turbo pump. Inside the monochromator chamber is a platinum coated 142° toroidal grating which also re-focuses diffracted light 12.59 inches downstream. The groove density is 275 lines/mm. At first order, the maximum wavelength for diffraction is estimated to be about 500 nm (though the range of optimum efficiency is stated as 50-300 nm by the vendor).

The grating can be scanned either manually or by a remote computer. In remote control mode, the electrical steeping motor for the grating is connected to the grating controller (supplied with the grating), which is connected to a personal computer via RS232 interface. Remote control commands of the grating system are described in detail in the instruction manual provided by the vendor. In principle, the grating scans synchronously with the VUV wavelength. Preliminary testing suggests that it is unnecessary. In practice, the VUV range scanned each experiment is very narrow and the grating, if scanning synchronously with the VUV wavelength, virtually does not move. Therefore, it is only necessary to set the grating position at the beginning (via manual control or interactive computer control) and leave it unchanged during the experiment.

Note that a light-dispersing device such as a monochromator chamber of this kind does not exist in the modified apparatus. The monochromator chamber in the new system serves three purposes: 1) The grating separates the VUV light from the undesired UV and visible lights; 2) The VUV light coming out after jet mixing is always diverging (because focusing at the nonlinear gas jet is necessary), so it is an advantage to have a grating to re-focus the VUV light at the PI/PEX region; 3) The monochromator chamber pumped with a powerful turbo

pump plays an important role in differential pumping and maintains a vacuum gradient between the jet-mixing chamber (10^{-4} Torr) and the main chamber (10^{-7} – 10^{-8} Torr).

Upon diffraction, the VUV light intensity is reduced due to light absorption on the grating surface and light diffraction at the undesired orders (e.g. zeroth order, second order and so on when first order diffraction is used). The specified first order diffraction efficiency is 8% at 250.0 nm, 11.5% at 161.0 nm and 19% at 121.6 nm. For wavelengths shorter than 100 nm, the diffraction efficiency is expected to be higher than 20%. Although a significant portion of VUV light intensity is lost, the re-focusing property of the grating used confines all remaining photons into a small region comparable to the size of the molecular beam. This makes the use of VUV light more efficient than a non-diffracted but diverging beam.

3.5. Source chamber, main chamber and extension chamber

The source chamber, main chamber and extension chamber are connected in series and perpendicular to the diffracted VUV light path from the monochromator chamber (see Fig. 1). Gaseous sample is introduced into the source chamber through a pulsed valve. The molecular beam is skimmed before entering the main chamber. The skimmed beam is intercepted perpendicularly at the center of the main chamber (the PI/PEX region) by the VUV light. The photoionization region is inside an electrostatic lens stack. Ions and electrons are extracted to the reflectron mass spectrometer and electron detector, respectively (also see the section below and Fig. 2). Molecules not ionized fly straight through the main chamber into the extension chamber and are pumped away.

The main chamber contains a window for laser alignment. There is also a window to perform pre-ionization processes on the molecular beam. For example, a separate laser may be used to dissociate the parent molecules into radicals which are photoionized by the VUV laser.

The pumping utilities of the new system are much more powerful than those of the modified apparatus. The source chamber of the new system is pumped by a 10-in. diffusion pump (5300 L/s, VHS-10, Varian) backed up by an ejector pump in series with a roots blower and a mechanical pump. On the other hand, the source chamber of the modified apparatus is pumped by a 6-in. diffusion (pumping speed = 2000 L/s) backed by a mechanical pump. The main chamber and the extension chamber of the new system are pumped together by a 520 L/s turbo pump, whereas the main chamber of the modified apparatus is pumped by a 330 L/s turbo pump. Therefore, a much better vacuum is expected for the new system.

The main chamber of the new system is much bigger than that of the modified apparatus. This allows a more complicated apparatus inside the chamber. For example, a longer lens stack is used in the new system for ion and electron extraction. The extension chamber, which does not exist in the modified apparatus, reserves room for future uses.

3.6. Reflectron mass spectrometer and electron detector

A lens stack is installed at the center of the main chamber at which VUV PI/PEX occurs. Lenses above and below the PI/PEX region extract ions and electrons, respectively. A double-stage micro-channel plate (MCP) for electron detection is located at the bottom of the lens stack.

For mass spectrometric studies, a reflectron tube assembly is installed on top of the main chamber (see Fig. 2). The vacuum is maintained at 10^{-8} Torr with a 230 L/s turbo pump. At the entrance, there is an X-Y deflector (consisting of two pairs of parallel electrostatic lens) for steering the ion beam into the drift tube. A lens stack is installed at the top of the assembly to reflect the ions to the end of the other leg of the assembly (refer to Fig. 2 for the schematic ion path) at which another double-stage MCP detector is located. The orientation of the lens stack can be adjusted via two mechanical feed-throughs on the top flange. In this way, the reflected beam direction can be adjusted for better resolution and/or signal intensity. When the high-resolution of the reflectron technique is not necessary, e.g., when searching the signal at the very beginning of the experiment, linear mass spectrometric detection is necessary due to higher signal intensity and easier operation. For this purpose, a third double-stage MCP detector is located above the reflector lens stack. When doing linear mass spectrometry, the reflector lens stack is turned off and the ions can go straight into the third detector.

The total length of the reflectron drift tube is 2 m, which is about double of that of the linear drift tube used in the modified apparatus. The longer total flight path increases the resolution of the TOF spectra and hence heavier molecules (such as biomolecules) can be studied.

3.7. Light detector

A detector for VUV light detection collects the VUV photons about 3.5" downstream from the PI/PEX region (see Fig. 1). VUV photons hitting the tungsten disc surface of the detector create photoelectrons which are collected by a positively biased copper anode.

The light detector previously used in the modified apparatus has a copper wedge to collect VUV photons. The use of tungsten for the cathode has two advantages over the copper. First of all, tungsten is more inert than copper towards air oxidation and thus has a more stable photoelectric yield. Secondly, the photoelectric yield of tungsten in the range 60 – 90 nm is 14 – 15%, which is slightly higher than that of copper (11 - 13%).[19]

3.8. Data acquisition system

The ion, electron and ion signals are fed into one of the dye laser controllers which also serve to acquire direct current signals. When necessary, the signals are amplified and/or gated before being fed into the controller. Data acquisition is controlled by the WAVESCAN program provided by the dye laser company (LAS) installed on a 486 PC via GPIB connection. The software also synchronizes the scanning of one of the dye lasers (for ω_2 laser light). The time sequence of laser firing, pulse valve opening, etc. are handled by two pulse generators (DG353, Stanford Research) which provide triggering pulses at user-specified time intervals.

4. Current status of the system

The three lasers (one Nd-YAG and two dye lasers) have been tested and the manufacturer specifications are met. All the vacuum chambers are assembled and the jet-mixing, monochromator and main chambers are carefully aligned. Components in various vacuum chambers (such as pulsed values, lens stack and grating) have been installed. Vacuum-maintaining system including turbo pumps, diffusion pump and backup pumps have also been hooked up and are working normally.

We are now attempting to generate VUV light using Xe as a nonlinear medium in the range 102.4-104.1 nm. Oxygen molecules, whose ionization energy (97348 cm^{-1}, corresponding to 102.72 nm) is within this range,[20] will be used as a starting target for the photoionization and photoelectron studies. This species has been studied by Tonkyn et. al.[20] with a VUV laser system and the results can be compared.

5. Further prospective of the system

5.1. Photoionization and photodissociation studies of radical

The new system will be used mainly on radical systems in VUV photoionization mass spectrometric and PFI-PE spectroscopic studies. Up to date, many radicals, some of which are simple, have not been studied thoroughly and their properties are still not well-known.

The sulfur-containing radicals of interest are SO, CS, CH_3S, CH_3CH_2S, CH_2CH_2SH, CH_3SS and C_6H_5S, which can be prepared in abundance by 193- or 248-nm photodissociation (PD) of SO_2, CS_2, CH_3SH (or CH_3SCH_3), $CH_3CH_2SCH_2CH_3$, CH_3CH_2SH, $HSCH_2CH_2SH$, CH_3SSCH_3 and C_6H_5SH (or $C_6H_5SCH_3$), respectively. The conventional PI and PE

spectroscopic studies on are SO, CS, CH_3S, CH_3CH_2S and CH_3SS have been carried out in our group before and much understanding of the formation of these radicals have been gained.[21-25]

We are also interested in some oxygen-containing radicals such as CH_3O, CH_2CH_3O, CH_3CH_2O, CH_3CO and C_6H_5CO. Most of them are important intermediates in combustion processes. These radicals have not been studied extensively. High-resolution laser-induced fluorescence (LIF) studies have been performed on CH_3O[26,27] and CH_3CH_2O[28] by Miller and co-workers. The PI spectrum of CH_3O has also been obtained in a conventional VUV PI mass spectrometric experiment.[29] To our knowledge, however, the remaining radicals (CH_2CH_3O, CH_3CH_2O, CH_3CO and C_6H_5CO) have never been subjected to PI and PE studies. Previous studies show that the methoxy (CH_3O) and ethoxy (CH_3CH_2O) radicals can be prepared by photolysis of the corresponding nirite[26-28] whereas the vinoxy (C_2H_3O) radical can be formed by photolysis of ethyl vinyl ether.[30] Recently, in a 193- and 248-nm PD experiment, we found that the C_6H_5CO and CH_3CO radicals can be generated from $C_6H_5COCH_3$.[31]

Another interesting class of radicals is the halogen-containing radicals such as CCl_2, CBr_2, CClBr, CFBr, $CHBr_2$ and CF_3O. They are relevant to atmospheric degradation of halo-hydrocarbons. An important reason for choosing these radicals is that LIF jet studies on them have been made[32-36] and thus the recipes are known for preparing these radicals. They can prepared by photolysis or pyrolysis of the appropriate halogen-containing precursor molecules in supersonic jets. It is certain that many other halo-hydrocarbons can be prepared by similar methods.

The radicals listed above are by no means exhaustive but simply representative systems of our recent interest. The actual direction of our studies will be guided by our experience and the scientific pay-off.

Understanding the UV and VUV PD processes involved in the formation of these radicals represents an important step for future reactivity studies of these radicals. Furthermore, the detailed characterization of these radicals by high-resolution PI and PE spectroscopy will lead to new experimental schemes for state-selection (rotational, vibrational and electronic) of their cations for ion-molecule reaction studies. We have considerable interest in these topics and plan to pursue these studies in due course.

5.2 Collaborations with other research groups in Iowa State University

The VUV coherent light is an invaluable light source in studies of other fields under vacuum environment. This will certainly induce collaborations with the other research groups, especially those in the Iowa State University. For this purpose, we have designed the new system as a multi-user facility for the other groups to install specific devices necessary for their studies.

At the moment, several plans have been outlined. One of them is to combine VUV laser ionization and matrix-assisted laser desorption (MALA) for mass spectrometric analysis of biomolecules. Because of the soft ionization and prompt fragmentation induced by VUV excitation, the combination of VUV PI and MALA is potentially useful for mass and structural analysis of biomolecules. Another interesting class of experiments is the modification and ablation of surfaces by tunable VUV laser radiation. The high energy VUV

radiation is expected to lead to new surface morphologies as well as chemically active sites. We plan to investigate the changes in both physical and chemical properties of fluorinated polymers induced by irradiation with VUV photons. The change in surface topography and gaseous fragments can be examined by atomic force microscopy and mass spectrometry, respectively. The VUV modified Ag and Au surfaces will also be used as substrates for surface enhanced Raman scattering studies. Finally, we will incorporate VUV PI and excitations to inductively-coupled plasma (ICP) and ICP-MS for elemental analyses to investigate the energy transfer mechanisms concerning vaporization, atomization and ionization in ICP and to modification and ablation of surfaces by tunable VUV laser radiation.

References

1. J. A. R. Samson, *Techniques of Vacuum Ultraviolet Spectroscopy* (Wiley, New York, 1967).

2. J. W. Hepburn, in *Vacuum Ultraviolet Photoionization and Photodissociation of Molecules and Clusters*, edited by C. Y. Ng (World Scientific, Singapore, 1991), p. 435.

3. A. H. Kung and Y. T. Lee, in *Vacuum Ultraviolet Photoionization and Photodissociation of Molecules and Clusters*, edited by C. Y. Ng (World Scientific, Singapore, 1991), p. 487.

4. R. H. Page, R. J. Larkin, A. H. Kung, Y. R. Shen, and Y. T. Lee, Rev. Sci. Instrum. **58**, 1616 (1987).

5. A. H. Kung, Opt. Lett. **8**, 24 (1983).

6. E. Cromwell, T. Trickl, Y. T. Lee, and A. H. Kung, Rev. Sci. Instrum. **60**, 2888 (1989).

7. J. W. Hepburn, in *Generation of Coherent Vacuum Ultraviolet Radiation: Application to High Resolution Photoionization and Photoelectron Spectroscopy, in Laser Techniques in Chemistry*, edited by A. Meyers and T. R, Rizza (Wiley, New York, 1994).

8. *High Resolution Laser Photoionization and Photoelectron Studies*, edited by I. Powis, T. Baer, and C. Y. Ng, Wiley Series in Ion Chem. and Phys. (Wiley, Chichester, 1995); and references therein.

9. These include: U. Heinzman group at University of Bielefeld (Germany), J. W. Hepburn group at University of Waterloo (Canada), Y. T. Lee group at University of California at Berkeley (USA), T. P. Softly group at Oxford University (United Kingdom), C. R. Vidal group at Max-Planck Institute for Extraterrestrial Physics (Germany) and M. G. White group at Brookhaven National Laboratory (USA).

10. Y. R. Shen, *The principle of Nonlinear Optics* (Wiley, New York, 1984).

11. The recipe of generating 189-nm light is the following: frequency-double the laser output of 459.6 nm from a dye laser with a BBOI crystal to 229.8 nm. Then generate the 189-nm light from the 229.8- and 1064-nm (the fundamental of Nd-YAG laser) lights by sum-frequnecy process with a second BBOI crystal.

12. J. Boker, P. H. Bucksbaum, and R. R. Freeman, Opt. Lett. **8**, 217 (1983)

13. G. C. Jorklund, IEEE J. Quant. Elec. **QE-11** 287 (1975).

14. A. Lago, G. Hilber, and R. Wallenstein, Phys. Rev. **A 36**, 3827 (1987).

15. G. Zadsiuk and S. C. Wallace, Appl. Phys. Lett. **28**, 449 (1976).

16. R. Hilbig and R. Wallenstein, IEEE J. Quant. Elec. **QE-19** 1759 (1983).

17. D. J. Hart, Ph. D. thesis, University of Waterloo, 1987.

18. W. Kong, Ph. D. thesis, University of Waterloo, 1993.

19. R. B. Cairns amd J. A. R. Samson, J. Opt. Soc. Am. **56**, 1568 (1966).

20. R. G. Tonkyn, J. W. Winniczek, and M. G. White, Chem. Phys. Lett. **164** 137 (1989).

21. S. Nourbakhsh, K. Norwood, H.-M. Yin, C.-L. Liao, and C. Y. Ng, J. Chem. Phys. **95**, 946 (1991).

22. S. Nourbakhsh, K. Norwood, H.-M. Yin, C.-L. Liao, and C. Y. Ng, J. Chem. Phys. **95**, 5014 (1991).

23. S. Nourbakhsh, H.-M. Yin, C.-L. Liao, and C. Y. Ng, Chem. Phys. Lett. **183**, 348 (1991).

24. S. Nourbakhsh, H.-M. Yin, C.-L. Liao, and C. Y. Ng, Chem. Phys. Lett. **190**, 6283 (1991).

25. C.-W. Hsu, C.-L. Liao, Z.-X. Ma, P. J. H. Tjossem, and C. Y. Ng, J. Phys. Chem. **97**, 6283 (1992).

26. X. Liu, C. P. Damo, T.-D. Lin, S. C. Foster, P. Misra, L. Yu, and T. A. Miller, J. Phys. Chem. **93**, 2266 (1989).

27. X. Liu, S. C. Foster, J. M. Williamson, L. Yu, and T. A. Miller, Mol. Phys. **69**, 357 (1990).

28. X.-Q. Tan, J. M. Williamson, S. C. Foster, and T. A. Miller, J. Phys. Chem. **97**, 9311 (1993).

29. B. Ruscic and J. Berkowitz, J. Chem. Phys. **95**, 4033 (1991).

30. L. F. DiMauro, M. Heaven, and T. A. Miller, J. Chem. Phys. **81**, 2339 (1984).

31. H.-Q. Zhao, Y.-S. Cheung, C.-L. Liao, C.-X. Liao, C. Y. Ng, and W.-K. Li, J. Chem. Phys. **106**, 86 (1997).

32. X.-Q. Tan, T. G. Wright and T. A. Miller, in *Laser Applications in Physical Chemistry*, edited by D. K. Evans (Marcel Dekker, 1994).

33. D. J. Clouthier and H. Karolczak, J. Chem. Phys. **94**, 1 (1991).

34. S. Xu and M. D. Harmony, J. Phys. Chem. **97**, 7465 (1993).

35. R. Schlachta, G. Lask, A. Stangassinger, and V. E. Bondybey, J. Phys. Chem. **95**, 7132 (1991).

36. R. Schlachta, G. Lask, and V. E. Bondybey, Chem. Phys. Lett. **180**, 275 (1991).

CHAPTER 8. GENERAL CONCLUSIONS

Single- and multi-photon ionization techniques have been employed for the photoionization and pulsed field ionization (PFI) studies of the following organsulfur species: CH_3SH, CH_3CH_2SH, CH_3CH_2S and CS_2. Accurate ionization energy (IE) have been determined for these neutral species using high-resolution lasers and PFI scheme. The uncertainty in ionization energy is a few wavenumbers. Information of the energy levels for the neutrals and/or the corresponding cations have been retrieved from the experimental results. In these studies, the resolution of PFI spectra by single vacuum ultraviolet photon ionization is higher than that by multi-photon ionization. The PFI spectra obtained are very similar in the two photoexcitation schemes, while the photoionization efficiency spectra could not be obtained in every case when using the multi-photon scheme. The VUV single-photon ionization/excitation technique is therefore considered cleaner, but MPI method is less demanding in terms of experimental setup. Hence the latter is a simple but more popular tool to be used in related fields.

APPENDIX

COMPUTER PROGRAM LISTING

In this appendix, the contents of two programs are listed. The first (shown in pp. 181-183) was used in the paper in Chapter 2 for calculating energy levels for a rotor potential energy surface. The second (shown in pp. 184-192) was used in the papers in Chapters 5 and 6 for simulation of rotational profile in single-photon pulsed-field ionization spectra.

The programs are written for the Mathcad Plus 6.0 (Professional Version). Note that it is an interactive environment and the programming statements and graphics are put together. Therefore, the content is reproduced here as it appears in the software.

Molecule: CH_3CH_2SH. C-S bond rotation. MP2/6-31G(d,p)

Sine functions, sin(nϕ) where n = 1,2, ..., Nbasis, are used for the odd eigenfunctions. A constant term and cosine functions, cos(nϕ) where n = 1, 2, ..., (Nbasis-1), are used for the even eigenfunctions. Note that the normalization constant for the constant term differs from those for the cosine functions.
A file with 2 columns is read in:

(angle)	(energy in hart.)
0	-476.8 ...
60	-476.8 ...
...	.....

The matrix will be sorted in ascending order of angle.

Define constants and conversion factors

$$h\_bar\_sq\_over\_two\_nu \equiv \frac{5}{4.184 \cdot 1000} \cdot \left(\frac{6.022 \cdot 6.626}{2 \cdot \pi}\right)^2 \qquad red\_I \equiv 1.68 \qquad T \equiv \frac{h\_bar\_sq\_over\_two\_nu}{red\_I}$$

$kcal\_to\_waveno \equiv 349.755$ $\quad Nbasis \equiv 50$ $\quad hart\_to\_kcal \equiv 627.50955$ $\quad T = 0.029$

Read in energy vs angle :

$M := READPRN(NEUTRAL)$ $\quad M := csort(M, 0)$ $\quad globalmin := \min\left(M^{\langle 1 \rangle}\right)$

$M^{\langle 1 \rangle} := \left(M^{\langle 1 \rangle} - globalmin\right) \cdot hart\_to\_kcal$

Extend PES from [0°, 180°] to [-180°, 540°] for fitting.
Assuming periodicity = 360°, symmetric about 180°.

$i := 0..20 \qquad PES_{i,0} := -\left(M_{20-i,0}\right) \qquad PES_{i,1} := M_{20-i,1}$

$i := 21..40 \qquad PES_{i,0} := M_{i-20,0} \qquad PES_{i,1} := M_{i-20,1}$

$i := 41..80 \qquad PES_{i,0} := PES_{i-40,0} + 360 \qquad PES_{i,1} := PES_{i-40,1}$

Convert angle from deg to rad : $PES^{\langle 0 \rangle} := \frac{\pi}{180} \cdot PES^{\langle 0 \rangle}$

Cubic spline fitting

$ANGLE := PES^{\langle 0 \rangle}$ $ENERGY := PES^{\langle 1 \rangle}$ $vs := cspline(ANGLE, ENERGY)$

$V(\phi) := interp(vs, ANGLE, ENERGY, \phi)$ $\theta := 0, 0.25 .. 360$

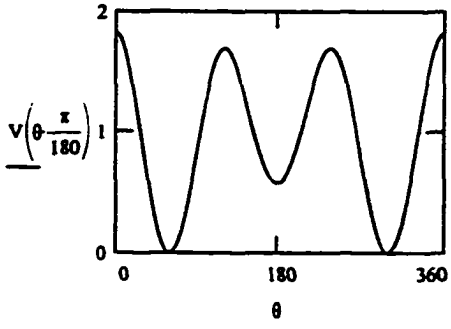

Create T, V and H matrix

$ORIGIN := 1$ $TOL := 0.0001$ $k := 1 .. 2 \cdot Nbasis + 1$

$$Vcos_k := \int_0^{\pi} V(\phi) \cdot \cos((k-1) \cdot \phi)\, d\phi$$

$i := 1 .. Nbasis$ $j := 1 .. Nbasis$

$To_{i,j} := i^2 \cdot T \cdot \delta(i,j)$ $Vo_{i,j} := 0$ $Vo_{i,j} := if\left[i>j, Vo_{j,i}, \frac{1}{\pi} \cdot \left(Vcos_{|i-j|+1} - Vcos_{i+j+1} \right) \right]$

$Te_{i,j} := (i-1)^2 \cdot T \cdot \delta(i,j)$ $Ve_{i,j} := 0$ $Ve_{1,1} := \frac{1}{\pi} \cdot Vcos_1$

$i := 2 .. Nbasis$ $Ve_{1,i} := \frac{\sqrt{2}}{\pi} \cdot Vcos_{i+1}$ $Ve_{i,1} := Ve_{1,i}$

$i := 2 .. Nbasis$ $j := 2 .. Nbasis$ $Ve_{i,j} := if\left[i>j, Ve_{j,i}, \frac{1}{\pi} \cdot \left(Vcos_{|i-j|+1} + Vcos_{i+j-1} \right) \right]$

$Ho := To + Vo$ $\Lambda o := eigenvals(Ho)$ $\lambda o := sort(\Lambda o)$

$He := Te + Ve$ $\Lambda e := eigenvals(He)$ $\lambda e := sort(\Lambda e)$

Now have a look at the eigenvalues: (in kcal/mol) Nbasis = 50

$\lambda o^T =$ [redacted]

0.311 0.899 1.272 1.413 1.8 2.049 2.41 2.831 3.308 3.847 4.444 5.1 5.814 6.586 7.416

$\lambda e^T =$ [redacted]

0.367 0.689 1.089 1.207 1.603 1.922 2.045 2.428 2.832 3.308 3.847 4.444 5.1 5.814

Eigenvalues in cm^{-1}:

$kcal\_to\_waveno \cdot \lambda o^T =$ [redacted]

108.78 314.45 444.89 494.3 629.52 716.59 842.92 990.06 $1.16 \cdot 10^3$

$kcal\_to\_waveno \cdot \lambda e^T =$ [redacted]

128.28 241.12 380.9 422.31 560.81 672.23 715.36 849.07 990.59

Produce coeff-matrix such that $\underline{\psi} = \underline{C} * \underline{\chi}$ where both $\underline{\psi}$ and $\underline{\chi}$ are column vectors.

$k := 1 .. Nbasis$ $\quad coeffo^{\langle k \rangle} := eigenvec(Ho, \lambda o_k)$ $\quad Co := coeffo^T$

$coeffe^{\langle k \rangle} = eigenvec(He, \lambda e_k)$ $\quad Ce := coeffe^T$

Wavefunctions so obtained: (ψ in deg)

$$\psi_o(m,\phi) := \frac{1}{\sqrt{\pi}} \cdot \sum_{n=1}^{Nbasis} Co_{m,n} \cdot \sin\left(n \cdot \phi \cdot \frac{\pi}{180}\right)$$

$$\psi_e(m,\phi) := \frac{1}{\sqrt{\pi}} \left[\frac{1}{\sqrt{2}} \cdot Ce_{m,1} + \sum_{n=2}^{Nbasis} Ce_{m,n} \cdot \cos\left[(n-1) \cdot \phi \cdot \frac{\pi}{180}\right] \right]$$

Write coefficients onto files:

WRITEPRN(SINCOEFF) := Re(Co) $\quad$ WRITEPRN(COSCOEFF) := Re(Ce)

Stimulation for CH_3SH.

Expt := READPRN(ExptData1)

TOL := 0.000001 EngConv ≡ 0.69503877

A ≡ 3.50 B ≡ 0.43 C ≡ 0.41

$A_{cat} \equiv 3.46$ $B_{cat} \equiv 0.46$ $C_{cat} \equiv 0.44$

$J_{trun} \equiv 20$ $Pop_{thre} \equiv 0.001$ T ≡ 20 kT ≡ EngConv·T kT = 13.901

Define Hamiltonian matrice elements:

$$Hij(A,B,C,J,Ki,Kj) := \begin{cases} \left[\left(\frac{A+B}{2}\right)\cdot J\cdot(J+1)+\left(C-\frac{A+B}{2}\right)\cdot Ki^2\right] & \text{if } Ki \equiv Kj \\ \frac{A-B}{4}\cdot\sqrt{(J-Kj)\cdot(J+Kj+1)\cdot(J-Kj-1)\cdot(J+Kj+2)} & \text{if } Ki \equiv Kj+2 \\ \frac{A-B}{4}\cdot\sqrt{(J+Kj)\cdot(J-Kj+1)\cdot(J+Kj-1)\cdot(J-Kj+2)} & \text{if } Ki \equiv Kj-2 \\ 0 \quad \text{otherwise} \end{cases}$$

Define a procedure to work out the energy levels for the asymmetric tops using A, B, C:

```
EngLev(A,B,C) := temp_0 ← 0
                 for J ∈ 1..J_trun
                   for i ∈ 0..2·J
                     for j ∈ 0..2·J
                       H_i,j ← Hij(A,B,C,J,i-J,j-J)
                   temp ← stack(temp, sort(Re(eigenvals(H))))
                 temp
```

```
NeuJ := temp_0 ← 0
        for J ∈ 1..J_trun
          for i ∈ 0..2·J
            dummy_0 ← J
            temp ← stack(temp, dummy)
        temp
```

NeuEng := EngLev(A,B,C)

$$NeuPop := \left[(2\cdot NeuJ+1)\cdot e^{-\frac{NeuEng}{kT}}\right]$$

Population of neutral r.w.t. J.

$$PopJ := \left| \begin{array}{l} \text{for } i \in 0..J_{trun} \\ \quad \left| \begin{array}{l} temp_i \leftarrow 0 \\ \text{for } j \in i^2..(i+1)^2 - 1 \\ \quad temp_i \leftarrow temp_i + NeuPop_j \end{array} \right. \\ temp \end{array} \right.$$

$$J_{max} := \left| \begin{array}{l} temp \leftarrow (0 \;\; 0) \\ \text{for } i \in 0..last(PopJ) \\ \quad temp \leftarrow \left| \begin{array}{l} (i \;\; PopJ_i) \text{ if } PopJ_i > temp_{0,1} \\ temp \text{ otherwise} \end{array} \right. \\ temp_{0,0} \end{array} \right.$$

$i := 0..last(PopJ)$

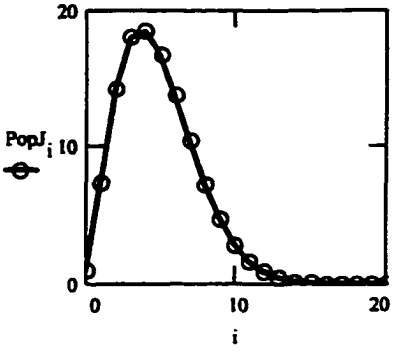

$J_{max} = 4$

Poplulation in energy.

$$SortNeuEng := csort(augment(NeuEng, NeuPop), 0)$$

$$(E_{max} \;\; Pop_{max}) := \left| \begin{array}{l} temp \leftarrow (0 \;\; 0) \\ \text{for } i \in 0..last(NeuPop) \\ \quad temp \leftarrow \left| \begin{array}{l} (SortNeuEng_{i,0} \;\; SortNeuEng_{i,1}) \text{ if } SortNeuEng_{i,1} > temp_{0,1} \\ temp \text{ otherwise} \end{array} \right. \\ temp \end{array} \right.$$

$E_{max} = 8.399$

$$NeuEngCum := \left| \begin{array}{l} temp_0 \leftarrow SortNeuEng_{0,1} \\ \text{for } i \in 1..rows(SortNeuEng) - 1 \\ \quad temp_i \leftarrow temp_{i-1} + SortNeuEng_{i,1} \\ temp \end{array} \right.$$

$NeuEngLst := last(NeuEng)$

$$E_{trun} := \left| \begin{array}{l} i \leftarrow 0 \\ \text{while } \dfrac{NeuEngCum_i}{NeuEngCum_{NeuEngLst}} < (1 - Pop_{thre}) \\ \quad i \leftarrow i + 1 \\ SortNeuEng_{i,0} \end{array} \right.$$

$$E_{trun} = 113.948$$

$$Ka := \left| \begin{array}{l} temp_0 \leftarrow 0 \\ \text{for } J \in 1..J_{trun} \\ \quad \left| \begin{array}{l} dummy_0 \leftarrow 0 \\ temp \leftarrow stack(temp, dummy) \\ \text{for } i \in 1..J \\ \quad \left| \begin{array}{l} dummy_0 \leftarrow i \\ temp \leftarrow stack(temp, dummy) \\ temp \leftarrow stack(temp, dummy) \end{array} \right. \end{array} \right. \\ temp \end{array} \right.$$

$$Kc := \left| \begin{array}{l} temp_0 \leftarrow 0 \\ \text{for } J \in 1..J_{trun} \\ \quad \left| \begin{array}{l} \text{for } i \in J, J-1..1 \\ \quad \left| \begin{array}{l} dummy_0 \leftarrow i \\ temp \leftarrow stack(temp, dummy) \\ temp \leftarrow stack(temp, dummy) \end{array} \right. \\ dummy_0 \leftarrow 0 \\ temp \leftarrow stack(temp, dummy) \end{array} \right. \\ temp \end{array} \right.$$

Create a matrix containing energy, J, K_a, K_c and population for each level, in ascending order of energy and energy smaller than or equal to E_{trun}.

$$Neutral := \left| \begin{array}{l} i \leftarrow 0 \\ \text{for } j \in 0..last(NeuEng) \\ \quad \text{if } NeuEng_j \le E_{trun} \\ \quad \quad \left| \begin{array}{l} temp_{i,0} \leftarrow NeuEng_j \\ temp_{i,1} \leftarrow NeuJ_j \\ temp_{i,2} \leftarrow Ka_j \\ temp_{i,3} \leftarrow Kc_j \\ temp_{i,4} \leftarrow NeuPop_j \\ i \leftarrow i + 1 \end{array} \right. \\ temp \end{array} \right.$$

Create a similar matrice for the cation (without truncation in energy):

$$\text{CatEng} := \text{EngLev}(A_{cat}, B_{cat}, C_{cat})$$

$$\text{Cation} := \text{csort}(\text{augment}(\text{augment}(\text{augment}(\text{CatEng}, \text{NeuJ}), \text{Ka}), \text{Kc}), 1)$$

Define a procedure to calculate the line spectrum with ΔJ as a parameter:

```
Branch(ΔJ) := | k ← 0
              | CatLst ← rows(Cation) - 1
              | for i ∈ 0..rows(Neutral) - 1
              |     J ← Neutral_{i,1}
              |     J_cat ← J + ΔJ
              |     if (Cation_{CatLst,1} ≥ J_cat)·(J_cat ≥ Cation_{0,1})
              |         j ← 0
              |         while (j ≤ CatLst)·(Cation_{j,1} ≤ J_cat)
              |             if Cation_{j,1} = J_cat
              |                 temp_{k,0} ← Cation_{j,0} - Neutral_{i,0}
              |                 temp_{k,1} ← Neutral_{i,4}
              |                 temp_{k,2} ← Cation_{j,2} - Neutral_{i,2}
              |                 temp_{k,3} ← Cation_{j,3} - Neutral_{i,3}
              |                 temp_{k,4} ← Neutral_{i,1}
              |                 temp_{k,5} ← Cation_{j,1} - Neutral_{i,1}
              |                 k ← k + 1
              |             j ← j + 1
              | temp
```

Define a procedure to extract a sub-branch from a branch obtained with the "Branch(ΔJ)" procedure with specific ΔK. To get the lines for ΔK_a = 100, set ΔKCol = 2 and ΔK = 100. For ΔK_c = 54, set ΔKCol = 3 and ΔK = 54. By running this procedures two times, transition lines with both ΔK_a = 2 and ΔK_c = 3 can be obtained.

```
SubBranch(Branch, ΔKCol, ΔK) := | i ← 0
                                | for j ∈ 0..rows(Branch) − 1
                                |   if Branch_{j,ΔKCol} = ΔK
                                |     | for k ∈ 0..5
                                |     |   temp_{i,k} ← Branch_{j,k}
                                |     | i ← i + 1
                                | temp
```

Create O-, P-, Q-, R- and S-branch (ΔJ = -2, -1, 0, +1 and +2, respectively):

O := Branch(-2) P := Branch(-1) Q := Branch(0)

R := Branch(1) S := Branch(2)

Pick up ΔK_a = -2, -1, 0, +1 and +2 in O-branch:

Oo := SubBranch(O,2,-2) Op := SubBranch(O,2,-1) Oq := SubBranch(O,2,0)

Or := SubBranch(O,2,1) Os := SubBranch(O,2,2)

Pick up ΔK_a = -2, -1, 0, +1 and +2 in P-branch:

Pq := SubBranch(P,2,0)

Po := SubBranch(P,2,-2) Pp := SubBranch(P,2,-1)

Pr := SubBranch(P,2,1) Ps := SubBranch(P,2,2)

Pick up ΔK_a = -2, -1, 0, +1 and +2 in Q-branch:

Qo := SubBranch(Q,2,-2) Qp := SubBranch(Q,2,-1) Qq := SubBranch(Q,2,0)

Qr := SubBranch(Q,2,1) Qs := SubBranch(Q,2,2)

Pick up ΔK_a = -2, -1, 0, +1 and +2 in R-branch:

Ro := SubBranch(R,2,-2) Rp := SubBranch(R,2,-1) Rq := SubBranch(R,2,0)

Rr := SubBranch(R,2,1) Rs := SubBranch(R,2,2)

Pick up ΔK_a = -2, -1, 0, +1 and +2 in S-branch:

So := SubBranch(S,2,-2) Sp := SubBranch(S,2,-1) Sq := SubBranch(S,2,0)

Sr := SubBranch(S,2,1) Ss := SubBranch(S,2,2)

Define another batch of constants which are necessary for spectrum plotting and line spectrum convolution:

LinWid ≡ 2 $IP_1 \equiv 76252.5$

ExptLst := rows(Expt) - 1 ExptLst = 600 $Expt_{0,0} = 76209.95$ $Expt_{ExptLst,0} = 76305.90$

$SpectSrt := Expt_{0,0} - IP_1$ $SpectEnd := Expt_{ExptLst,0} - IP_1$ $SpectStep := \frac{SpectEnd - SpectSrt}{ExptLst}$

SpectSrt := SpectSrt SpectEnd := SpectEnd SpectStep := SpectStep

The followings are NOT parameters. Don't touch them.

$SpectLst := ceil\left(\frac{SpectEnd - SpectSrt}{SpectStep}\right)$ SpectStep = 0.16 SpectLst = 600

Create a grid table for lines to be convoluted.

$$
\begin{aligned}
&\text{GridTab} := \left|\begin{array}{l}
\text{temp}_0 \leftarrow 0.1 \cdot \text{SpectStep} \\
\text{thres} \leftarrow 0.001 \\
\alpha \leftarrow \dfrac{4 \cdot \ln(2)}{\text{LinWid}^2} \\
x \leftarrow 0 \\
i \leftarrow 1 \\
\text{temp}_1 \leftarrow 1 \\
\text{while } \text{temp}_i \geq \text{thres} \\
\quad \left|\begin{array}{l}
x \leftarrow x + \text{temp}_0 \\
i \leftarrow i + 1 \\
\text{temp}_i \leftarrow e^{-\alpha \cdot x^2}
\end{array}\right. \\
\text{temp}
\end{array}\right.
\end{aligned}
$$

Create a look-up table for the Gaussian function.

$$
\begin{aligned}
&\text{LkupGsn}(x) := \left|\begin{array}{l}
\text{idx} \leftarrow \text{floor}\left(\dfrac{|x|}{\text{GridTab}_0} + 0.5\right) \\
\text{temp} \leftarrow \left|\begin{array}{ll}
\text{GridTab}_{\text{idx}+1} & \text{if idx} < \text{last}(\text{GridTab}) \\
0 & \text{otherwise}
\end{array}\right. \\
\text{temp}
\end{array}\right.
\end{aligned}
$$

Convolution procedure: put the branch or sub-branch as parameter:

$$
\begin{aligned}
&\text{Convol}(M) := \left|\begin{array}{l}
\text{for } i \in 0..\text{SpectLst} \\
\quad \text{temp}_i \leftarrow 0 \\
\text{for } i \in 0..\text{rows}(M)-1 \\
\quad \left|\begin{array}{l}
\text{GsnHfWid} \leftarrow \text{length}(\text{GridTab})\cdot \text{GridTab}_0 \\
\text{LftTail} \leftarrow M_{i,0} - \text{GsnHfWid} \\
\text{Low} \leftarrow \text{floor}\left(\dfrac{\text{LftTail}-\text{SpectSrt}}{\text{SpectStep}}\right) \\
\text{Low} \leftarrow \left|\begin{array}{ll} \text{Low} & \text{if Low}>0 \\ 0 & \text{otherwise} \end{array}\right. \\
\text{templ}_{i,0} \leftarrow \text{Low} \\
\text{RgtTail} \leftarrow M_{i,0} + \text{GsnHfWid} \\
\text{High} \leftarrow \text{ceil}\left(\dfrac{\text{RgtTail}-\text{SpectSrt}}{\text{SpectStep}}\right) \\
\text{High} \leftarrow \left|\begin{array}{ll} \text{High} & \text{if High}<\text{SpectLst} \\ \text{SpectLst} & \text{otherwise} \end{array}\right. \\
\text{templ}_{i,1} \leftarrow \text{High} \\
\text{templ}_{i,2} \leftarrow (\text{High}-\text{Low})\cdot\text{SpectStep} \\
\text{if } (\text{Low}\le\text{SpectLst})\cdot(\text{High}\ge 0) \\
\quad \left|\begin{array}{l}
\text{Eng} \leftarrow \text{SpectSrt} + \text{Low}\cdot\text{SpectStep} \\
\text{for } j \in \text{Low}..\text{High} \\
\quad \left|\begin{array}{l}
\text{temp}_j \leftarrow \text{temp}_j + M_{i,1}\cdot\text{LkupGsn}\left(\text{Eng}-M_{i,0}\right) \\
\text{Eng} \leftarrow \text{Eng} + \text{SpectStep}
\end{array}\right.
\end{array}\right.
\end{array}\right. \\
&\text{temp}
\end{aligned}
$$

Convolute branches:

QoSpect := Convol(Qo)	QpSpect := Convol(Qp)	QqSpect := Convol(Qq)
QrSpect := Convol(Qr)	QsSpect := Convol(Qs)	
PpSpect := Convol(Pp)	PqSpect := Convol(Pq)	PrSpect := Convol(Pr)
PoSpect := Convol(Po)	PsSpect := Convol(Ps)	
RpSpect := Convol(Rp)	RqSpect := Convol(Rq)	RrSpect := Convol(Rr)
RoSpect := Convol(Ro)	RsSpect := Convol(Rs)	

OoSpect := Convol(Oo) OpSpect := Convol(Op) OqSpect := Convol(Oq)

OrSpect := Convol(Or) OsSpect := Convol(Os)

SoSpect := Convol(So) SpSpect := Convol(Sp) SqSpect := Convol(Sq)

SrSpect := Convol(Sr) SsSpect := Convol(Ss)

Create final spectra:

ExptSpect := $Expt^{\langle 1 \rangle}$ + 2770 $IP_1 = 76252.50$ $IP_2 = 0$ $IP = IP_1 - IP_2$

$IP = 76252.50$

o:p:q:r:s = K2:K1:K0:K1:K2; O:P:Q:R:S = J2:J1:J0:J1:J2.

K0 := 1 K1 := 1.2 K2 := 0.7 J0 := 1 J1 := 1.1 J2 := 0.6

P01 := J1·(K1·PpSpect + K0·PqSpect + K1·PrSpect) P2 := J1·(K2·PoSpect + K2·PsSpect)

Q01 := J0·(K1·QpSpect + K0·QqSpect + K1·QrSpect) Q2 := J0·(K2·QoSpect + K2·QsSpect)

R01 := J1·(K1·RpSpect + K0·RqSpect + K1·RrSpect) R2 := J1·(K2·RoSpect + K2·RsSpect)

O012 := J2·(K2·OoSpect + K1·OpSpect + K0·OqSpect + K1·OrSpect + K2·OsSpect)

S012 := J2·(K2·SoSpect + K1·SpSpect + K0·SqSpect + K1·SrSpect + K2·SsSpect)

Stimul := P01 + Q01 + R01 + P2 + Q2 + R2 + O012 + S012

max1 := max(ExptSpect) max2 := max(Stimul) $Stimul := Stimul \cdot \frac{max1}{max2}$

i := 0.. rows(Stimul) − 1 j := 0.. rows(Expt) − 1

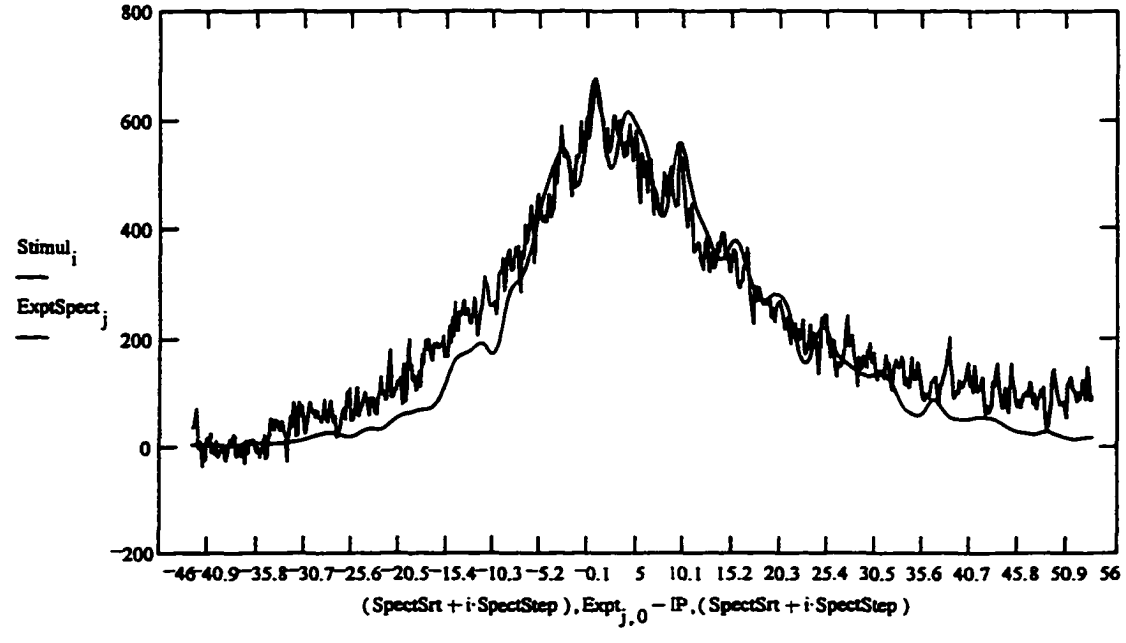

IMAGE EVALUATION
TEST TARGET (QA-3)

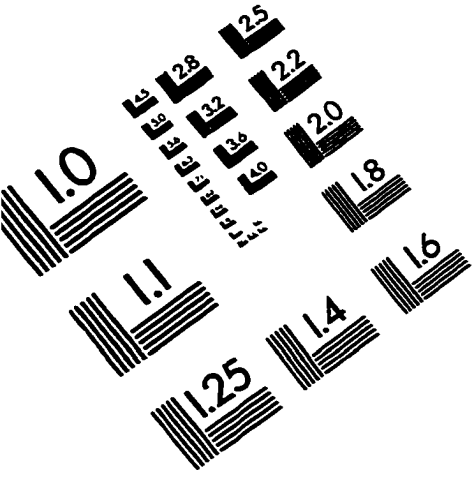

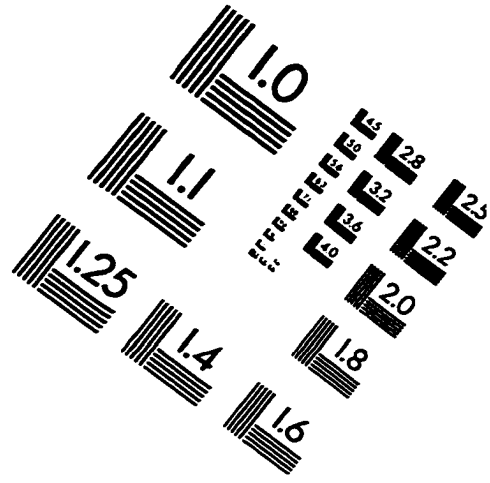

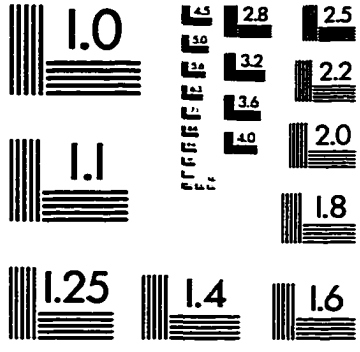

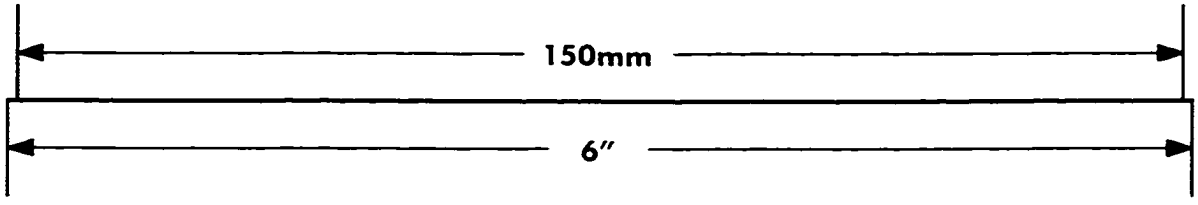

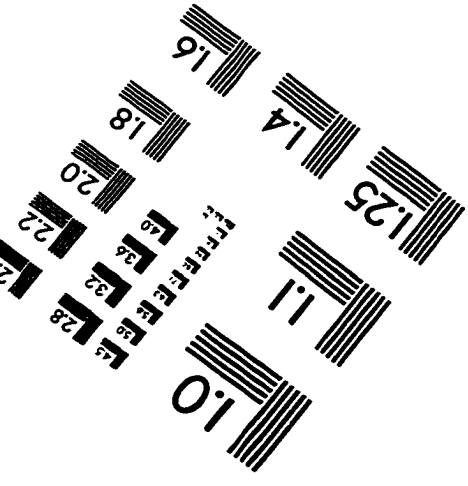

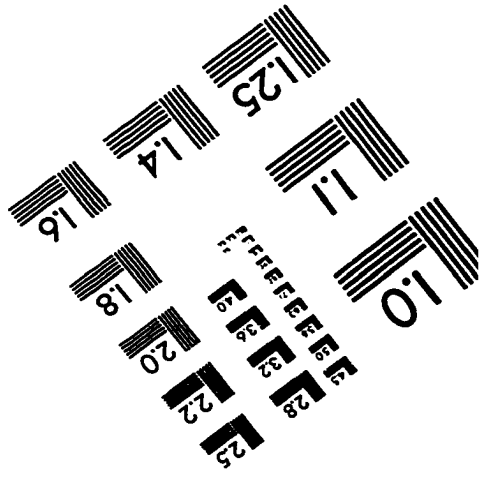

APPLIED IMAGE, Inc
1653 East Main Street
Rochester, NY 14609 USA
Phone: 716/482-0300
Fax: 716/288-5989